Observations of Near-Surface Temperature and Salinity from Profiling Floats: Vertical Variability, Structure, and Connection to Deeper Properties

Jessica E. Anderson

A dissertation

submitted in partial fulfillment of the

requirements for the degree of

Doctor of Philosophy

University of Washington

2018

Reading Committee:

Stephen C. Riser, Chair

Meghan F. Cronin

Mark J. Warner

Program Authorized to Offer Degree:

School of Oceanography

University of Washington

Abstract

Observations of Near-Surface Temperature and Salinity from Profiling Floats:
Vertical Variability, Structure, and Connection to Deeper Properties

Jessica E. Anderson

Chair of the Supervisory Committee:
Professor Stephen C. Riser
School of Oceanography

In response to the changing climate, it is probable that there is an intensification of the oceanic hydrologic cycle underway. Due to the difficulty of observing the ocean, especially very close to the sea surface, we lack the detailed observations of ocean salinity (a proxy for the oceanic freshwater cycle) necessary to fully understand and model the complex dynamics governing the ocean's role in the hydrologic cycle and how it might change in the future. While relatively new measurements of sea surface salinity from satellites (Aquarius/SAC-D, SMOS, and SMAP) have enhanced our understanding of the freshwater cycle over the ocean, sea surface satellite maps integrate over relatively large scales and blur the short-lived, small-scale variability (where precipitation occurs) that remains poorly constrained. This dissertation explores the magnitude,

frequency, and structure of such near-surface temperature and salinity variability and how it is connected to larger-scale, subsurface ocean properties.

The first two chapters of this dissertation utilize observations obtained from profiling floats equipped with auxiliary Surface Temperature and Salinity (STS) sensors. These novel instruments allow for high vertical resolution (10 cm) examination of near-surface (~0.2-30 m) temperature and salinity stratification usually not possible in the context of Argo. Observations from STS equipped Argo-type floats deployed in the tropical and subtropical Pacific, Atlantic, and Indian Oceans show that the upper 4 m of the ocean are well-mixed most of the time (87% for temperature, 97% for salinity), generally associated with wind speeds > 6 m/s. This homogeneity is interrupted by significant and often short-lived warming/cooling and freshening events. A subset of floats programmed to profile rapidly (~2.5 hours) shows a strong diurnal signal in temperature with salinity exhibiting somewhat weaker diurnal variations. The diurnal cycle magnitude is largest in areas with light winds and heavy precipitation and was found to decay rapidly with depth (50% over the top 2 m). Observations of near-surface salinity drop events associated with rainfall show an average freshening of -0.37 PSU associated with a cooling of 0.13 °C. The fresh lenses are typically 3 m thick with maximum freshening in the upper ~0.6 m. Conditions favorable for double diffusion are present at the base of the fresh lens. Fresh lenses are typically short-lived with downward mixing occurring within 6-8 hrs (equivalent diffusivity ~10^{-4} m^2/s). A linear correlation between rain rate and salinity drop magnitude was not found across a range of wind speeds due to covariance between wind speed and rain rate. This work provides insight into near-surface vertical processes with the goal of refining the representation of upper ocean dynamics in models and putting observed discrepancies between satellite and in situ measurements in context.

The final chapter of this dissertation examines mixed layer properties and subduction rates of high salinity water in an evaporation dominated region of the North Atlantic Ocean (~ 25°N, 38°W) which was heavily surveyed during the NASA-sponsored Salinity Processes in the Upper Ocean Regional Study (SPURS). High spatial resolution, objective maps of temperature, salinity, and mixed layer depth (MLD) (created from Argo, Seaglider, and mooring data) show low spatial variability during the late spring and summer months and higher spatial variability during the late winter and early spring as the mixed layer shoals. This spatial variability is not represented in previous climatologies; meaning prior estimates of annual subduction may be low. These results are put into context with updated, Argo era climatological values of annual subduction for the North Atlantic. Higher temporal and spatial resolution MLD maps combined with mooring velocities and satellite wind stresses were used to investigate both the annual mean and eddy-varying subduction rates in the SPURS region. MLD spatial variability leads to an enhanced lateral induction contribution to annual subduction rates. Eddy subduction rates are locally large when a time-varying MLD is used. Averaged over the SPURS domain however, the net eddy contribution is likely small. This work highlights the importance of capturing MLD variations when examining subduction and water mass formation rates.

TABLE OF CONTENTS

LIST OF FIGURES

LIST OF TABLES

ACKNOWLEDGEMENTS

I would like to thank my advisor Stephen Riser for his mentorship during my time in graduate school. I appreciate the perspective our numerous discussions about science and life provided and I am especially grateful for his patience with my exploration of numerous paths.

I would also like to thank the members of my committee, Meghan Cronin, Mark Warner, and Dargan Frierson for constructive criticism, which helped me more fully develop my science.

Numerous other people contributed positively to my time at UW with enlightening conversations, troubleshooting, and, most importantly, laughter. Particularly, I would like to thank Kathie Kelly, LuAnne Thompson, Andrey Shcherbina, Carol Janzen, Dave Murphy, Kim Martini, the science party and crew of S4P, the numerous Aquarius, SMOS, and SPURS scientists who provided a scientific community for feedback, the UW Oceanography administrative staff, the international Argo program, Rick Rupan, Annie Wong, Dana Swift, Dale Ripley, Greg Brusseau, Robert Drucker, Mike Johnson, Jim Bennett, and "lab" mates Alison, Tyler, Earle, Rosalind, and Ian, and the supportive and fun UW Oceanography graduate school community – my numerous years here were better because of you.

A huge thank you to the friends that kept me sane, convinced me to stay, and shared many an outdoor activity, dance, or nacho/sushi session, Kirsten, Liz, Andrea, Alyssa, Nancy, Sarah, Alison, Andy, Seth, and Noel. Thank you for making graduate school fun!

Finally, thank you to my family and family of friends for your support during some of the hardest times and for also sharing in the biggest laughs, especially my sister Sarah, mother Patty, like a mother Ellie, forever friends Margaret and Kacey, and Ben.

DEDICATION

To my Montessori preschool teacher who encouraged me to find fun in numbers,

my 9th grade geometry teacher and track coach Mr. Anderson for helping me find the confidence

to continue doing so,

and the little things in nature for the continued inspiration.

"A surprising result emerges!"

– James R. Miller

Chapter 1

Introduction

As a result of anthropogenic greenhouse gas emissions, the Earth system is projected to continue experiencing unequivocal warming in the coming decades. In response to this warming, an intensification of the hydrologic cycle is expected which may increase the likelihood of floods and droughts as well as impact water quality and food security (Bates et al., 2008). Under the wet-get-wetter, dry-get-drier paradigm of global warming water cycle intensification, precipitation is expected to scale (3.4 % increase per 1° K) with water vapor increases (6.5 % increase per 1° K) expected by the Clausius–Clapeyron relationship (Allen & Ingram, 2002; Held & Soden, 2006). There is disagreement among modeling studies in producing results consistent with this paradigm however, and recent work indicates this may be the result of shifting atmospheric cells and precipitation bands (Polson & Hegerl, 2017; Scheff & Frierson, 2012).

Direct observations of water cycle intensification over land are limited due to record length and observational coverage. Since the majority of freshwater cycling occurs between the atmosphere and ocean (78% of precipitation falls over ocean) it makes sense to look for changes to this system within the ocean environment (Durack, 2015; Schanze et al., 2010). Using salinity as a proxy for freshwater, hydrologic cycle changes can be inferred from salinity trends in ocean observations (Durack et al., 2012; Skliris et al., 2016). Atmospheric circulation patterns which lead to rainforests and deserts over land leave a similar footprint on the salinity field of the ocean surface. In latitudes with large precipitation, such as the low and high latitudes, sea surface

salinity is fresher. In the subtropics, surface salinity is higher due to enhanced evaporation. However, even at large scales, the ocean does not act as a perfect rain gauge. There is an offset in the location of maximum evaporation from the sea surface and the location of maximum salinity, which illustrates the importance of ocean dynamics in mixing the atmospheric forcing away from the source. Recent improvements in our ability to observe ocean salinity in situ and through remote sensing, via the global Argo array and the Aquarius, SMOS, and SMAP satellites, have facilitated efforts to observe the hydrologic cycle in the ocean (Kerr et al., 2010; Lagerloef et al., 2008; Riser et al., 2016).

While observations from Argo and satellites provide a wealth of new insights, they integrate over large time and space scales where most air-sea interactions occur. In interpreting these datasets, it is of interest to know how and where they may be biased. Of particular interest are processes that lead to upper ocean stratification in temperature and salinity (Boutin et al., 2015; Donlon et al., 2002). Strong upper ocean stratification can lead to systematic biases between in situ observations (taken at 4 m) and satellite measurements (sensed to ~1 cm) (Boutin et al., 2013, 2015; Drucker & Riser, 2014). Strong, stable stratification can also lead to enhanced diurnal cycles which can increase surface heat fluxes by up to 60 W m^2 as well as influence the onset of Madden Julian Oscillation (MJO) events and monsoons (Bernie et al., 2005; Clayson & Bogdanoff, 2013; Klingaman et al., 2011; Woolnough et al., 2007). Understanding the processes that lead to the two extremes of ocean salinity, fresh and salty, is also pertinent to understanding the oceanic freshwater cycle. The freshest end members, rain lenses, are short lived and geographically limited. Their evolution and feedback to air-sea fluxes is still not well constrained (Asher et al., 2014; Drushka et al., 2016). Salty lenses are rarely observed due to their unstable

stratification (Yu, 2010). The integrated response to large-scale evaporation is what gives subtropical mode waters their properties however.

The focus of this dissertation is on understanding the small-scale variability of the upper ocean and mixed layer as it relates to the ocean's role in the freshwater cycle. Small-scale variability is examined with in situ observations in both fresh and salty regions. In Chapter 2, the frequency of significant upper ocean stratification is examined using novel observations of the near-surface obtained with Argo-type floats equipped with a secondary, Surface Temperature and Salinity CTD which collects high vertical resolution measurements of temperature and salinity in the upper 30 m. While the upper ocean is well mixed most of the time, large stratification events are observed due to diurnal warming and precipitation falling over the ocean surface. Diurnal cycles in salinity associated with diurnal rainfall are also observed. In Chapter 3, the upper ocean response to these rainfall events is examined. Fresh, near-surface lenses associated with rainfall are typically very shallow and short lived. Cooling of the near-surface from the freshwater input is also observed. Finally, in Chapter 4, the transfer of salt enhanced surface water into the deeper ocean via subduction is examined in the evaporation dominated North Atlantic subtropics. This is the process by which salty end member water moves away from its source region. Eddies were found to have a large impact via lateral induction and by forming gradients on which other processes can act.

References:

Allen, M. R., & Ingram, W. J. (2002). Constraints on future changes in climate and the hydrologic cycle. *Nature*, *419*(6903), 224–232.

Asher, W. E., Jessup, A. T., Branch, R., & Clark, D. (2014). Observations of rain-induced near-surface salinity anomalies. *Journal of Geophysical Research: Oceans*, n/a-n/a. https://doi.org/10.1002/2014JC009954

Bates, B., Kundzewicz, Z., & Wu, S. (2008). *Climate change and water*. Intergovernmental Panel on Climate Change Secretariat.

Bernie, D. J., Woolnough, S. J., Slingo, J. M., & Guilyardi, E. (2005). Modeling Diurnal and Intraseasonal Variability of the Ocean Mixed Layer. *Journal of Climate*, *18*(8), 1190–1202.

Boutin, J., Martin, N., Reverdin, G., Yin, X., & Gaillard, F. (2013). Sea surface freshening inferred from SMOS and ARGO salinity: Impact of rain. *Ocean Science*, *9*(1), 183.

Boutin, J., Chao, Y., Asher, W. E., Delcroix, T., Drucker, R., Drushka, K., … Ward, B. (2015). Satellite and In Situ Salinity : Understanding Near-Surface Stratification and Sub-footprint Variability. *Bulletin of the American Meteorological Society*. https://doi.org/10.1175/BAMS-D-15-00032.1

Clayson, C. A., & Bogdanoff, A. S. (2013). The Effect of Diurnal Sea Surface Temperature Warming on Climatological Air–Sea Fluxes. *Journal of Climate*, *26*(8), 2546–2556. https://doi.org/10.1175/JCLI-D-12-00062.1

Donlon, C. J., Minnett, P. J., Gentemann, C., Nightingale, T. J., Barton, I. J., Ward, B., & Murray, M. J. (2002). Toward Improved Validation of Satellite Sea Surface Skin Temperature Measurements for Climate Research. *Journal of Climate*, *15*(4), 353–369. https://doi.org/10.1175/1520-0442(2002)015<0353:TIVOSS>2.0.CO;2

Drucker, R., & Riser, S. C. (2014). Validation of Aquarius sea surface salinity with Argo: Analysis of error due to depth of measurement and vertical salinity stratification. *Journal of Geophysical Research: Oceans*, n/a-n/a. https://doi.org/10.1002/2014JC010045

Drushka, K., Asher, W. E., Ward, B., & Walesby, K. (2016). Understanding the formation and evolution of rain-formed fresh lenses at the ocean surface. *Journal of Geophysical Research: Oceans*, n/a-n/a. https://doi.org/10.1002/2015JC011527

Durack, P. (2015). Ocean Salinity and the Global Water Cycle. *Oceanography*, *28*(1), 20–31. https://doi.org/10.5670/oceanog.2015.03

Durack, P. J., Wijffels, S. E., & Matear, R. J. (2012). Ocean Salinities Reveal Strong Global Water Cycle Intensification During 1950 to 2000. *Science*, *336*(6080), 455–458. https://doi.org/10.1126/science.1212222

Held, I. M., & Soden, B. J. (2006). Robust Responses of the Hydrological Cycle to Global Warming. *Journal of Climate*, *19*(21), 5686–5699. https://doi.org/10.1175/JCLI3990.1

Kerr, Y. H., Waldteufel, P., Wigneron, J. P., Delwart, S., Cabot, F., Boutin, J., … Mecklenburg, S. (2010). The SMOS Mission: New Tool for Monitoring Key Elements ofthe Global Water Cycle. *Proceedings of the IEEE*, *98*(5), 666–687. https://doi.org/10.1109/JPROC.2010.2043032

Klingaman, N. P., Woolnough, S. J., Weller, H., & Slingo, J. M. (2011). The impact of finer-resolution air–sea coupling on the intraseasonal oscillation of the Indian monsoon. *Journal of Climate*, *24*(10), 2451–2468.

Lagerloef, G., Colomb, F. R., Le Vine, D., Wentz, F., Yueh, S., Ruf, C., … others. (2008). The Aquarius/SAC-D mission: Designed to meet the salinity remote-sensing challenge. *Oceanography*, *21*(1), 68–81.

Polson, D., & Hegerl, G. C. (2017). Strengthening contrast between precipitation in tropical wet and dry regions. *Geophysical Research Letters*, *44*(1), 2016GL071194. https://doi.org/10.1002/2016GL071194

Riser, S. C., Freeland, H. J., Roemmich, D., Wijffels, S., Troisi, A., Belbéoch, M., … Jayne, S. R. (2016). Fifteen years of ocean observations with the global Argo array. *Nature Climate Change*, *6*(2), 145–153. https://doi.org/10.1038/nclimate2872

Schanze, J. J., Schmitt, R. W., & Yu, L. L. (2010). The global oceanic freshwater cycle: A state-of-the-art quantification. *Journal of Marine Research*, *68*(3–1), 569–595. https://doi.org/10.1357/002224010794657164

Scheff, J., & Frierson, D. M. W. (2012). Robust future precipitation declines in CMIP5 largely reflect the poleward expansion of model subtropical dry zones. *Geophysical Research Letters*, *39*(18), L18704. https://doi.org/10.1029/2012GL052910

Skliris, N., Zika, J. D., Nurser, G., Josey, S. A., & Marsh, R. (2016). Global water cycle amplifying at less than the Clausius-Clapeyron rate. *Scientific Reports*, *6*, srep38752. https://doi.org/10.1038/srep38752

Woolnough, S. J., Vitart, F., & Balmaseda, M. A. (2007). The role of the ocean in the Madden–Julian Oscillation: Implications for MJO prediction. *Quarterly Journal of the Royal Meteorological Society*, *133*(622), 117–128. https://doi.org/10.1002/qj.4

Yu, L. (2010), On sea surface salinity skin effect induced by evaporation and implications for remote sensing of ocean salinity, *J. Phys. Oceanogr.,* 40(1), 85–102, doi:10.1175/2009JPO4168.1.

Chapter 2

Near-Surface variability of temperature and salinity in the near-tropical ocean: Observations from profiling floats

(This manuscript has been previously published as: Anderson, J. E., and S. C. Riser (2014), Near-surface variability of temperature and salinity in the near-tropical ocean: Observations from profiling floats, J. Geophys. Res. Oceans, 119, doi:10.1002/2014JC010112. Small changes have been made here for clarity and to fix typos.)

Abstract

Upper ocean measurements of temperature and salinity obtained from profiling floats equipped with auxiliary Surface Temperature and Salinity sensors (STS) are presented. Using these instruments, high vertical resolution (10 cm) measurements in the near-surface layer were acquired to within 20 cm of the sea surface, allowing for an examination of the ocean's near-surface structure and variability not usually possible. We examine the data from 62 Argo-type floats equipped with STS units deployed in the Pacific, Atlantic, and Indian Oceans. The vertical variability of temperature and salinity in the near-surface layer is characterized for each of these regions. While observations show the upper 4 m of the ocean are well mixed most of the time, this homogeneity is interrupted by significant and often short-lived warming/cooling and freshening events. In addition to the presence of barrier layers, a strong diurnal signal in temperature is observed, with salinity exhibiting somewhat weaker diurnal variations. The magnitude of the upper ocean diurnal cycle in temperature and salinity is largest in areas with

light winds and heavy precipitation and was found to decay rapidly with depth (~50% over the top 2 m). Storm events, validated from meteorological data collected from nearby TAO moorings and the Tropical Rainfall Measuring Mission (TRMM) satellite, show downward mixing of rainfall-derived freshwater to 10 m depth over only a few hours. Turner angle calculations show instability following these events.

2.1 Introduction

Historically, there has been a relative abundance of in situ sea surface temperature (SST) measurements (Kawai & Wada, 2007). Our knowledge of SST and our ability to obtain reliable SST measurements has improved over the years through the use of a variety of instrumentation (Kennedy, 2014). Starting in the 1980s, data from several SST satellites has further contributed to our understanding of the processes controlling SST. From these data sets, SST has been observed to vary greatly in both space and time (e.g., Soloviev & Lukas, 2006). Comparison of in situ observations, typically taken at depths of 1 m or more, and satellite data sets from the upper micrometers, has shown large variability and structure in the near-surface layer. Diurnal cycles of up to 5° have been observed not only in low and middle latitudes (Kawai & Wada, 2007) but also high latitudes (Eastwood et al., 2011; Kawai & Wada, 2007). During the intensive TOGA COARE experiment in the western Pacific warm pool, Soloviev and Lukas (1997) found that the amplitude of the diurnal warming was highly dependent on wind speed and precipitation. The largest diurnal cycles were found where insolation is high and winds were weak. During large diurnal warming events, the heat flux from the ocean has been observed to increase the net surface heat flux up to 50−60 W/m^2. Not incorporating the effect of the diurnal cycle in flux climatologies can lead to differences of 10 W/m^2 (Clayson & Bogdanoff, 2013). While several models of the diurnal cycle and vertical structure of SST provide a good baseline to examine the

relative importance of contributing forces, we lack enough detailed observations of both the vertical and temporal evolution of SST under a variety of conditions and surface forcing at fine enough temporal and spatial scales to validate them (Bernie et al., 2005; Soloviev & Lukas, 2006). A good model of diurnal warming and mixing is necessary to put interseasonal and annual observations in context.

In contrast, very little is known about near-surface salinity, primarily due to a marked lack of high quality data at the spatial and temporal resolution necessary to accurately characterize variability. Historically, sea surface salinity (SSS) has not been as extensively measured as SST largely due to a lack of ship-of-opportunity measurements (Bingham et al., 2002). Over the past decade the network of more than 3000 Argo floats has greatly enhanced our understanding of ocean salinity. To avoid potential surface fouling and ensure sensor stability over long time periods, standard Argo floats cease collecting measurements at a depth of about 4 m below the ocean's surface (Riser et al., 2008). The recent launches of the NASA Aquarius/SAC-D and ESA Soil Moisture and Ocean Salinity (SMOS) satellites will further enhance our understanding of salinity. With a 7 day repeat cycle, Aquarius provides estimates of SSS with an accuracy of 0.2 PSU on monthly time scales, at 150 km resolution (Lagerloef et al., 2008). The SMOS satellite has similar requirements for the SSS portion of its mission (Kerr et al., 2010). While these measurements will greatly expand our understanding of ocean salinity, the radiometric depth of satellite SSS measurements is on the order of a centimeter. There is therefore a need for accurate, near-surface data between the surface and 4 m so that the structure and variability between these two observational depths can be connected.

In addition to the larger-scale features observed by Aquarius and Argo, salinity also varies on much smaller temporal and spatial scales. A classic example of this is presented in Price (1979);

using shipboard CTD (conductivity/temperature/depth) instrumentation, localized freshening of the upper ocean of 0.25 PSU over several hours due to rainfall was observed to penetrate to depths of 25 m in less than 1 day. The spatial and temporal extent of storm events has been the subject of several studies. Using COARE enhanced TAO moorings in the tropical western Pacific, Cronin and McPhaden (1999) observed a diurnal cycle in salinity with an amplitude of 0.005 PSU at 1 m depth due to the mediation of preferential predawn rainfall by enhanced nighttime convection. More recent work by Drushka et al. (2014) observed diurnal salinity cycles of a similar magnitude across the tropics using data from moorings. The magnitude of rain induced fresh pools has also been observed to decay with depth (Reverdin et al., 2012) and to be highly dependent on rain rate and wind intensity (Henocq et al., 2010). The large-scale cumulative effect of this more localized rainfall-induced stratification was observed as a −0.1 PSU bias between SMOS and Argo over a 3 month period in the tropical western Pacific (Boutin et al., 2013). Similarly, global comparisons of Aquarius to Argo salinities from a depth of 5 m have also shown a negative bias of ~ −0.03 PSU due to rainfall within 15° of the equator (Drucker & Riser, 2014, this issue). It has been hypothesized that salinity may also have a positive (salt enriched) diurnal cycle in evaporation dominated regimes (Saunders, 1967) or regions with light winds further characterized by surface cooling (Yu, 2010). Calculations show the amplitude and overturning scale of these unstable, salt enriched layers to be much smaller than the effects of rainfall (Yu, 2010). Recent studies in the Atlantic salinity maximum region have observed the relatively small surface salinity response (Hodges & Fratantoni, 2014; Schanze et al., 2014).

The processes controlling upper ocean temperature and salinity are variable by region, and ultimately it is the balance between salt and temperature stratification that sets mixing and

circulation in the deeper ocean. When the halocline and thermocline are not at the same depth, stable layers such as barrier layers can form which inhibit vertical mixing by trapping surface fluxes within the shallower halocline and insolating the shallower halocline from entrainment cooling at the base of the deeper thermocline (Cronin & McPhaden, 2002; Lukas & Lindstrom, 1991; Soloviev & Lukas, 2006). Previous studies have shown that rain-induced near-surface salinity stratification greatly enhances the diurnal temperature amplitude (Soloviev & Lukas, 1997). An understanding of smaller scale SSS variability may enhance future models of SST variability, though salinity effects are of secondary importance to wind and insolation when modeling diurnal SST (Kawai & Wada, 2007).

The Global High Resolution Sea Surface Temperature (GHRSST) working group has formulated several sea surface temperature definitions in order to clarify which temperature is being used for analysis of air-sea interactions. From shallowest to deepest, they are: interface, skin, subskin, SST at a depth, and foundation temperatures (Donlon et al., 2002). The interface temperature is theoretical and has not been observed; satellites are thought to measure the skin and subskin SSTs. Following the launch of Aquarius and SMOS, it is of use to similarly formulate several definitions of SSS, although this has not yet been done and is beyond the scope of this paper. In order to capture the full vertical variability of SST and SSS, high vertical resolution measurements on the order of centimeters is needed. This is especially important in the highly variable region between the skin SST/SSS and SST/SSS at depth in situ measurements. Direct intercomparison between satellite and in situ SST/SSS will require in situ measurements in the upper 1 cm, which remain difficult to reliably obtain.

Here we present new observations of temperature and salinity variability, mixing, and diurnal cycles in the near-surface layer of the ocean. To investigate the variability and structure of

temperature and salinity at smaller scales, we have employed Argo-type floats equipped with an auxiliary Surface Temperature and Salinity (STS) CTD unit capable of making high vertical resolution measurements (10 cm) nearly all the way to the sea surface (~20 cm). After describing the operation and accuracy of these new sensors, we present near-surface observations from floats deployed in the Atlantic, Pacific, and Indian Oceans. The vertical structure and variability due to atmospheric effects, as well as active diurnal cycles in both temperature and salinity will be presented, and the effect of stratification on mixing will be determined using Turner angle calculations.

2.2 Data Description

2.2.1 *The STS Sensor*

Near-surface measurements of temperature and salinity used in this study were obtained using Argo-type profiling floats equipped with an auxiliary, unpumped, surface temperature and salinity (STS) CTD manufactured by Seabird Electronics, Inc. A standard, primary, pumped SBE 41CP CTD unit is also installed on the float inline with the secondary STS unit. Initial deployment of an STS enhanced float showed the in situ precision of the STS unit to be 0.004°C and 0.005 PSU (Murphy, 2008). In situ accuracy of the STS sensor, as determined via comparison with the primary SBE 41CP CTD, is discussed in section 2.3.1. Seabird Electronics, Inc. uses the same protocols to calibrate both the primary SBE 41CP CTD (C. Janzen et al., Accuracy and stability of Argo SBE 41 and SBE 41CP CTD conductivity and temperature sensors, Seabird Electronics, unpublished technical paper, 2008) and the STS CTD using well-controlled baths. The STS CTD, by design, remains unpumped during calibration and is calibrated alongside the primary CTD. No additional calibrations to the STS unit are done prior to deployment. The STS equipped floats were fabricated at the University of Washington from

components purchased from Webb Research and Seabird Electronics, Inc. Shown in Figure 2.1 is a typical Argo-type float endcap with both CTDs installed. A typical profile collected from an STS equipped float is shown in Figure 2.2.

2.2.2 *STS Float Operation*

Between the depths of 2000 m and 30 m, STS equipped floats operate almost identical to typical Argo-type floats, with only the primary SBE 41CP CTD collecting data at a rate of 1 Hz as the float ascends at a rate of about 8 cm/s, then averaging these data into 2 m bins. The only change to the operation of STS equipped floats below 30 m is that at around 1000 m, the secondary STS unit operates in tandem with the SBE 41CP CTD briefly (approximately 30 m), providing the opportunity to compare the STS unit to the main CTD at a location in the water column where temperature and salinity typically have little vertical variation. From 30 m to 4 m, both the auxiliary STS unit and the SBE 41CP CTD collect 1.5 Hz measurements as the ascent rate slows, resulting in STS measurements approximately every 10 cm. At a depth of 4 m, the main SBE 41CP unit shuts off while the STS unit continues to operate at 1 Hz the rest of the way to the sea surface. Shutting off the primary SBE 41CP at depths above 4 m prevents surface fouling and maintains the stability of the primary CTD over time; recovered floats have generally shown only very small drifts in the SBE 41CP temperature and salinity sensors (Oka, 2005). Since the STS unit operates all the way to the sea surface, it is expected that it may drift over time, but this drift can be removed by using the concomitant data from the proven, stable primary CTD unit.

2.2.3 *Deployment Locations*

Included in this study are 62 STS equipped floats deployed in the Atlantic, Pacific, and Indian Oceans between December 2007 and January 2013. The majority of floats were deployed at low

latitudes, in order to be used in conjunction with the Aquarius/SAC-D satellite mission, since the accuracy of Aquarius is greatest at higher temperatures due to a weaker radiometric signal at low temperatures (Lagerloef et al., 2008). Additionally, the largest temperature and salinity variations between the sea surface and a depth of 4 m are expected to be found in low wind, high precipitation regimes (Henocq et al., 2010), and thus many of these floats were deployed in the Intertropical Convergence Zone (ITCZ) and in regions with strong monsoon cycles. A large number of floats were also deployed in the Atlantic Ocean in the first NASA-sponsored Salinity Processes in the Upper Ocean Regional Study (SPURS-1) area. Deployment locations and float trajectories for all STS floats use in this study are shown in Figure 2.3. Additionally, information about deployment dates and locations is provided in Table 2.1.

2.2.4 *Fast Cycle*

The Iridium satellite system was used for communications for all STS-equipped floats. This allows increased data transmission from multiple sensors as well as two-way communication with the floats, allowing the mission of the float to be changed after deployment. For most of their life the 62 STS-equipped floats used in this study operated with a typical Argo-type mission, drifting at 1000 m, then descending to 2000 m and collecting a full depth profile to the surface while ascending, at intervals of 10 days. For the 15 of the 62 STS-equipped floats in this study, indicated by triangles in Figure 2.3, both the time interval and maximum depth of the float profile were temporarily (several days to several months) altered in order to collect profile data between approximately 150 m and the surface at intervals of about 2 h. This faster, shallower profiling allows for investigation of shorter-lived upper ocean processes. Data from these 15 floats programmed to cycle rapidly are presented here and are put into context by using the data collected from all 62 STS-equipped floats under a standard, 10 day profiling scheme.

2.2.5 *Other Data Sets*

To place the observed near-surface temperature and salinity measurements in context, a variety of data sources were used to obtain meteorological and larger-scale oceanic data. Meteorological data assimilated and computed by the National Centers for Environmental Prediction (product NCEP-DOE AMIP-II Reanalysis) were used to provide an estimate of the incident insolation and wind speed. These data were available in 6 hourly intervals on a Gaussian T62 grid (1.875° resolution at the equator). For each location and time of a float profile, the closest AMIP-II value in time and space was used for the analysis providing the surface conditions in the broader region around the float profile. Additionally, several floats on fast cycle missions passed close to moorings deployed as part of the TAO project. In these instances, hourly wind speed, precipitation, and atmospheric data were obtained from enhanced moorings. Finally, collocated rainfall data along the float trajectories were obtained from the TRMM satellite (product 3B42). TRMM operates on a nonsun synchronous circular orbit that allows for 3 hourly estimates of rainfall at 0.25° grid resolution. Using data within 0.5° of float profile location, TRMM data were linearly interpolated for each profile using a one-dimensional interpolation in time between 3 hourly estimates, followed by a two-dimensional interpolation in space.

2.3 STS Data Processing/Data Quality

2.3.1 *Data Quality*

Data from STS floats used in this study were subjected to intensive quality control. Using tests slightly adapted from the International Argo Program, all STS data were checked for gradient errors, outliers, and spikes (Wong et al., 2013). Adjustments to the surface pressure (normally

assumed to be essentially zero during the data transmission phase on all Argo floats) were not made, as the STS floats sample in the surface wave zone and there was a desire to preserve this information. As the STS floats surface, spiking can occur in the salinity record as the float encounters air bubbles very near the air-sea interface. All temperature and salinity data collected during ascent after a near-surface salinity spike was detected (indicated by an increase of greater than 1 PSU over a 0.1 dbar interval) were discarded. This reduction results in the shallowest surface measurement being generally between 0.1 and 2.7 m below the surface, depending upon location and profile number. One float, deployed in the Bay of Bengal, was unable to reach the surface for several days, resulting in no measurements above ~20 m depth during that period.

Additionally, the auxiliary temperature and conductivity sensors on some STS units were found to drift over time, which was determined by comparing the STS data to the overlap data from the main SBE 41CP CTD unit. Measurement differences between the two sensor suites were small for most floats though a few floats showed larger drift. This drift was observed to accelerate during fast cycle profiling periods and was likely the result of enhanced sensor fouling due to increased exposure to the near the surface layer (the main CTD unit is pumped and contains a biocide, nearly eliminating the possibility of significant drift, while the STS unit is unpumped without biocide). STS unit sensor drift was corrected using data from the deep overlap section of the profiles where the typical vertical variability of both temperature and salinity is small. An offset (estimated as an amount of drift per profile) was used to adjust the STS unit temperature to the SBE 41CP unit temperature. For salinity, a mean conductivity ratio between the two sensors was found on each profile, and this was used to adjust for differences between the two sensors, with the salinity recalculated after this conductivity adjustment was made. Analysis of 11,269 profiles from 62 floats deployed between 2007 and 2013 shows the average difference between

the two sensors to be 0.009 ± 0.013°C and 0.018 ± 0.028 PSU. A small subset of STS floats was discovered to have a minor leak in the STS thermistor, indicated by a rapid increase in the temperature offset. Data from these floats were subjected to more intensive quality checks and were omitted from this study when the offset became too large.

While profiling through the sea surface, the STS enhanced Argo floats often record multiple temperature and salinity measurements at a single pressure as ocean surface waves cause the floats to oscillate vertically. For this study (and as outlined in the Argo Quality Control Manual), in regions of constant pressure only the first recorded temperature and salinity measurements at a single pressure were used. Following pressure reversals, the first reading at a single pressure were also used which may introduce small distortions to the near-surface measurements. In the case of small gaps in measurements, data were put on a standard, 10 cm resolution depth grid between 0 and 30 m (0 and 150 m during fast cycle periods) using linear interpolation. These full, reconstructed profiles were used in our analysis.

2.4 Results

2.4.1 *Near-Surface Variability and Structure*

To gain a better understanding of the near-surface variability of temperature and salinity, we have compared the near-surface observations to those at depth. Two comparisons were made. The first, the difference between data values at a depth of 4 m and data at the shallowest, near-surface measurement, provides information on how comparisons between standard Argo float data with that collected by satellites may be biased in certain situations. The second, the difference between 15 m and each shallower depth (at 10 cm increments), provides information about the amplitude and structure of the near-surface variability and its decay with depth under a variety of conditions.

2.4.1.1 *Differences From 4 m*

Shown in Table 2.2 is the difference between STS temperature and STS salinity at 4 m from the shallowest observation obtained from each profile. A depth of 4 m was chosen since the majority of the 3,600 Argo floats currently deployed ceased collecting data at that depth in order to insure sensor stability over time. The shallowest observation available varied between each profile and float but generally was within 0.2 dbar, approximately 0.2 cm (0.17 dbar average over 11,269 profiles) of the sea surface. Small regional differences in the depth of the shallowest measurement were seen. Floats deployed in the Pacific Ocean were generally able to sample the closest to the sea surface, followed by those deployed in the Atlantic and Indian Oceans. This is likely a result of both sea state and near-surface stratification−larger sea states may cause near-surface air bubbles deeper in the water column resulting in salinity spikes while strong near-surface stratification can prevent the float from reaching the surface. Across all 62 floats and 11,269 profiles, the difference between temperature at these two depths is less than ±0.1°C in 87% of the cases examined (mean difference 0.012 ± 0.164°C). For salinity, the difference is less than ±0.1 PSU in 97% of the cases (mean difference −0.023 ± 0.096 PSU). This implies that the upper 4 m (actually between a depth of about 20 cm and 4 m) of the ocean is nearly always well mixed to this degree. This suggests that there should generally be only small differences between SST and SSS estimates made from satellites and those made from the ~3°, 10 day resolution array of 3,600 Argo floats.

While these differences are usually small for both temperature and salinity over 87/97% of the time, large differences are sometimes observed and it is still important to understand in which locations and under what conditions more variability near the sea surface exists. For example, if we subdivide the floats by region based on major ocean basin, it is apparent that floats located in

the Indian Ocean show large differences in the upper 4 m more frequently than those in the Atlantic and Pacific Oceans (Table 2.2). Indeed, the mean temperature difference for Indian Ocean floats is increased to 0.022 ± 0.086°C versus 0.007 ± 0.042°C and 0.005 ± 0.069°C for Atlantic and Pacific floats, respectively. Additionally, data from UW float 6117, deployed in the tropical western Pacific, show a reduction in the percentage of profiles with near-surface differences within ±0.1°C/PSU to 73% and 89%, respectively. The Pacific Ocean floats have the largest mean difference at –0.002 ± 0.016 PSU. Larger temperature differences are also seen in floats within the SPURS-1 study area, likely due to enhanced near-surface stability resulting from evaporation in this salinity maximum region.

To first order, the source of heat that results in an SST increase (ignoring advection) is solar insolation. 50-65% of solar radiation is absorbed in the upper 1 m of the ocean (e.g, Soloviev & Lukas, 2006). NCEP net downward shortwave radiation incident at the surface was used to examine this controlling variable. Gridded NCEP data were collocated to the float profiles using the closest values in both time and location (latitude and longitude). Top of the atmosphere shortwave radiation is at a peak during the daytime. At the surface, however, the time of peak can vary due to clouds. Shown in Figure 2.4 is the difference between the shallowest measurement depth and 4 m versus NCEP shortwave radiation estimates. The largest 4 m differences in temperature are not found when solar insolation is the largest, likely the result of a time lag between incident radiation and SST increase. Solar insolation absorbed at the surface does not immediately mix downward into the stable water column. Under light wind conditions it can take several hours for the heat to be transferred to depths below (Minnett, 2003). Salinity does not appear to vary linearly with solar insolation, which is not unexpected as negative (rain-induced) salinity differences could be coincident with a large range of solar insolation

values−clouds associated with rainfall events reduce incident shortwave radiation and both broader scale stratiform rainfall and more localized convective rainfall can occur at various times of the day depending on location (Janowiak et al., 1994; Kikuchi & Wang, 2008; Nesbitt & Zipser, 2003; Yang & Smith, 2006, 2008). For example, in locations where there is preferential predawn rainfall due to convective systems or costal effects, negative biases could occur since shortwave is low due to both time of day (pre-dawn) and the presence of clouds.

Previous studies have also shown upper ocean variability to be highly dependent on wind speed (Donlon et al., 2002; Soloviev & Lukas, 1997). NCEP zonal and meridional wind speeds collocated with the float profile in the same manner as shortwave radiation were used to examine the dependence of SST and SSS on the total wind speed. Plotted in Figure 2.5 are the differences from 4 m of SST and SSS versus wind speed; for both SST and SSS, above wind speeds of ~6−10 m/s the water column is well mixed, with the majority of the larger differences occurring with wind speeds of ~6 m/s or less, consistent with Donlon et al. (2002) and Gille (2012). Additional comparisons for float 6117 with nearby TAO mooring data (not shown) also indicate that below 6 m/s differences are small.

2.4.1.2 *Differences From 15 m*

Shown in Figure 2.6 are the differences in near-surface temperature and salinity referenced to a depth of 15 m, estimated at 10 cm intervals for all profiles collected from December 2007 to December 2013. The reference depth chosen (15 m) is arbitrary, with the criteria that it be generally deeper than the diurnal mixed layer. To examine the variability in vertical structure by region, the 62 floats were grouped by ocean basin (as was done for the 4 m differences). For temperature, a positive difference indicates that the surface is warmer than that at 15 m. Negative

salinity differences indicate a freshening near the sea surface while positive differences indicate that the near-surface layer has become saltier.

As can be seen in Figure 2.6, across all floats and all regions, for the majority of profiles, the upper ocean is well mixed all the way to 15 m. For profiles where large temperature differences are observed (up to 5°), they are generally confined to the upper 5 m. For these larger events, there is a rapid decay with depth, with the surface difference being reduced by more than half at a depth 5 m. Below 5 m, the vertical decay is less rapid. The differences in SST are generally positive, implying that it is the result of daytime heating. The majority of positive differences occur between 1100 and 1900. Negative differences are likely due to cooling from rainfall (either from the drops themselves or by entrainment of cooler subsurface water from the precipitation event).

Similarly, salinity differences of 2 PSU (occasionally as large as 6 PSU) are also found primarily in the upper 2 m. Salinity signals also show a rapid decay with depth. With the exception of a few of the largest events, the negative salinity differences are associated with rainfall events, with the rate of decay varying with the local conditions (the upper ocean response to the rainfall events will be examined in section 2.4.4). The slight positive bias in salinity is of the same order of magnitude of the STS sensor accuracy, and therefore positive salinity differences due to evaporation were not unequivocally observed.

While the upper ocean is well mixed the majority of the time, large diurnal warming events and large surface stratification due to rainfall are observed in all three ocean basins. The vertical structure for larger positive events is similar in all ocean basins. While the Atlantic and Pacific floats rarely show negative (cooling) SST differences, such vertical gradients are common in the Indian Ocean, likely the result of increased, heavy rainfall during the monsoon season, as well as

river input for the floats located in the northern Bay of Bengal. Negative SSS differences again have a similar structure for the Atlantic and Pacific Ocean floats, with the most stratified profiles showing a rapid decrease in the upper ~3 m. In the Indian Ocean, the negative salinity differences are more abundant, decay less rapidly with depth, and are mixed vertically further into the water column. Again, these differences are likely the result of increased heavy rainfall and winds associated with the monsoon and influence of river runoff.

2.4.2 *The Diurnal Cycle*

To further investigate the influence of the diurnal cycle on the near-surface structure, 15 floats (indicated by triangles in Figure 2.3) had their mission configuration altered to profile only over the upper 150 m, at intervals of approximately 2 h; this configuration was allowed to continue for at least 8 days, and in a few cases for over 4 months. Shown in Figure 2.7 are data from the primary SBE 41CP sensor for the entire record of one of these floats (6117), which was deployed, in the tropical western Pacific. The blank, white region in this plot between 24 June 2009 and 15 July 2009 indicates when the float mission was altered (via Iridium) to cycle between the sea surface and a depth of 150 m at intervals of between 2 and 2.5 h. Floats were chosen to execute a fast cycle due to their location within precipitation dominated regimes and/or proximity to moorings so the influence of local oceanic and atmospheric conditions could be examined. Diurnal forcing due to solar insolation (with a time lagged response) heavily influences the near-surface temperature structure, with wind also having a significant effect. While a response in salinity due to evaporation is not observed by any of the floats, the effects of rainfall are apparent for those located in the tropical western Pacific and the Indian Ocean. Past studies have indicated that over the ocean there is a quasi-diurnal cycle in incident rainfall due to the increased likelihood of convective systems that vary in intensity with location (Kikuchi &

Wang, 2008; Nesbitt & Zipser, 2003; Yang & Smith, 2008). Previous studies have observed an apparent diurnal salinity response to this diurnally timed rainfall forcing, which is then modulated by an increase in entrainment at nighttime due to convective cooling (Cronin & McPhaden, 1999; Drushka et al., 2014).

Time series plots (e.g., Figure 2.8) of temperature and salinity from 15 floats show a diurnal response in temperature in all locations, with freshening due to rainfall being observed less frequently. The intensity, depth of penetration, and time lag of the upper ocean temperature and salinity responses varies between locations and with the location conditions. Plotted in Figure 2.8 are data from the secondary STS unit CTD as functions of time and depth for float 6117 during the fast cycle period. The near-surface data (0−5 m) from the STS sensor during this 3 week period show a clear diurnal temperature signal of up to 1.5°C in the upper 5 m of the water column, with a less pronounced daily cycle in salinity (though some diurnal variability is apparent). In most cases, the upper 5 m variability (in both temperature and salinity) occurs nearly coincidently in time over the layer.

To confirm the diurnal cycles identified in the time depth plots, the power spectrum was computed at depths of 0.5, 3.0, and 10 m for all fast cycle floats, with the power spectrum for float 6117 shown in Figure 2.9. While temperature for float 6117 shows a clear diurnal response through the upper 10 m, decaying with depth, salinity exhibits a more broadband diurnal response confined to the sea surface. This peak at the 24 h band was seen for all 15 fast cycle floats in temperature, although it did not penetrate to a depth of 10 m in all locations. A significant peak at the 24 h band in salinity was observed by only three floats: 5131 deployed near Hawaii, and floats 6115 and 6117 deployed in the tropical western Pacific (150−160E). Surprisingly, the third Pacific float, 5066, does not show a diurnal cycle in salinity. This float is

located further east in the basin, farther from land (along 180° meridian). This is consistent with the results of Drushka et al. (2014) who also observed a decreased amplitude in the diurnal salinity at this longitude from moored observations.

To obtain a greater understanding of the response at depth in salinity and temperature, a composite diurnal vertical profile was constructed using data collected during the fast cycle mission. While the length of the fast cycle varies between floats, for all floats the fast cycle was short enough to assume that it was representative of the local environment in the particular season when the data were collected. Composites were computed using temperature and salinity anomalies, defined as the difference from the fast cycle record length mean temperature and salinity at each depth. The anomalies were then binned into 2 h local-time-of-day bins and the mean amplitude of the composite determined for each 10 cm vertical grid point; the composite diurnal cycle for float 6117 is shown in Figure 2.10. Diurnal warming due to insolation reaches its peak of 0.29°C at the surface at 1500 local time. The magnitude of the diurnal cycle decreases with depth and is reduced to 0.07°C by 4 m. There is also a time lag with depth, with the peak of 0.07°C at 4 m occurring at 1700 local time, a lag of 2 h. Salinity also exhibits a diurnal cycle, with maximum freshening of −0.07°C occurring at 1500 in the afternoon (local time). The maximum freshening is not concurrent with the maximum rainfall, which occurs at 0700. The predawn rainfall's effect on the SSS appears to be modulated by the entrainment of saltier water from below. The time lag of temperature anomalies with depth was larger in the tropical western Pacific and the SPURS-1 study area (which also had larger amplitude diurnal SST signals). In locations that are typically windy and/or more likely to have strong advection (such as near Hawaii), the SST anomalies were concurrent (or within the same 2 h bin) in time through the

upper 5 m. Not all locations exhibited a diurnal cycle in salinity while others exhibited diurnal cycles consistent with diurnal entrainment.

Using the range of the positive and negative anomalies at each depth, the magnitude of the diurnal cycle was computed for each float. Figure 2.11 shows the amplitude of the diurnal cycle in temperature and salinity for all 15 floats. The largest diurnal temperature amplitudes are found in the precipitation dominated regions of the tropical western Pacific and the Bay of Bengal. Diurnal salinity signals are only seen in regions with a time-of-day diurnal rainfall preference. The very large salinity diurnal signal seen in float 7092 located in the northern Bay of Bengal (18.03°N, 89.52°E) is also likely the result of river input.

2.4.3 *Storm Events*

Using spectral analysis and compositing of the fast cycle data, we have thus far examined the average response of the near-surface SST and SSS to precipitation. We now turn our attention to an analysis of individual rain events and the resulting upper ocean response over a period of a day in order to obtain a more detailed view of the effects of rain on the vertical structure of the water column. On 3 July 2009 float 6117 captured a short-lived response to one event (Figure 2.12). The top plot shows the hourly air temperature and the plot below shows the hourly wind speed and direction during this event as observed by the TAO mooring located at 2°N, 147°E. The third plot shows rainfall as observed by TRMM (3 hourly). TRMM data were collocated to float profiles by first doing a one-dimensional linear interpolation in time and then a two-dimensional linear interpolation in location. Temperature and salinity in the upper 15 m from the SBE STS CTD are shown in bottom two plots. Contour lines are at 0.10 °C/PSU intervals. Prior to the storm event, the upper 15 m of the water column are well mixed; however, following a cumulative rainfall total of 19 mm, the upper meter of the water column freshens by

approximately 0.15 PSU. The fresh pool begins to mix downward within hours of forming and the upper 15 m of the water column is fully mixed again 12 h after the conclusion of the storm. A depression in air temperature following the storm event is also observed.

The total rainfall (19 mm) during the 3 July event is less than half the rainfall (60 mm) observed by Price (1979) and results in a smaller salinity depression and depth of penetration (0.15 PSU in 15 m) than that observed by Price (1979) (0.25 PSU in 25 m); the upper ocean response is clearly not linear and depends heavily on winds and preexisting stratification. This is seen by examining the other rain events captured in detail by float 6117 during its fast cycle mission on 10-11 July and 12-15 July (Figure 2.8). The total rainfall and associated freshening are 7 mm/0.6 PSU and 50 mm/0.3 PSU, respectively, a clearly non-linear relationship between rainfall rate and freshening. A simple mass balance also does not represent the observed freshening well. Hundreds of rainfall events have been captured by the STS-equipped floats and a detailed analysis of these storm-related events will be the subject of a future work. More insight into the dynamics of the stratification can be determined by calculating the Turner angle, which is discussed in the next section.

2.4.4 *Turner Angle Calculations*

Turner angles are similar to the density ratio ($Rp = \alpha\theta/\beta S$, variables defined below), in that they provide a means of examining the relative contributions of temperature and salinity to the density, or stability of the water column. They have the added benefit of removing some of the ambiguity related to the relative strength of the diffusion and salt fingering that may be present in the water column (Ruddick, 1983). The Turner angle is calculated as the four quadrant arctangent,

$$Tu(deg) = \tan^{-1}\left(\alpha\frac{\partial\theta}{\partial z} - \beta\frac{\partial S}{\partial z}, \alpha\frac{\partial\theta}{\partial z} + \beta\frac{\partial S}{\partial z}\right) \quad (2.1)$$

where α is the coefficient of thermal expansion and β is the coefficient of saline contraction, z is the depth, and θ and S are the temperature and salinity at some depth below the sea surface. Turner angles between –45° and 45° are stable, with both temperature and salinity being stably stratified. For all other angles, the water column is unstable with, angles in the range –90 ° to –45° and 45° to 90° being prone to diffusion and salt fingering, respectively.

Calculation of the Turner angle for float 6117's fast cycle period between 24 June 2009 and 15 July 2009 shows strong instability in the water column during and immediately after the 3 July 2009 storm event (Figure 2.13). As the water column becomes unstable, the depth of the diffusion is enhanced. In the days following the rainfall event, a strong stable region forms between 20 and 80 m with enhanced salt fingering. Mixed layer depth calculations have identified this stable region as a barrier layer, a common feature in the western tropical Pacific region where float 6117 was deployed. Following the 10-11 July and 12-15 July events, Turner angle calculations do not show as much instability, with the 10-11 July event showing slightly enhanced diffusion and the 12-15 July event being relatively stable with some indication of salt fingering. This difference in stability can be partially explained by looking at the temperature and salinity in the water column during these events (Figure 2.8). Both the 10-11 July and 12-15 July events show enhanced diurnal warming, contained to the near-surface layer. This contributes stability to the water column, which is reflected in the Turner angle.

2.5 Discussion and Conclusions

Difference calculations using two separate criteria have shown that over 80% of the time the near-surface temperature and salinity above a depth of 4 m are well mixed over the tropical

ocean, implying that using Argo floats in the tropics to validate satellite measurements will likely not produce a significant difference. This finding agrees with those of Henocq et al. (2010), who found the upper ocean difference between 10−5 m, 5−1 m, and 10−1 m to be small in most cases. We also find the differences to be highly dependent on wind speed. Below wind speeds of ~10 m/s both large and small differences are observed though the largest differences are only observed when winds are less than ~6 m/s. When the wind speed is above ~10 m/s, the water column appears to mix to at least a depth of 15 m in all ocean basins sampled.

In the few cases where the upper ocean is not well mixed, vertical temperature and salinity profiles show an interesting variety of structures. Profiles captured in light winds, following a rain event, show a strong decay with depth in salinity. Likewise, strong diurnal warming events also show a rapid decrease with depth as was observed by Gille (2012). It is apparent from concurrent observations of large diurnal warming events and near-surface salinity depressions that stability gained via fresh water input at the surface, if allowed to persist under light wind conditions, results in an amplified diurnal temperature signal. This amplification, previously observed by Soloviev and Lukas (1997), is due to more heat being “trapped” in the stably stratified surface layer. The locations where strong near-surface stratification are more likely are the tropical western Pacific and the Bay of Bengal, locations that were both identified by Boutin et al. (2013) and Drucker and Riser (2014, this issue) as having significant negative salinity biases. Our study confirms the findings of Reverdin et al. (2012) with a rapid decrease in intensity with depth.

Use of a fast cycle mission profiling schema on the STS equipped floats also allowed for an examination of the diurnal cycles of temperature and salinity in the near-surface layer and the ocean response to rainfall. The amplitude of the diurnal temperature cycles are on the same order

of magnitude as previously observed (Kawai & Wada, 2007). New estimates of a the magnitude of a precipitation and entrainment driven salinity diurnal cycle are slightly larger (~ 0.05 PSU at 1 m) but on the same order of magnitude with calculations from Cronin and McPhadden (1999) and Drushka et al. (2014) using mooring data (~0.01 PSU at 1 m) and those of Reverdin et al. (2012) using drifter data. The slightly larger 1 m values are likely the result of our tropical western Pacific floats executing their fast cycle missions during the month of July. The high vertical resolution of the STS floats allows us to extend our estimates closer to the sea surface. The diurnal salinity response was significantly larger closer to the sea surface (~0.1 PSU). In general, diurnal salinity signals were only observed in regions with a tendency for diurnal rainfall due to mesoscale convective systems (Nesbitt & Zipser, 2003; Yang & Smith, 2008) or coastal effects (Kikuchi & Wang, 2008). Using TRMM rainfall data, Nesbitt and Zipser (2003) showed rainfall over the ocean only exhibits a diurnal signal when these systems are the source of the rainfall (versus localized convection which has a smaller footprint). More recent studies also using TRMM data (with less smoothing) have also shown that larger scale convection and/or rainfall propagating from its initiation region near the ocean/land boundary is the dominant source of diurnal rainfall (Kikuchi & Wang, 2008; Yang & Smith, 2008). Novel observations of rain events captured by STS enhanced floats provide a valuable dataset to be used in quantifying and developing better dynamical models of the near-surface layer, with Turner angle calculations providing a first look at the delicate balance between temperature and salinity in maintaining stratification in the near-surface layer.

The addition of the STS sensor to typical Argo floats has allowed for a detailed examination of the surface layer that is usually not possible in the context of Argo. High-resolution data in the near-surface region show that while the upper ocean is well mixed in both temperature and

salinity the majority of the time, significant warming and freshening occurs on daily and hourly time scales. These significant events are more likely to occur when wind speeds are less than ~6 m/s. The largest variability in both temperature and salinity is found in low wind and/or high precipitation regimes such like the tropical western Pacific and the monsoon-affected Indian Ocean. It was found that enhanced stability associated with rainfall events results in larger than normal diurnal warming events. Additionally, if rainfall occurs at nearly the same time every day, a diurnal cycle in salinity can occur. A salinity diurnal cycle due to evaporation was not found, likely due to it being smaller in magnitude or nearer to the sea surface than can be observed with the STS sensor. While it is unlikely that the use of standard Argo 4 m data to validate satellite measurements will result in a significant bias, the observations of larger, though occasional, variability captured by STS enhanced floats and presented here provides a rare opportunity to understand the near-surface vertical dynamics as they evolve in time. Future work using STS float and surface drifter data to more quantitatively describe the upper ocean stratification balance on light wind days and following rainfall could help refine upper ocean models as well as help put observed satellite biases in context.

Acknowledgments:

STS data used in this study are available at http://flux.ocean.washington.edu/. TAO data were obtained via http://www.pmel.noaa.gov/tao/jsdisplay/. NCEP Reanalysis data were obtained from http://www.esrl.noaa.gov/psd/. TRMM (product 3B42) was obtained from ftp://trmmopen.gsfc.nasa.gov/trmmdata/ByDate/V07. Support for this work was generously supported through NASA grants NNX09AU71G and NNX11AF79G to the University of Washington. The STS floats used in this study were fabricated at the University of Washington

by the skilled UW float group of Dana Swift, Dale Ripley, Rick Rupan, and Greg Brusseau. An additional thank you to Dana Swift and Annie Wong for guidance and thoughts on STS data processing and Robert Drucker for providing collocated TRMM data.

References:

Bernie, D. J., S. J. Woolnough, J. M. Slingo, and E. Guilyardi (2005), Modeling diurnal and intraseasonal variability of the ocean mixed layer, *J. Clim.*, 18(8), 1190–1202, doi:10.1175/JCLI3319.1.

Bingham, F. M., S. D. Howden, and C. J. Koblinsky (2002), Sea surface salinity measurements in the historical database, *J. Geophys. Res.*, 107(C12), 8019, doi:10.1029/2000JC000767.

Boutin, J., N. Martin, G. Reverdin, X. Yin, and F. Gaillard (2013), Sea surface freshening inferred from SMOS and ARGO salinity: Impact of rain, *Ocean Sci.*, 9, 183–192, doi:10.5194/os-9-183-2013.

Clayson, C. A., and A. S. Bogdanoff (2013), The effect of diurnal sea surface temperature warming on climatological air–sea fluxes, *J. Clim.*, 26(8), 2546–2556, doi:10.1175/JCLI-D-12-00062.1.

Cronin, M. F., and M. J. McPhaden (1999), Diurnal cycle of rainfall and surface salinity in the western Pacific warm pool, *Geophys. Res. Lett.*, 26, 3465–3468, doi:10.1029/1999GL010504.

Cronin, M. F., and M. J. McPhaden (2002), Barrier layer formation during westerly wind bursts, *J. Geophys. Res.*, 107(C12), 8020, doi:10.1029/2001JC001171.

Donlon, C. J., P. J. Minnett, C. Gentemann, T. J. Nightingale, I. J. Barton, B. Ward, and M. J. Murray (2002), Toward improved validation of satellite sea surface skin temperature measurements for climate research, *J. Clim.*, 15(4), 353–369, doi:10.1175/15200442(2002)015<0353:TIVOSS>2.0.CO;2.

Drucker, R., and S. C. Riser (2014), Validation of Aquarius sea surface salinity with Argo: Analysis of error due to depth of measurement and vertical salinity stratification, *J. Geophys. Res. Oceans*, 119, 4626–4637, doi:10.1002/2014JC010045.

Drushka, K., S. T. Gille, and J. Sprintall (2014), The diurnal salinity cycle in the tropics, *J. Geophys. Res. Oceans.*, 119, 5874–5890, doi:10.1002/2014JC009924.

Eastwood, S., P. Le Borgne, S. Pere, and D. Poulter (2011), Diurnal variability in sea surface temperature in the Arctic, *Remote Sens. Environ.*, 115(10), 2594–2602, doi:10.1016/j.rse.2011.05.015.

Gille, S. T. (2012). Diurnal variability of upper ocean temperatures from microwave satellite measurements and Argo profiles, *J. Geophys. Res.*, 117, C11027, doi:10.1029/2012JC007883.

Henocq, C., J. Boutin, G. Reverdin, F. Petitcolin, S. Arnault, and P. Lattes (2010), Vertical variability of near-surface salinity in the tropics: Consequences for L-band radiometer calibration and validation, *J. Atmos. Oceanic Technol.*, 27(1), 192–209, doi:10.1175/2009JTECHO670.1.

Hodges, B. A., and D. M. Fratantoni (2014), AUV observations of the diurnal surface layer in the North Atlantic salinity maximum, *J. Phys. Oceanogr.*, 44, 1595–1604, doi:10.1175/JPO-D-13-0140.1.

Janowiak, J. E., P. A. Arkin, and M. Morrissey (1994), An examination of the diurnal cycle in oceanic tropical rainfall using satellite and in situ data, *Mon. Weather Rev.*, 122(10), 2296–2311, doi:10.1175/1520-0493(1994)122<2296:AEOTDC>2.0.CO;2.

Kawai, Y., and A. Wada (2007), Diurnal sea surface temperature variation and its impact on the atmosphere and ocean: A review, *J. Oceanogr.*, 63(5), 721–744, doi:10.1007/s10872-007-0063-0.

Kennedy, J. J. (2014), A review of uncertainty in in situ measurements and data sets of sea surface temperature, *Rev. Geophys.*, 52, 1–32, doi:10.1002/2013RG000434.

Kerr, Y. H., P. Waldteufel, J. P. Wigneron, S. Delwart, F. Cabot, J. Boutin, and S. Mecklenburg (2010), The SMOS mission: New tool for monitoring key elements of the global water cycle, *Proc. IEEE*, 98(5), 666–687, doi:10.1109/JPROC.2010.2043032.

Kikuchi, K., and B. Wang (2008), Diurnal precipitation regimes in the global tropics, *J. Clim.*, 21(11), 2680–2696, doi:10.1175/2007JCLI2051.1.

Lagerloef, G., F. R. Colomb, D. Le Vine, F. Wentz, S. Yueh, C. Ruf, Y. Chao, A. deCharon, G. Feldman, and C. Swift (2008), The Aquarius/SAC-D mission: Designed to meet the salinity remote-sensing challenge, *Oceanography*, 21(1), 68–81, doi:10.5670/oceanog.2008.68.

Lukas, R., and E. Lindstrom (1991), The mixed layer of the western equatorial Pacific Ocean, *J. Geophys. Res.*, 96, 3343–3357, doi:10.1029/90JC01951.

Minnett, P. J. (2003), Radiometric measurements of the sea-surface skin temperature: The competing roles of the diurnal thermocline and the cool skin, *Int. J. Remote Sens.*, 24(24), 5033 5047, doi:10.1080/0143116031000095880.

Murphy, D., S. Riser, N. Larson, and C. Janzen (2008), Measurement of salinity and temperature profiles through the sea surface on Argo floats. 4th Aquarius/SAC-D Science Workshop, Puerto Madryn, Argentina.

Nesbitt, S. W., and E. J. Zipser (2003), The diurnal cycle of rainfall and convective intensity according to three years of TRMM measurements, *J. Clim.*, 16(10), 1456–1475, doi:10.1175/1520-0442-16.10.1456.

Oka, E. (2005), Long-term sensor drift found in recovered Argo profiling floats, *J. Oceanogr.*, 61(4), 775–781, doi:10.1007/s10872-005-0083-6.

Price, J. F. (1979), Observations of a rain-formed mixed layer, *J. Phys. Oceanogr.*, 9(3), 643 649, doi:10.1175/1520-0485(1979)009<0643:OOARFM>2.0.CO;2.

Reverdin, G., S. Morisset, J. Boutin, and N. Martin (2012), Rain-induced variability of near sea surface T and S from drifter data, *J. Geophys. Res.*, 117, C02032, doi:10.1029/2011JC007549.

Riser, S., L. Ren, and A. Wong (2008), Salinity in Argo: A modern view of a changing ocean, *Oceanography*, 21(1), 56–67, doi:10.5670/ oceanog.2008.67.

Ruddick, B. (1983), A practical indicator of the stability of the water column to double-diffusive activity, *Deep Sea Res., Part A*, 30(10), 1105–1107, doi:10.1016/0198-0149(83)90063-8.

Price, J. F. (1979). Observations of a rain-formed mixed layer. *J. Phys. Oceanogr.*, 9(3), 643-649. doi: 10.1175/1520-0485(1979)009<0643:OOARFM>2.0.CO;2

Saunders, P. M. (1967), The temperature at the ocean-air interface, *J. Atmos. Sci.*, 24(3), 269 273, doi:10.1175/1520-0469(1967)024<0269:TTATOA>2.0.CO;2.

Schanze, J. J., G. Lagerloef, R. W. Schmitt, and B. A. Hodges (2014), Snakes on a ship: Surface salinity observations during SPURS, Abstract 17211 presented at 2014 Ocean Science Meeting, Co-sponsored by ASLO, TOS, and AGU Honolulu, Hawaii, 23–28 Feb.

Soloviev, A., and R. Lukas (1997), Observation of large diurnal warming events in the near surface layer of the western equatorial Pacific warm pool, *Deep Sea Res., Part I*, 44(6), 1055 1076, doi:10.1016/S0967-0637(96)00124-0.

Soloviev, A., and R. Lukas (2006*), The Near-Surface Layer of the Ocean: Structure, Dynamics and Application*, vol. 31, 572 pp., Atmos. and Oceanogr. Sci. Lib., Springer, Dordrecht, Netherlands.

Wong, A., R. Keeley, T. Carval, and the Argo Data Management Team (2013), Argo quality control manual, version 2.9. Argo Data Management, 54 pp. [Available online at

http://www.argodatamgt.org/content/download/20685/142877/file/argo-quality-control manual_version2.9. pdf.]

Yang, S., and E. A. Smith (2006), Mechanisms for diurnal variability of global tropical rainfall observed from TRMM, *J. Clim.*, 19(20), 5190– 5226. doi:10.1175/JCLI3883.1.

Yang, S., and E. A. Smith (2008), Convective-stratiform precipitation variability at seasonal scale from 8 Yr of TRMM observations: Implications for multiple modes of diurnal variability, *J. Clim.*, 21(16), 4115–4131, doi:10.1175/2008JCLI2096.1.

Yu, L. (2010), On sea surface salinity skin effect induced by evaporation and implications for remote sensing of ocean salinity, *J. Phys. Oceanogr.,* 40(1), 85–102, doi:10.1175/2009JPO4168.1.

Table 2.1. STS float summary for floats used in this study

Table 2.1. STS Float Summary for Floats Used in this Study

UW ID	WMO ID	Deployment Date	Deployment Location	Classification	Fast Cycle	Number of Profiles
F5232	5902266	21 Mar 2010	09.97N, 68.04E	Indian	Y	247
F5233	5903744	1 Jan 2013	18.04N, 89.51E	Indian	Y	801
F6179	5902267	21 Mar 2010	08.95N, 67.99E	Indian	N	85
F6918	5903587	14 Dec 2011	17.00N, 69.42E	Indian	N	140
F6920	5903588	31 Aug 2011	09.94N, 88.52E	Indian	N	108
F6922	5903589	4 Sep 2011	15.22N, 89.70E	Indian	N	104
F6924	5903590	6 Sep 2011	17.39N, 89.00E	Indian	N	159
F7059	5903745	29 Dec 2012	12.09N, 88.70E	Indian	Y	665
F7086	5903746	29 Dec 2012	12.10N, 88.70E	Indian	Y	659
F7092	5903747	1 Jan 2013	18.03N, 89.52E	Indian	Y	587
F6882	5903281	30 Jun 2010	17.15N, −37.58E	Atlantic	Y	283
F6884	5903269	29 Apr 2010	04.99N, −22.97E	Atlantic	N	115
F6885	5903270	30 Apr 2010	08.06N, −23.02E	Atlantic	N	41
F6888	5903282	29 Jun 2010	15.07N, −35.35E	Atlantic	N	128
F6889	5903283	1 Jul 2010	18.98N, −39.51E	Atlantic	N	122
F6923	5904016	16 Sep 2012	25.26N, −37.76E	Atlantic	Y	228
F7547	5903999	15 Sep 2012	24.75N, −37.75E	Atlantic	N	30
F7569	5904011	17 Sep 2012	23.75N, −37.75E	Atlantic	Y	208
F7572	5904018	16 Sep 2012	25.25N, −38.27E	Atlantic	N	73
F7574	5903995	6 Oct 2012	29.97N, −33.32E	Atlantic	N	59
F7582	5903998	15 Sep 2012	24.76N, −38.25E	Atlantic	N	18
F7585	5903997	8 Sep 2012	36.72N, −58.92E	Atlantic	N	25
F7587	5904004	17 Sep 2012	24.75N, −37.25E	Atlantic	N	76
F7594	5903996	8 Sep 2012	36.37N, −58.28E	Atlantic	N	74
F7595	5903750	6 Oct 2012	29.01N, −35.51E	Atlantic	N	59
F7598	5904000	7 Oct 2012	31.00N, −31.21E	Atlantic	N	56
F7599	5903751	5 Oct 2012	27.00N, −36.94E	Atlantic	N	59
F7604	5904013	22 Sep 2012	25.32N, −37.08E	Atlantic	Y	631
F7607	5904005	17 Sep 2012	23.74N, −37.25E	Atlantic	N	44
F7611	5904001	11 Sep 2012	30.01N, −47.09E	Atlantic	N	74
F7635	5904012	17 Sep 2012	23.74N, −38.24E	Atlantic	N	76
F7660	5904009	16 Sep 2012	24.76N, −38.74E	Atlantic	N	73
F7699	5904003	17 Sep 2012	24.26N, −37.25E	Atlantic	N	76
F7742	5904010	18 Sep 2012	24.26N, −38.75E	Atlantic	Y	711
F5241	5902108	9 Sep 2008	02.05N, 164.95E	Pacific	N	208
F6862	5903402	20 Apr 2011	04.95N, −139.96E	Pacific	N	185
F6872	5901490	18 Oct 2010	47.49N, −126.36E	Pacific	N	232
F6874	5903403	21 Apr 2011	02.06N, −140.04E	Pacific	N	185
F6877	5903404	22 Apr 2011	−00.01S, −139.87E	Pacific	N	185
F6879	5903610	27 Oct 2011	45.03N, −130.44E	Pacific	N	148
F6915	5903383	23 Nov 2010	09.02N, −140.25E	Pacific	N	54
F6916	5903273	21 May 2010	22.69N, −157.99E	Pacific	N	240
F6917	5903384	11 Dec 2010	8.07N, −124.96E	Pacific	N	210
F6921	5903609	27 Oct 2011	44.01N, −131.15E	Pacific	N	150
F7578	5903732	11 Apr 2012	16.68N, −175.00E	Pacific	N	119
F5131	5901469	20 Dec 2007	22.82N, −157.94E	Pacific	Y	423
F6117	5902125	24 Mar 2009	01.99N, 150.22E	Pacific	Y	324
F6119	5902126	25 Mar 2009	04.01N, 149.01E	Pacific	N	48
F7106	5903748	12 Dec 2012	14.22N, 129.96E	Pacific	N	39
F7539	5903749	13 Dec 2012	15.01N, 129.98E	Pacific	N	39
F7548	5903733	14 Sep 2012	24.25N, −37.76E	Pacific	N	117
F7586	5903734	14 Apr 2012	14.03N, 170.00E	Pacific	N	116
F7589	5903735	16 Apr 2012	09.82N, 161.96E	Pacific	N	112
F7648	5904019	12 Dec 2012	11.94N, 129.95E	Pacific	N	73
F7650	5904020	12 Dec 2012	13.25N, 129.96E	Pacific	N	71
F6883	5903268	28 Apr 2010	01.77N, −23.00E	Atlantic	Y	262
F6887	5903271	26 Apr 2010	−05.16S, −23.15E	Atlantic	N	16
F6103	5902122	23 Mar 2009	−01.05S, 152.14E	Pacific	N	20
F6113	5902123	24 Mar 2009	−0.01S, 151.48E	Pacific	N	173
F5066	5901748	15 Mar 2008	−00.06S, −168.41E	Pacific	Y	203
F6115	5902124	24 Mar 2009	01.01N, 150.84E	Pacific	Y	249
F6177	5902127	25 Mar 2009	05.03N, 148.39E	Pacific	N	174

Table 2.2. Percentage of profiles where the difference between the surface and 4 m temperature and salinity is within each difference class

Table 2.2. Percentage of Profiles Where the Difference Between the Surface and 4 m Temperature and Salinity is Within Each Difference Class[a]

	−0.2 <=ΔT/S< −0.1	*−0.1 <= ΔT/S< 0*	*0 <= ΔT/S< 0.1*	*0 .1 <=ΔT/S< 0.2*	Number of Profiles
Temperature					
All Floats	1.30	58.13	28.75	3.12	11,233
Atlantic	1.03	50.74	33.44	3.75	3603
Pacific	1.10	61.68	28.21	2.78	4094
6117	2.16	50.31	22.84	5.86	324
Indian	1.81	61.57	24.60	2.86	3536
Salinity					
All Floats	1.49	50.13	47.15	0.04	11,233
Atlantic	1.41	39.63	55.14	0.33	3603
Pacific	1.34	38.88	55.87	0.15	4094
6117	2.47	35.49	53.70	0.31	324
Indian	2.06	39.58	52.99	0.40	3536

[a]Differences are calculated using data from the STS unit.

Figure 2.1. STS float endcap with both STS and SBE 41CP CTDs. Unlike the SBE 41CP, the STS unit is unpumped and does not carry a biocide.

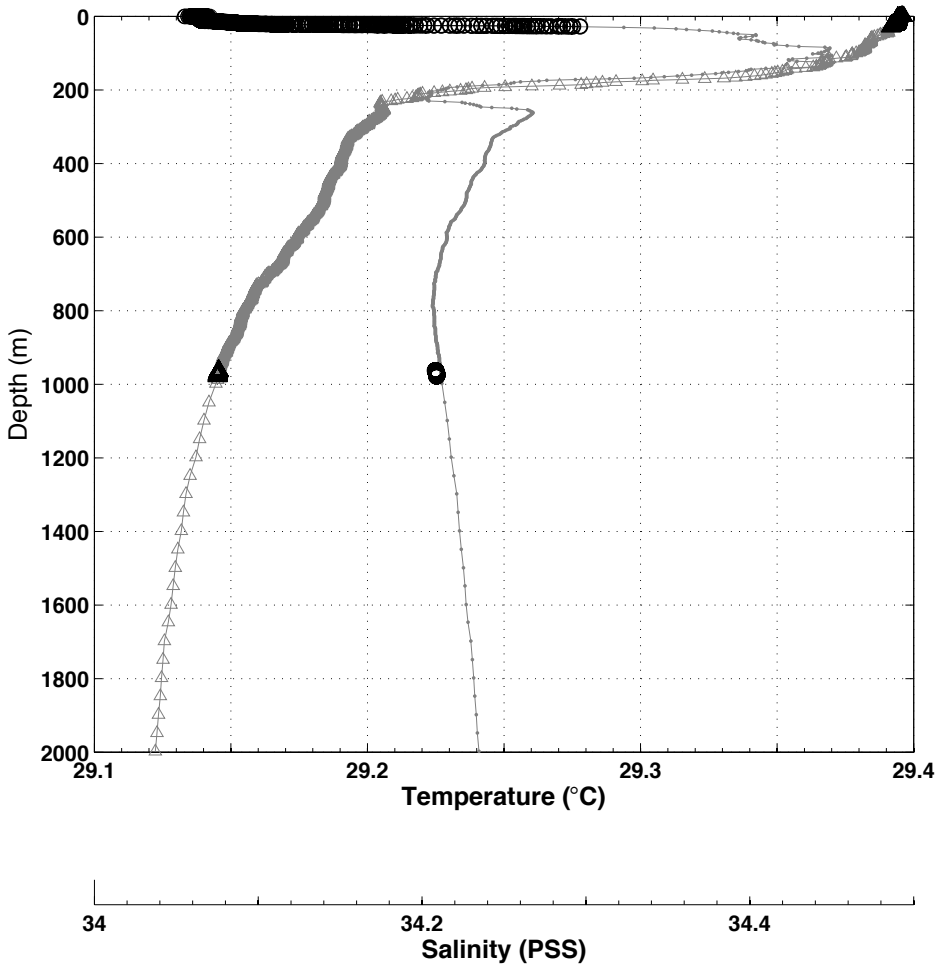

Figure 2.2. Example STS float profile collected by float 6117 near Papua New Guinea. The main SBE 41CP unit (gray) collects samples between 4 and 2000 m. The auxiliary STS unit operates briefly at a depth of 1000 m and again from 30 m to the surface. The temperature (circles) and salinity (triangles) differences between the two sensors for this profile (number 228) are less than 0.002°C and 0.01 PSU, respectively.

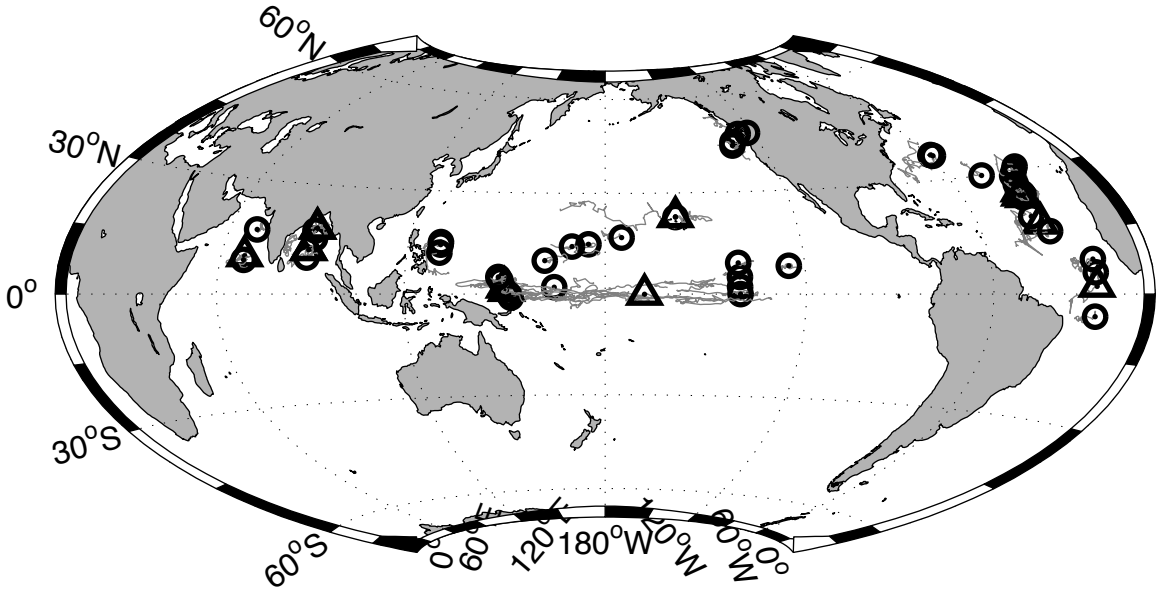

Figure 2.3. Deployment location (circles and triangles) and trajectories (gray lines) of 62 STS equipped floats deployed beginning in December 2007. Triangles indicate the deployment location of 15 floats that have completed a "fast cycle" profiling period and whose data are used in the diurnal cycle analysis.

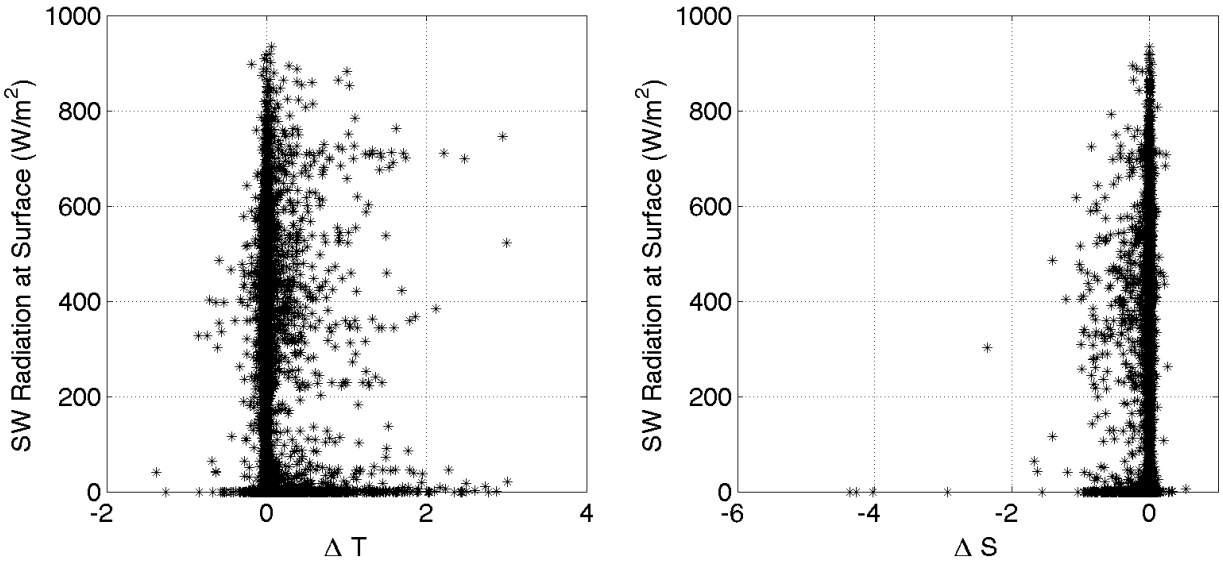

Figure 2.4. SST and SSS difference from 4 m versus shortwave radiation incident at the surface.

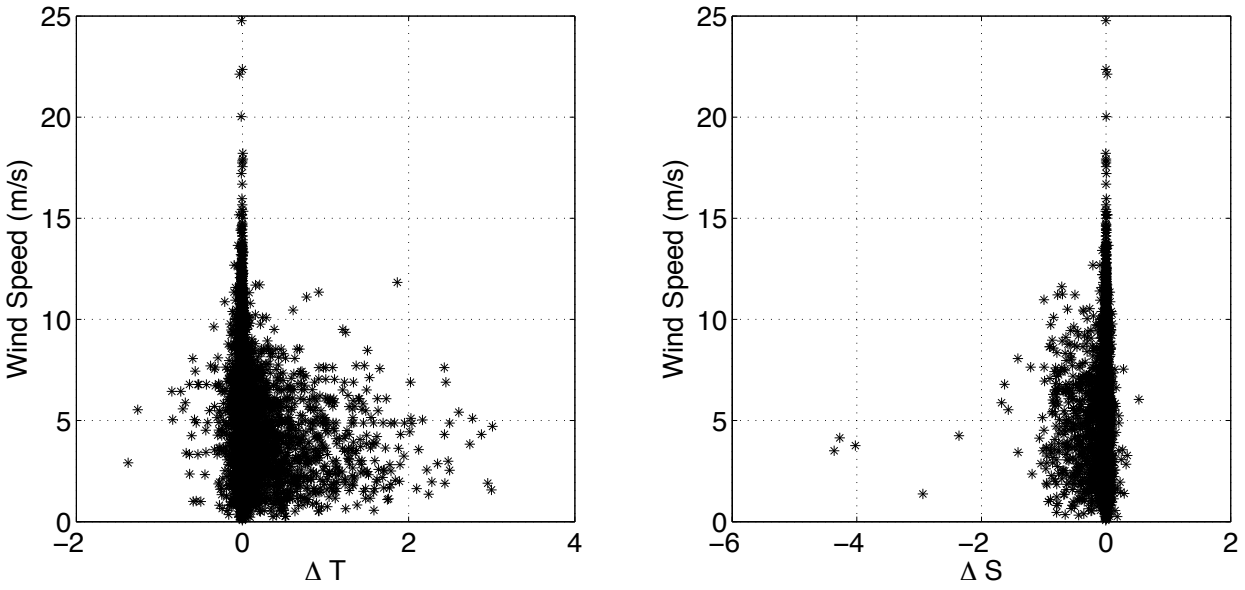

Figure 2.5. Difference from 4 m versus wind speed. Above wind speeds of ~6-10 m/s, the water column is well mixed.

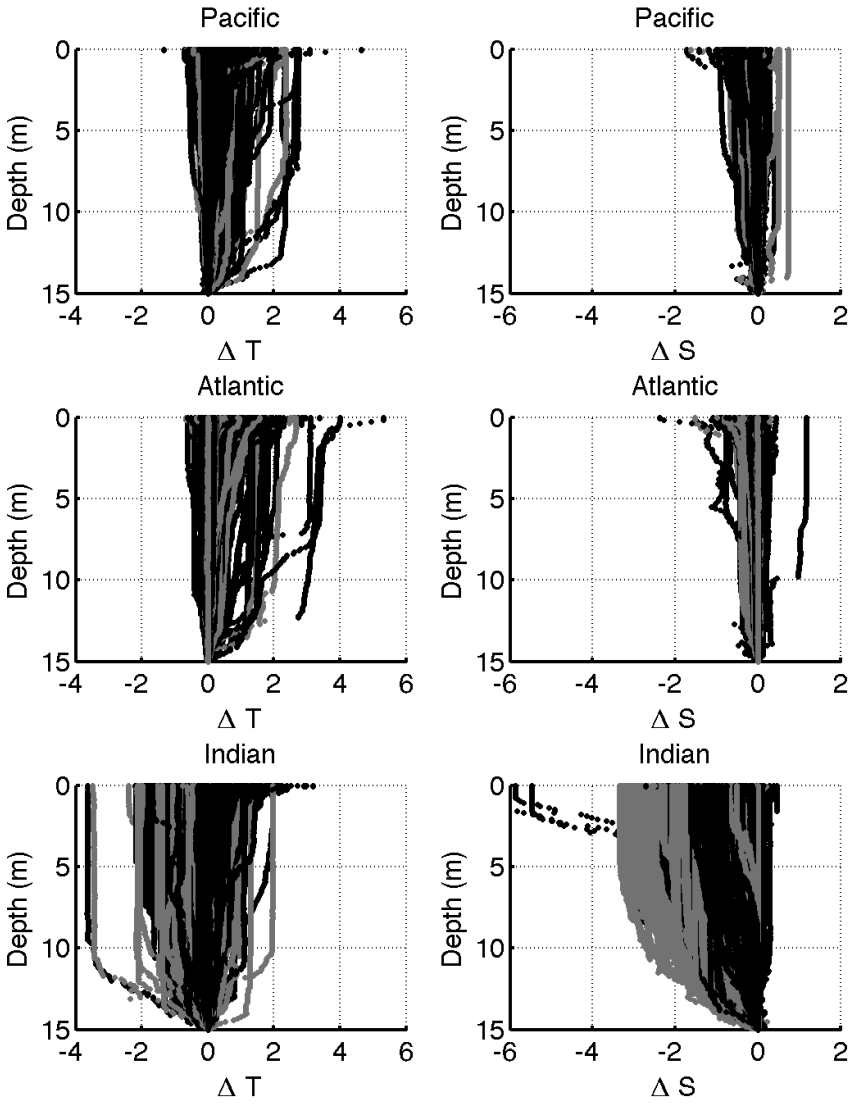

Figure 2.6. (left) Difference from 15 m for temperature and (right) salinity for floats deployed in the Pacific, Atlantic, and Indian Oceans. Differences collocated with wind speed less than 6 m/s are gray. Diurnal warming of over 4° is observed, with a rapid decay with depth. Occasional cooling associated with rainfall events is also observed. Freshening associated with rainfall events of up to –2 PSU is contained primarily to the upper 2 m. The slight positive bias in salinity is on the same order of magnitude of the STS accuracy and cannot be unequivocally attributed to evaporation.

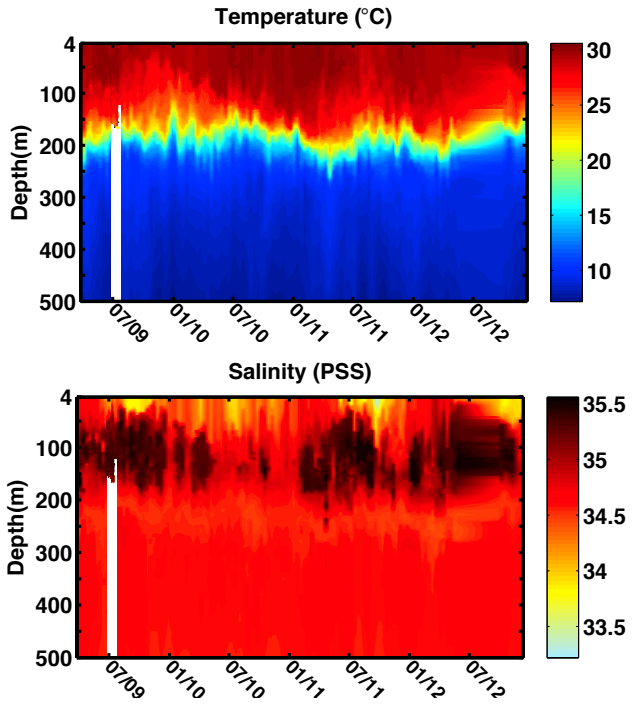

Figure 2.7. (top) Temperature and (bottom) salinity from the SBE 41CP unit from float 6117 deployed in the tropical western Pacific (1.99°N, 150.22°E). An annual cycle in temperature and salinity can be seen in the upper 50 m with the summer months of July and August being warmer and fresher. The white region is when the float was programmed to cycle in the upper 150 m every 2.5 h.

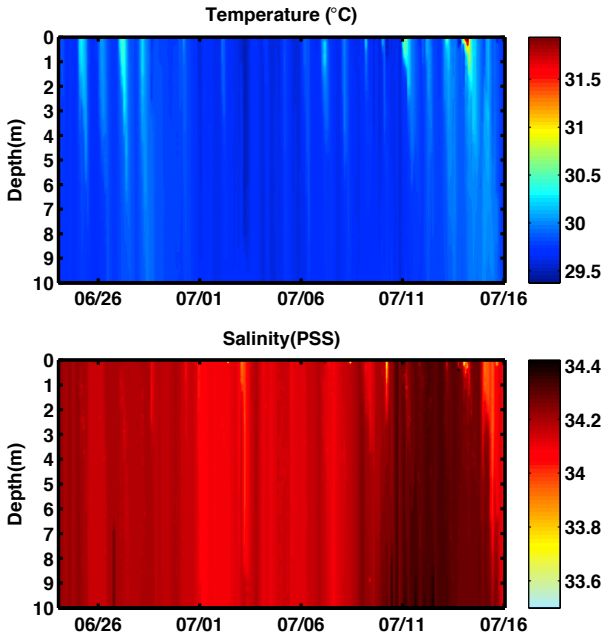

Figure 2.8. (top) Temperature and (bottom) salinity in the upper 10 m from the STS unit of float 6117 deployed in the tropical western Pacific (1.99°N, 150.22°E). From 24 June 2009 to 19 July 2009 the float was programmed to continuously profile in the upper 150 m every 2.5 h which corresponds with the blank region in Figure 2.7. The upper 10 m shows a clear diurnal cycle in temperature with salinity exhibiting a weaker diurnal response. The diurnal thermocline extends to approximately 2 m.

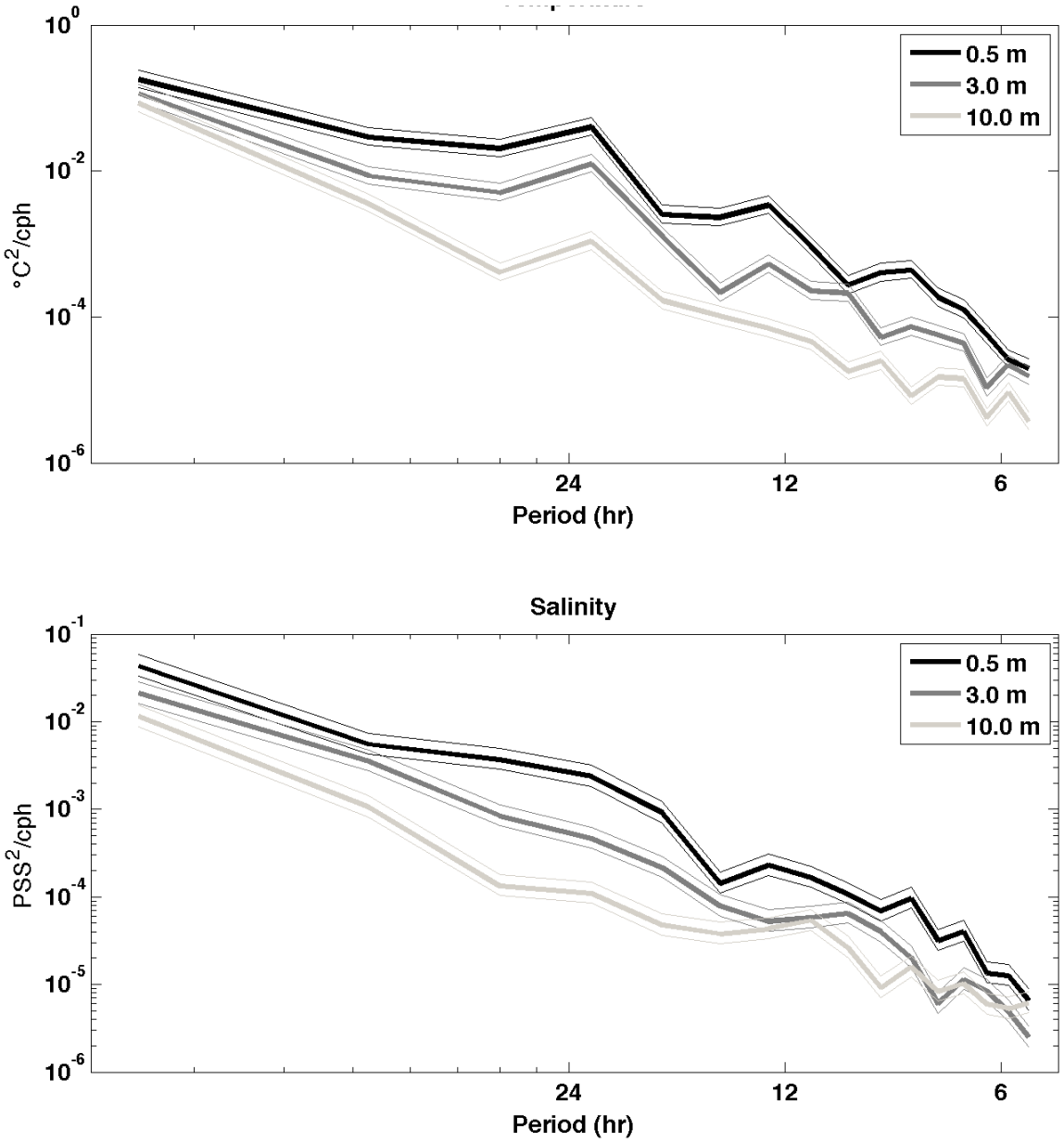

Figure 2.9. (top) Power spectrum for temperature and (bottom) salinity from float 6117 deployed in the tropical western Pacific (1.99°N, 150.22°E) for depths of 0.5, 3.0, and 10 m. Temperature shows a clear diurnal response through the upper 10 m, which decays with depth, while salinity exhibits a more broadband response contained to the surface.

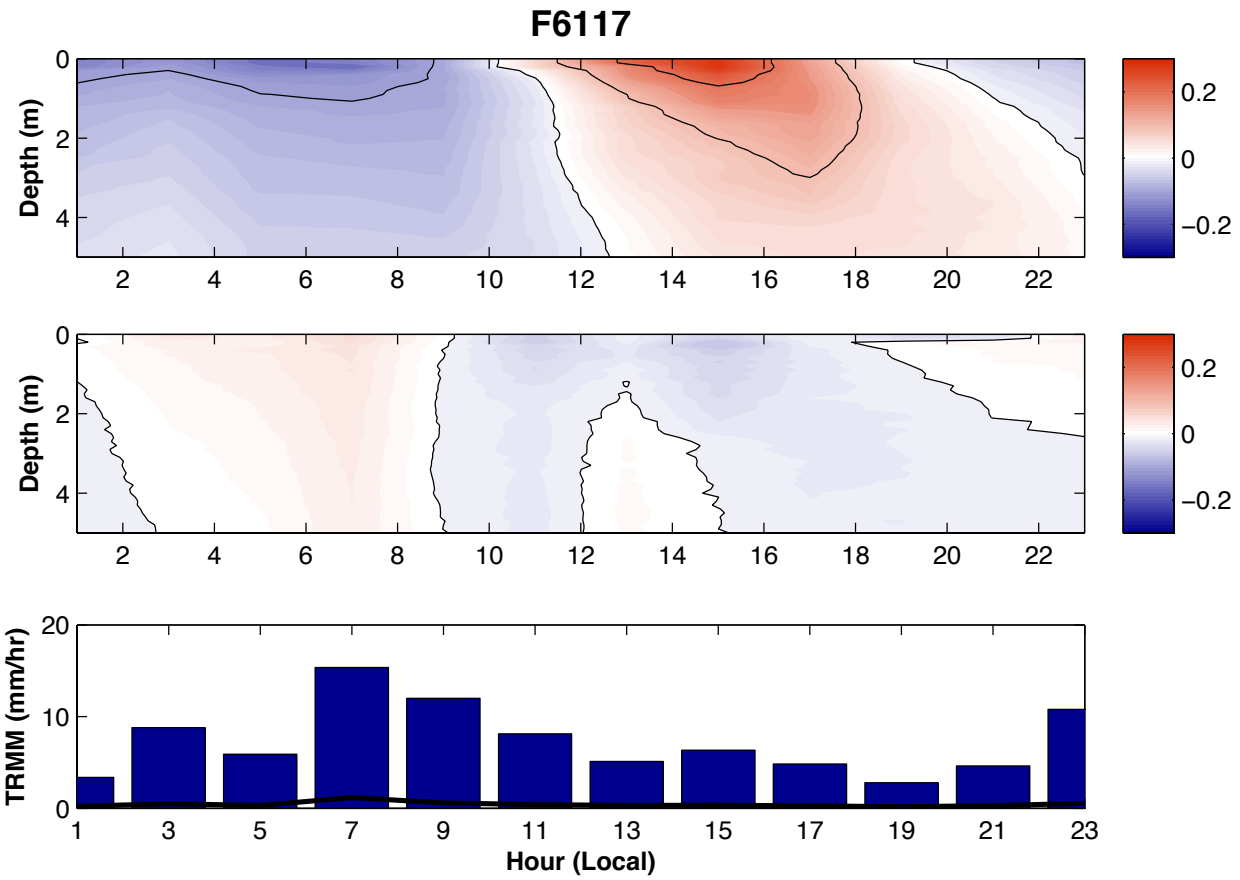

Figure 2.10. Two hourly binned composite diurnal temperature (top) and salinity (bottom) anomalies for float 6117 deployed in the tropical western Pacific (1.99°N, 150.22°E) during the float's fast cycle profiling schema. Diurnal warming due to insolation reaches its peak of 0.29 at the surface at 1500 local time. The magnitude of the diurnal cycle decreases with depth and is reduced to 0.07°C by 4 m. There is also a time lag with depth, with the peak at 4 m occurring at 1700. Salinity also exhibits a diurnal cycle, with maximum freshening of −0.07 PSU occurring at 1500. While composite rainfall reaches its peak at 0700 in the morning, mixing due to cooling moderates this freshening.

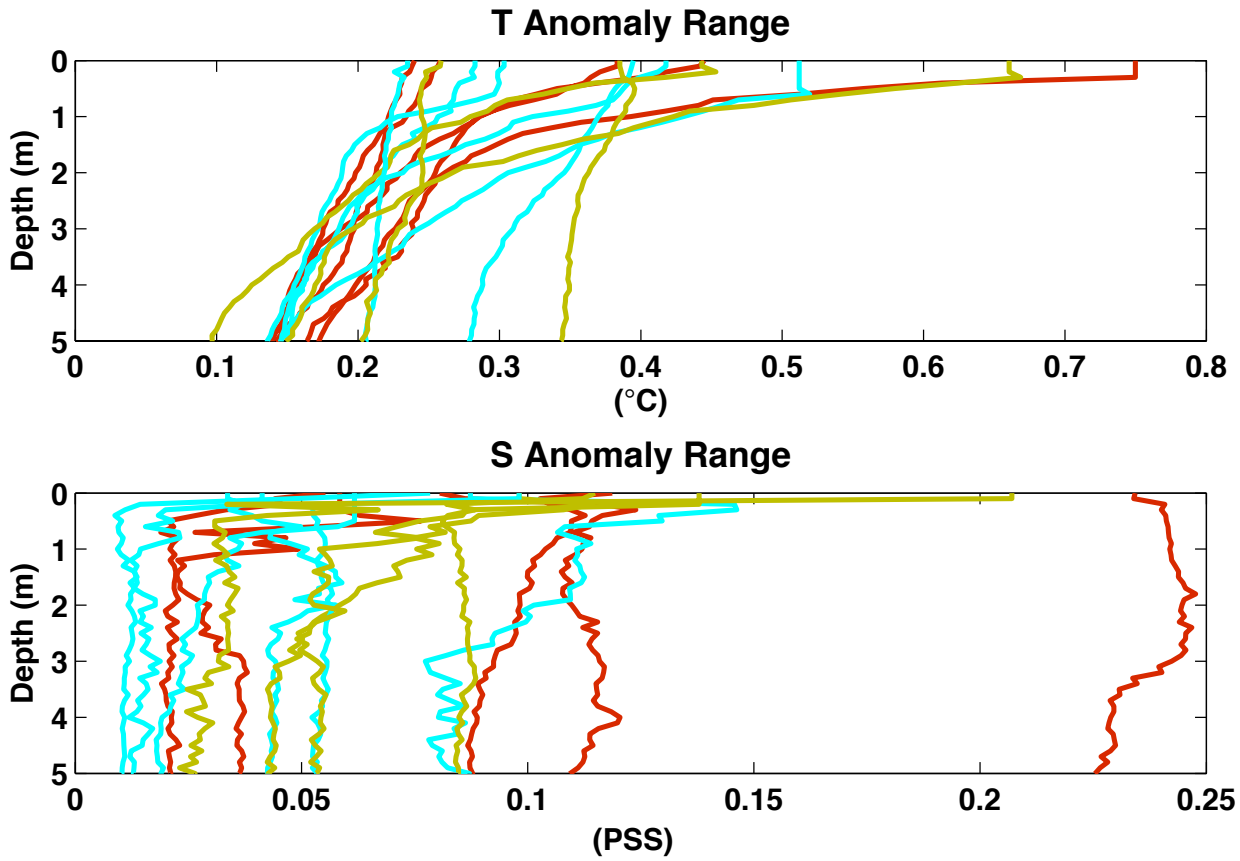

Figure 2.11. (top) Magnitude of the composite diurnal vertical profile for temperature and (bottom) salinity for all floats that have completed a fast cycle schema in the Atlantic (cyan), Pacific (yellow), and Indian (red) oceans. The magnitude decays with depth and is ~50% of its surface value at 5 m. Diurnal cycles with the largest amplitudes are found in the Pacific Ocean and Bay of Bengal where freshening due to rainfall and river runoff creates stable stratified layers which enhances the diurnal cycle in temperature near the surface.

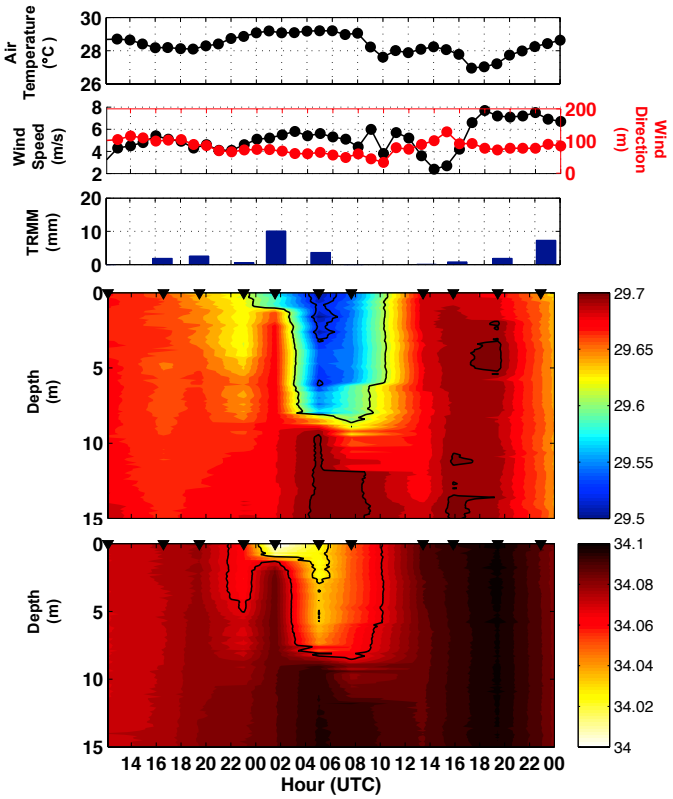

Figure 2.12. 3 July 2009 rainfall event observed by float 6117 deployed in the tropical western Pacific. Air temperature, wind speed, and wind direction from TAO mooring location located at 2°N, 147°E. Collocated, 3 h rainfall data from TRMM. Temperature and Salinity from the STS CTD.

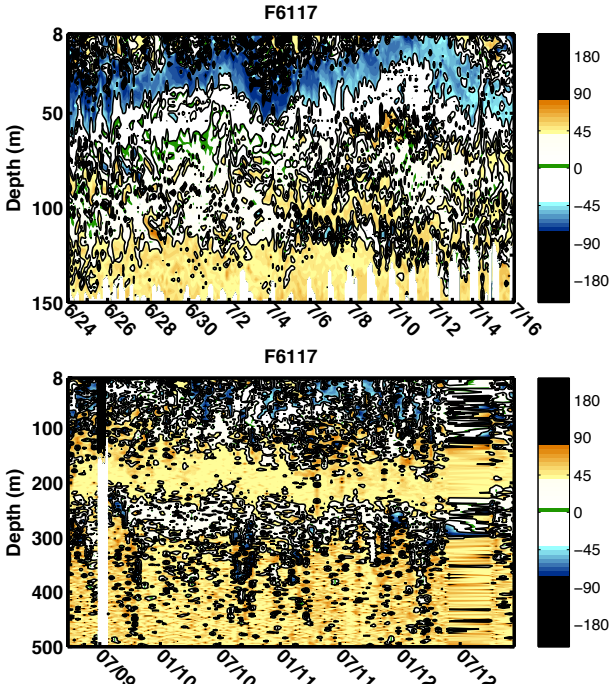

Figure 2.13. Turner Angle for float 6117 deployed in the tropical western Pacific. (top) During the fast cycle period and (bottom) over the entire record. Black regions indicate instability, while white and green colors indicate stability. Yellow colors are indicative of salt fingering while blue colors indicate diffusion.

Chapter 3

Upper Ocean Responses to Rainfall

Abstract

Precipitation falling over the ocean is one of the largest components of the freshwater cycle and also one of the most difficult to observe. Ocean near-surface stratification resulting from rain can influence air-sea feedbacks as well as influence validation of satellite measurements. In the present study, the upper ocean vertical structure, stability, and time evolution following rainfall events is examined using high vertical resolution measurements of temperature and salinity from Argo-type floats equipped with Surface Temperature and Salinity (STS) CTDs. Approximately 6% of profiles surveyed experienced freshening larger than -0.1 PSU. Mean freshening of drop events associated with rainfall is -0.37 PSU with a cooling of -0.13 °C. The observed fresh, cool upper ocean response was 3 m thick and had an average maximum freshening depth of 0.6 m. Decay of the fresh and cool signal away from the surface was 20% and 38% between the depths of 0.5 m and 3 m, respectively. Density at the depth of the salinity drop was observed to become either denser (when cooling controls) or lighter (when salinity controls) with an equal split between outcomes. Vertical structures associated with rainfall showed a potential for double diffusion, as indicated in Turner Angle calculations, in many profiles. Vertical mixing of the stratified water column occurred quickly (6-8 hours) in most cases and was associated with equivalent vertical diffusivities on the order of 10^{-4} m^2/s. Salinity drop magnitudes were linearly correlated with 6 hr rainfall accumulation for wind speeds > 6 m/s. No linear correlation between

wind speed and salinity drop magnitude was found. Covariance between wind and rain rate is expected to result in a nonlinear salinity drop response across a range of wind conditions.

3.1 Introduction

The input of freshwater to the ocean through precipitation is the second largest component of the global water cycle with ~78% of precipitation falling over the ocean (Durack, 2015; Schanze et al., 2010). Using salinity as a proxy, satellites (Kerr et al., 2010; Lagerloef et al., 2008) and the Argo array of profiling floats (Riser et al., 2008, 2016) have provided new insights into the larger-scale, integrated responses of the ocean to rainfall. Due to the often-small footprint and short lifespan of precipitation events however, the effects of individual precipitation events on upper ocean temperature and salinity have been difficult to observe. There remains a need to constrain the variability associated with these rain events. Near-surface stratification associated with rainfall events can modulate sea surface temperature (SST) diurnal cycles, amplifying thermal feedbacks to the atmosphere via heat trapping in the stable, fresh surface layer (S. P. Anderson et al., 1996; Clayson & Bogdanoff, 2013; Kawai & Wada, 2007; Soloviev & Lukas, 1997; Webster et al., 1996). Additionally, rain-induced stratification can influence validation of salinity satellites due to measurement depth differences (Boutin et al., 2013, 2015; Drucker & Riser, 2014). Recent work has sought to parameterize the rainfall response using satellite precipitation rates and wind speed for use in salinity satellite corrections (Santos-Garcia et al., 2014).

While studies have shown that the upper ocean is well mixed by wind most of the time (J. E. Anderson & Riser, 2014; Henocq et al., 2010), significant upper ocean stratification events have been observed (J. E. Anderson & Riser, 2014; Asher et al., 2014; Tomczak, 1995; Walesby et al., 2015). Direct observations of fresh lenses associated with rainfall are difficult to obtain though

development of unique ship-deployed (Asher et al., 2014; Walesby et al., 2015; Ward et al., 2014) and free drifting observational platforms (J. E. Anderson & Riser, 2014; Reverdin et al., 2012) have recently contributed to a new era of observation. These observations have found that fresh lenses are typically short-lived, spatially patchy, and have a salinity response that decreases with depth (J. E. Anderson & Riser, 2014; Asher et al., 2014; Reverdin et al., 2012). The largest salinity drop events have been observed under low winds and high rainfall conditions. Modeling studies have shown lateral spreading of the rain lenses (Soloviev & Dean, 2015). At the surface, turbulence can be enhanced by rain events and be trapped in the surface layer which leads to a suppression of turbulence below the lens (Drushka et al., 2016; Walesby et al., 2015; Zappa et al., 2009). Rain-induced upper ocean stratification may be conducive to double diffusion (Walesby et al., 2015). Diurnal cycles in upper ocean salinity have been observed where diurnal precipitation is present though the response is tempered by diurnal entrainment (J. E. Anderson & Riser, 2014; Cronin & McPhaden, 1999; Drushka et al., 2014; Fine et al., 2015). In the present study, we inventory the upper ocean response to rainfall using high vertical resolution near-surface observations collected with enhanced Argo-type profiling floats. Use of this drifting, high vertical resolution observational platform has resulted in an unprecedented number of observations of salinity drop events. The vertical structure, stability, and time evolution of these salinity drop events are examined under a variety of wind and rain conditions.

3.2 Data Description

3.2.1 *Temperature and salinity data*

Temperature and salinity profiles were collected with 76 surface temperature and salinity (STS) CTD (conductivity, temperature, depth) equipped Argo-type floats deployed in the Atlantic, Pacific, and Indian Oceans (Figure 3.1). Data collected between 20 December 2007 and 31

January 2016 are used in this study (limited by the availability of high resolution rainfall data). The majority of the 16,979 profiles collected during this time period were obtained while the floats operated on a standard Argo 10 day profiling mission (Riser et al., 2016). 23 floats were programed to complete fast profiling (~2.5 hours) for a portion of their lifetime resulting in 7,780 fast cycle profiles. Data from both the 10 day and 2.5 hour profiling schemes is used in this study All temperature and salinity profiles used in this study were obtained with a STS sensor manufactured by Seabird Electronics, Inc. (SBE). The unpumped STS CTD unit operates at 1.5 Hz between 30 m to 4 m, then at 1 Hz from a depth of 4 m to the sea surface. With an ascent rate of ~8 cm/s, the vertical resolution of data from the STS CTD is ~10 cm in the upper 30 m. The in situ accuracies of temperature and salinity are ~0.01°C and 0.02 PSU. Bubble contamination in near-surface STS data, identified as salinity spikes, was removed and the STS data were corrected for drift using concurrent data from the primary SBE 41CP CTD. Further details of the STS equipped float profile operation, data correction, and gridding can be found in Anderson and Riser (2014). To account for any potential conductivity cell thermal mass errors (CTM), freshening signals concurrent with warming larger than 0.05°C are excluded from this study. Development of a more detailed model for correction of CTM errors is underway.

3.2.2 *Rain and wind data*

Rainfall rates at float profile locations were obtained from the Climate Prediction Center morphing method (CMORPH) data product. Using infrared satellite images to estimate storm movement in between microwave satellite observations times, the CMORPH data product is able to provide higher spatiotemporal resolution precipitation data than other microwave only products. The global, 8 km (0.08°), 30 minute CMORPH V1.0 raw precipitation product was used in this study (Joyce et al., 2004). CMORPH data was linearly interpolated in space to the

float profile locations. At each profile location, a variety of rainfall statistics were calculated using 30 min rainfall rates for up to 3 days prior to the float profile. Wind estimates were determined using the European Centre for Medium-range Weather Forecasting (ECMWF) ERA-Interim reanalysis (Dee et al., 2011). ECMWF 10 m wind velocity vectors are available on a 0.25° grid every 6 hrs. The time and location closest to the float profile were used in the present study.

3.3 Methodology

3.3.1 *Identifying rain events*

Rain events were identified using a two-step process. First, STS Argo profiles collected during both normal (10 day) and fast cycle (~2.5 hour) profile periods were examined for salinity drops. Salinity drop events were identified using the criteria of Reverdin et al. (2012) that at some depth in the upper 10 meters a freshening of at least -0.1 PSU is observed. This was determined as the minimum of the difference between the salinity at 10 meters (S_{10m}) and every measurement depth from 9.9 m to the surface (S_x).

$$min(\Delta S = S_x - S_{10m}) \leq -0.1 \qquad (3.1)$$

This drop criterion is the same order of magnitude as the retrieval accuracy (target and validated) of satellite salinity averaged over spatial scales from 1° to 10° (Kerr et al., 2010; Lagerloef et al., 2008; Lee, 2016).

Second, rainfall was collocated to salinity drop profile locations. If no precipitation event occurred at the profile location within 24 hours prior to the profile time, it is assumed the drop is not due to rainfall. Drop events not concurrent with rainfall were removed from the analysis. It is assumed that the excluded salinity drop events are due to either river input (for floats in the Bay

of Bengal; see (Wilson & Riser, 2016)) or advection of low salinity water into the float profile location. It is expected that during active precipitation, maximum freshening occurs at the surface. Since the floats may profile after a rain event has ended and any resulting surface stratification has begun to evolve, we utilize drop events present anywhere in the upper 10 meters. The thickness of the fresh event was determined as the portion of the water column with a freshening of at least -0.1 PSU. Finally, multiple drop profiles from the same float within 8 hours of each other were assumed to be one event.

3.4 Results and Discussion

3.4.1 *Salinity drop event inventory*

Of the 16,979 profiles surveyed, salinity drops were identified in 981 profiles (~6% of all profiles) using the criteria detailed in section 3.2.1 (Figure 3.1). The majority of drop events (68%) are less than 0.5 PSU with most large events (> 1 PSU) found in the Bay of Bengal. In many cases, these drop events are not associated with rainfall and are likely a response to river input into the region. Since the response to rainfall is not straightforward in this case, all profiles collected in the Bay of Bengal are removed from further analysis even if they are concurrent with rainfall. In total, 369 profiles (~2% of all profiles) are associated with rainfall and located away from river influence (Table 1). 189 of these profiles were collected on 10 day cycles while 180 were collected during fast cycle missions. The majority of drop events (77%) associated with rainfall are also less than 0.5 PSU. The amplitude of the mean maximum freshening at any depth is -0.37 PSU.

The upper ocean structure, examined using the difference from 10 meters, shows that salinity drop events decay rapidly with depth and are primarily contained to the upper few meters of the water column (Figure 3.2). The depth of maximum freshening is generally shallower than 6 m

with an average value of 0.6 m (Figure 3.3) for all drop events. This is slightly deeper than the 0.2 m average minimum sampling depth of STS floats used in this study (after excluding bubble contaminated near-surface data). Larger salinity drop events (>1 PSU) have a slightly shallower mean depth of maximum freshening of 0.1 m. Larger events are only observed when the float profiled within an hour of rainfall (Figure 3.3). The shallower depth of maximum freshening for large, recently occurring events confirms the assumption that maximum freshening occurs at the surface under active precipitation. For all events, the average freshening decays by ~20% between 0.5 m and 3 m. The decay of the fresh signal with depth is more pronounced for larger (0.5 PSU and 1.0 PSU) events (34% and 82% reduction between the same depths). The average thicknesses of the observed fresh lenses are 3.1 m. This is thicker than the 1 m mixing depth assumed in the Rain Impact Model (RIM) currently used for Aquarius CAP V4.0 (Santos-Garcia et al., 2014) but similar to the mixing depth determined by fitting the same one dimensional diffusion model used in RIM to observations (Asher et al., 2014). Underestimating the mixing depth in the Rain Impact Model could result in an overestimate of the near-surface stratification due to rain by concentrating the freshwater input in a shallower layer. An overestimate of stratification in RIM could impact corrections made to Aquarius satellite data.

Salinity drop events are usually associated with a temperature drop due to the cooler temperature of the rainfall freshwater input. In situ measurements of rainfall temperature are close to surface air wet-bulb temperatures and are generally cooler than the sea surface temperature (~5° C cooler in the tropics) (S. P. Anderson et al., 1998). It is possible, though unlikely, for rainfall to be warmer than the SST (Katsaros & Buettner, 1969). Cooling from rain has been interpreted as an increase in the net heat flux out of the ocean during rainfall (Walesby et al., 2015). Following the rain event, stability gained from the freshwater input can lead to enhanced diurnal warming

signals. Our observations show that, in general, larger salinity drop events have larger cooling (Figure 3.3). The maximum salinity drop and the temperature drop are significantly correlated with a best-fit slope of -0.25 °C cooling per -1 PSU of salinity drop (R^2=0.23). The mean temperature drop at the depth of maximum freshening is -0.13°C. Cooling also decays away from the surface, but slightly less than salinity (Figure 3.2). The average temperature drop decays between at 0.5 m and 3 m by 38%.

The near-surface density structure shows both an increase in density (unstable) as well as a decrease in density (stable) (Figure 3.2). The water column is denser at the depth of maximum freshening than at 10 m in 59% of profiles. This proportion is seen across all combinations of wind speed, rain rate, salinity drop values, and elapsed time since rain. The densification of the near-surface due to cooling was also observed by *Asher et al* (2014). Our observations indicate that the cooling signal grows in proportion to the freshening, which may mean the resulting density profile depends primarily on a different process. Since we have excluded all events with warming at the depth of freshening, we are predisposed to observe densification, Only diurnal heating (preexisting or post rain event) or advection would be expected to warm the upper water column in the present study. At very high latitudes, not sampled here, it is possible that rainfall could be warmer than the ocean surface (Katsaros & Buettner, 1969). Excluding events with warming thus increases the likelihood of observing stability changes due only to rainfall. The interplay between the magnitude of freshening (stabilizes) and cooling effect due to rainfall (destabilizing) is nuanced and is examined in more detail in section 3.4.3.

3.4.2 *Correlation with wind and rainfall*

Of interest is how the impact of salinity drop events (freshening, cooling, and density) may be predicted for use in satellite validation and modeling of shorter-term variability in climate

models. As such, correlations between the precipitation rate, wind speed, and the magnitude of the salinity drop event in the upper ocean are desired. Previous studies have suggested the use of 3 day maximum rain rate (Henocq et al., 2010) or the 24 hour rain accumulation (Santos-Garcia et al., 2014) as appropriate rainfall statistical criteria. Here, we correlate 6 different rainfall statistics, determined with CMORPH 30 min resolution data, to the observed maximum freshening for each profile. The six rainfall statistics used include 3 rate-based (mm/hr) statistics; the maximum 3 day rain rate, the maximum 24 hr rain rate, the most recent rain rate prior to the float profile, and 3 accumulation (mm) statistics; the 3 day, 24 hr, and 6 hr rainfall accumulation before the float profile. Evaluation for correlation between salinity drops and these 6 rain statistics were completed for 3 wind speed classifications; all wind speeds combined, wind speeds < 6 m/s, and wind speeds > 6 m/s (Figure 3.4). The 6 hr rainfall accumulation for salinity drops with wind speeds > 6 m/s (30 events) was the only relationship, of the 18 evaluated, significant at the 95% level (Table 2). 6 hr rainfall accumulation was also significantly correlated with the size of the temperature drop (not shown) for wind speeds > 6 m/s. This is consistent with modeling studies which showed nonlinear responses at low wind speeds and linear responses at higher wind speeds (Drushka et al., 2016). Since many drop events were sampled more than 6 hours after the last rainfall (Figure 3.3) it is possible that our study does not well represent the instantaneous rainfall response and that for observational platforms which sample the ocean while it is raining, such as those used by (Asher et al., 2014), the instantaneous rain rate would be the most highly correlated. It is interesting however that an accumulation statistic has the highest correlation as it implies a memory of the near-surface ocean of up to 6 hours.

Correlation between the collocated wind speed at the time of float profiles and the maximum salinity drop is shown in Figure 3.3. A significant linear correlation was not found across all

wind speeds, wind speeds > 6 m/s, or wind speeds < 6 m/s. At low wind speeds the slope of the best fit is 0.13 m/s per PSU while above it was 0.64 m/s per PSU. While not significant, the general trend can be interpreted that at low wind speeds, a large range of salinity responses are found and the response is dominated by rainfall rates. Higher wind speeds reduce the likelihood of large salinity responses as the rain input is more rapidly mixed. This interpretation agrees with the results of Drushka et al. (2016), who observed a similar pattern with mooring data in the North Atlantic as well as in modeled upper ocean rainfall responses. In particular, the model results show a nonlinear response below 6 m/s and a linear response above 6 m/s but with a variable slope depending on rain rate.

The lack of linear correlation between salinity drops and wind or rain in this study illustrate that while a multivariate linear regression may show a linear response, it does not mean that the underlying process are linear. It could be an artifact of nonzero covariance between the variables. In order to assume a linear multivariate response, it must be assumed wind speed and rain rate are not correlated with each other. This is not a valid assumption as higher wind speeds are correlated with higher precipitation rates in deep convective systems (Back & Bretherton, 2005) as well as shallow convective systems (Nuijens et al., 2009). Correlation between wind and rain rate mean that the assumption of additivity for a linear relationship is not met. Linear correlations between salinity drop and precipitation found by previous studies (Boutin et al., 2014; Drucker & Riser, 2014; Drushka et al., 2016; Santos-Garcia et al., 2014, 2016) across a range of wind speeds should be used with caution. Nonlinear models, such as the power model proposed by Drushka et al. (2016), better reflect the underlying processes. The majority of rain events sampled in the present study are associated with winds < 6 m/s and accumulations less than 20

mm. Other wind speed and rain combinations are not sampled well enough to develop a statistical model in the present study.

3.4.3 *Temporal Evolution*

Due to limited observations, the persistence of rain-induced salinity drops is not adequately constrained. Previous studies have observed salinity drop events that evolve rapidly, often mixing into the upper ocean in a manner of hours (J. E. Anderson & Riser, 2014; Price, 1979; Wijesekera et al., 1999), as well as longer persisting events (Walesby et al., 2015). Modeling studies have shown that higher winds and lower rain rates are associated with shorter-lived lenses (Drushka et al., 2016). Looking at the time elapsed between the profile time and last rainfall recorded at the profile location; we can investigate the general duration of salinity drop events (Figure 3.3). With one exception, salinity drop events larger than 1 PSU are only observed if the float profiled within 1 hour of the cessation of a rainfall event. For events between 0.1 and 1 PSU, there is large variability in event duration, with some events persisting up to 22.5 hours after the rainfall ended. This could also represent advection of freshwater into the float profile location from a location with more recent rain. The largest 24 hr maximum rain rates are associated with profiles collected within 5 hours of rainfall (not shown) while more moderate rain events are associated with longer lasting events. Large rain events have two destabilizing processes, higher winds (Back & Bretherton, 2005) and more cool freshwater input, both of which lead to mixing.

Using data collected by floats on fast cycle (~2.5 hour between profiles) we can examine the time evolution of drop events in more detail. We assume that the Lagrangian float is profiling the same water column as it evolves in time. This assumption is necessary for this observational platform and implies that if the fresh lens is advected, the float is advected at the same rate. The

average distance traveled between events examined here is 8.8 km (0.80-61.19 km) with an average speed of 1 m/s. These values are heavily influenced by 18 events collected by floats located in the Atlantic and Pacific Northern Equatorial currents where distance traveled between profiles is 20-60 km. Most events do not have significant movement between profiles. Movement of 2 km at 0.25 m/s is more common. A total of 180 profiles collected during fast cycle profile missions contain salinity drops. Separating into ensembles of profiles at least 8 hours apart, we identified 86 independent rain events observed by 15 different floats.

An example of one of these rain events, observed by float 6115 on 7 July 2009 in the tropical western Pacific (1.45°S,159.36°W), is shown in Figure 3.5. Concurrent with a rain rate of 6 mm/hr, salinity is observed to drop 0.15 PSU while the upper ocean temperature cools. The fresh, cool signal penetrates to 4 meters depth with a weaker, time lagged with depth response. Within 8 hours the water column is again well mixed. The equivalent vertical diffusivity (k_z) of the rainfall event can be estimated as the change in the mean salinity in the lens (3 m) between the drop profile and the following profile divided by the second order center difference of dS/dz in the layer. The diffusivity for the 7 July 2009 event is, $k_z = 6.6 \times 10^{-4}$ m^2/s. This value is the same order of magnitude as diffusivities obtained by Asher et al. (2014).

Interestingly, the density of the water column shows relatively little response to the rainfall event with temperature and salinity changes being nearly density compensating. The stability of the rain event is examined using the Turner angle, defined as:

$$Tu(deg) = \tan^{-1}\left(\alpha\frac{\partial\theta}{\partial z} - \beta\frac{\partial S}{\partial z}, \alpha\frac{\partial\theta}{\partial z} + \beta\frac{\partial S}{\partial z}\right) \qquad (3.2)$$

where α is the coefficient of thermal expansion and β is the coefficient of saline contraction, z is depth, and θ and S are the temperature and salinity. Turner angles between -90° and -45° are prone to double diffusion, -45° and 45° are stable, and 45° and 90° prone to salt fingering.

Outside of these ranges the water column is stable. The event on 7 July 2009 shows instability in the near-surface layer and the water column is prone to double diffusion below the fresh lens. Double diffusive conditions below fresh lenses were also observed by Walesby et al. (2015). Since turbulence is suppressed below the surface layer, double diffusion may have the chance to occur. Using the heat and salt diffusion rates of St. Laurent and Schmitt (1999) it would take approximately 1-1.5 hrs to diffuse properties at the bottom of the fresh lens 1 m. Since the density of the two water masses are similar in this case, if double diffusive mixing has enough time to occur, it is possible that cabbeling could occur at the lower interface of rain lenses, resulting in a densification and further instability mixing. Density compensating layers were only observed in a few of the rain events in the present study while conditions preferable for double diffusion were ubiquitous for events profiled soon after the rain ended.

The average time evolution of all 86 drop events is shown in Figure 3.6. The rain-induced salinity and temperature response were determined by subtracting the non-rain profile collected prior to each drop event, then averaging events starting at the normalized salinity drop time. While each event is unique, by averaging all events we can get an understanding of the dominant responses. Since we have excluded freshening concurrent with warming, events that were averaged occurred primarily in the evening, overnight, and morning. The time period between 1300 and 1800 local time is not well represented. In the average event, we again see a salinity response (~0.1 PSU) contained primarily to the upper 1 meter that has an expression at 4 meters within 2 hours. Temperature also cools slightly (0.025 °C) and has an expression at 4 meters within 2 hours. 2 hours following the event, the maximum salinity response and temperature response begin to degrade. While the signal continues to reach further into the water column, it is continually reduced in strength. Within 6-8 hours the weak subsurface remnant is small

compared to surface warming and salinification likely due to the diurnal cycle. The cooling associated with the composite freshening is the proportional to the linear best fit to the individual observations (Section 3.4.1). A mixing depth of 3 m is also reflected in the composite with the majority of freshening contained to this depth throughout the 10 hour evolution. A mixing depth of 3 m was again utilized in determining an equivalent vertical diffusivity for the composite event. The vertical diffusivity ($k_z = 6.6 \times 10^{-4}$ m^2/s) is also similar to values obtained by Asher et al. (2014).

3.5 Summary and Conclusions

High resolution, near-surface measurements of temperature and salinity have allowed observation of the upper ocean responses to rainfall. These observations, obtained with STS equipped Argo-type floats, provide new insights. While the upper ocean is well mixed the majority of the time, significant salinity drop events correlated with rainfall are observed. The magnitude of these events is usually smaller than -0.5 PSU (mean -0.37 PSU) with the largest salinity stratification observed in the Bay of Bengal (likely the combined effect of river runoff and rain and not investigated here) and the tropics. Largest responses are observed when winds are light (< 6 m/s). Consistent across a wind range of wind speed and rain rates, the thickness of the fresh layer (reflective of the characteristic mixing depth) is ~3 m. One-dimensional diffusion models using a shallower mixing depth of 1 m to predict upper ocean stratification due to rain may overestimate maximum freshening. Maximum freshening is contained to the upper 1 m of the ocean and decays rapidly with depth, with a large reduction in observed freshening by 3 m. The amount the salinity drop signal decays away from the surface increases with the size of the events. Events larger than -0.1, -0.5, and -1.0 PSU decay by 20%, 34%, 82%, respectively, at 3 m. Temperature decays slightly more for each class of events (38%, 53%, 83%). This may be a

result of different diffusion rates for salt and heat (St. Laurent & Schmitt, 1999). Equivalent diffusivities are on the order of 10^{-4} m^2/s. Upper ocean cooling associated with rain is on the order of -0.25 °C/PSU. Rainfall can have both stabilizing (freshening) and destabilizing (cooling) effects on the upper ocean with a roughly equal split in the observed response. It appears that in the absence of diurnal warming, these processes are well balanced and scale with each other. The time evolution of stratification after rainfall thus likely depends on the stratification conditions already present in the water column or those which form shortly after the rain ends. Accurately modeling and predicting when each of these processes dominate will be important to understanding the persistence and broader scale influence of rainfall events.

Salinity drop events were significantly correlated to 6 hr rain accumulation for winds > 6 m/s. Significant correlations were not found for winds < 6 m/s or with alternative precipitation statistics. This may be a result of floats profiling after the cessation of the rain event or advection of freshwater into the profile location. A significant correlation with wind was not found though observations do indicate salinity stratification decays faster under high winds. Lower winds and longer persistence are associated with a broader range of salinity responses. It is not unexpected that a linear correlation between maximum salinity stratification and wind or rain was not robust. A linear response with rain rate is only expected to reflect physical processes if it is fitted to a narrow range of wind speeds. This is due to the correlation between wind speed and rain rate. While the salinity response to one of these variables may be linear (as observed with rainfall in previous studies), the combined effect of another variable on salinity may be nonlinear especially if the two controlling variables are correlated. Future work should investigate the nature of the nonlinear responses observed.

Future validation of theoretical rain stratification models will require observations of the full range of meteorological and oceanic conditions concurrent with rainfall. These variables should be observed on the scale at which rainfall occurs to reduce ambiguity regarding time evolution and spatial variability. Results from the coordinated SPURS-2 (fresh) field campaign will likely succeed in collecting these observations. Future work should develop a robust model capable of utilizing standard satellite and in situ observations so that the global, integrated effect of rain events can be quantified. While operational observation platforms integrate over large areas or are point measurements, utilization of advanced statistical techniques and datasets with recent advances (higher spatiotemporal resolution rainfall products, satellite salinity, Argo observations closer to the sea surface) could result in a statistical model capable of quantifying the rain ocean-atmosphere feedback.

Acknowledgments:

The floats used in this study were fabricated at the University of Washington by the skilled UW float group of Dana Swift, Dale Ripley, Rick Rupan, and Greg Brusseau. An additional thank you to Annie Wong and Robert Drucker for insightful conversations on STS data processing**.** Data used in this study were obtained from the following locations: STS Argo (http://runt.ocean.washington.edu/), CMORPH (ftp://ftp.cpc.ncep.noaa.gov/precip/CMORPH_V1.0/RAW/8km-30min/), ECMWF (http://apps.ecmwf.int/datasets/data/interim-full-daily/levtype=sfc/). Support for this work was generously supported through the following grants to the University of Washington, NASA grants NNX09AU71G, NNX11AF79G, and NNX15AG97G and Office of Naval Research grant N00014-15-1-2254, as well as NOAA support of US Argo.

References

Anderson, J. E., & Riser, S. C. (2014). Near-surface variability of temperature and salinity in the near-tropical ocean: Observations from profiling floats. *Journal of Geophysical Research: Oceans*, *119*(11), 7433–7448. https://doi.org/10.1002/2014JC010112

Anderson, S. P., Weller, R. A., & Lukas, R. B. (1996). Surface Buoyancy Forcing and the Mixed Layer of the Western Pacific Warm Pool: Observations and 1D Model Results. *Journal of Climate*, *9*(12), 3056–3085.

Anderson, S. P., Hinton, A., & Weller, R. A. (1998). Moored observations of precipitation temperature. *Journal of Atmospheric and Oceanic Technology*, *15*(4), 979–986.

Asher, W. E., Jessup, A. T., Branch, R., & Clark, D. (2014). Observations of rain-induced near-surface salinity anomalies. *Journal of Geophysical Research: Oceans*, n/a-n/a. https://doi.org/10.1002/2014JC009954

Back, L. E., & Bretherton, C. S. (2005). The Relationship between Wind Speed and Precipitation in the Pacific ITCZ. *Journal of Climate*, *18*(20), 4317–4328. https://doi.org/10.1175/JCLI3519.1

Boutin, J., Martin, N., Reverdin, G., Yin, X., & Gaillard, F. (2013). Sea surface freshening inferred from SMOS and ARGO salinity: Impact of rain. *Ocean Science*, *9*(1), 183.

Boutin, J., Martin, N., Reverdin, G., Morisset, S., Yin, X., Centurioni, L., & Reul, N. (2014). Sea surface salinity under rain cells: SMOS satellite and in situ drifters observations. *Journal of Geophysical Research: Oceans*, *119*(8), 5533–5545. https://doi.org/10.1002/2014JC010070

Boutin, J., Chao, Y., Asher, W. E., Delcroix, T., Drucker, R., Drushka, K., … Ward, B. (2015). Satellite and In Situ Salinity : Understanding Near-Surface Stratification and Sub-footprint

Variability. *Bulletin of the American Meteorological Society*. https://doi.org/10.1175/BAMS-D-15-00032.1

Clayson, C. A., & Bogdanoff, A. S. (2013). The Effect of Diurnal Sea Surface Temperature Warming on Climatological Air–Sea Fluxes. *Journal of Climate*, *26*(8), 2546–2556. https://doi.org/10.1175/JCLI-D-12-00062.1

Cronin, M. F., & McPhaden, M. J. (1999). Diurnal cycle of rainfall and surface salinity in the western Pacific warm pool. *Geophysical Research Letters*, *26*(23), 3465–3468.

Dee, D. P., Uppala, S. M., Simmons, A. J., Berrisford, P., Poli, P., Kobayashi, S., … Vitart, F. (2011). The ERA-Interim reanalysis: configuration and performance of the data assimilation system. *Quarterly Journal of the Royal Meteorological Society*, *137*(656), 553–597. https://doi.org/10.1002/qj.828

Drucker, R., & Riser, S. C. (2014). Validation of Aquarius sea surface salinity with Argo: Analysis of error due to depth of measurement and vertical salinity stratification. *Journal of Geophysical Research: Oceans*, n/a-n/a. https://doi.org/10.1002/2014JC010045

Drushka, K., Gille, S. T., & Sprintall, J. (2014). The diurnal salinity cycle in the tropics. *Journal of Geophysical Research: Oceans*, *119*(9), 5874–5890. https://doi.org/10.1002/2014JC009924

Drushka, K., Asher, W. E., Ward, B., & Walesby, K. (2016). Understanding the formation and evolution of rain-formed fresh lenses at the ocean surface. *Journal of Geophysical Research: Oceans*, n/a-n/a. https://doi.org/10.1002/2015JC011527

Durack, P. (2015). Ocean Salinity and the Global Water Cycle. *Oceanography*, *28*(1), 20–31. https://doi.org/10.5670/oceanog.2015.03

Fine, E. C., Bryan, F. O., Large, W. G., & Bailey, D. A. (2015). An initial estimate of the global distribution of diurnal variation in sea surface salinity. *Journal of Geophysical Research: Oceans*, n/a-n/a. https://doi.org/10.1002/2014JC010483

Henocq, C., Boutin, J., Reverdin, G., Petitcolin, F., Arnault, S., & Lattes, P. (2010). Vertical variability of near-surface salinity in the tropics: Consequences for L-band radiometer calibration and validation. *Journal of Atmospheric and Oceanic Technology*, *27*(1), 192–209.

Joyce, R. J., Janowiak, J. E., Arkin, P. A., & Xie, P. (2004). CMORPH: A Method that Produces Global Precipitation Estimates from Passive Microwave and Infrared Data at High Spatial and Temporal Resolution. *Journal of Hydrometeorology*, *5*(3), 487–503.

Katsaros, K., & Buettner, K. J. K. (1969). Influence of Rainfall on Temperature and Salinity of the Ocean Surface. *Journal of Applied Meteorology*, *8*(1), 15–18. https://doi.org/10.1175/1520-0450(1969)008<0015:IOROTA>2.0.CO;2

Kawai, Y., & Wada, A. (2007). Diurnal sea surface temperature variation and its impact on the atmosphere and ocean: A review. *Journal of Oceanography*, *63*(5), 721–744. https://doi.org/10.1007/s10872-007-0063-0

Kerr, Y. H., Waldteufel, P., Wigneron, J. P., Delwart, S., Cabot, F., Boutin, J., … Mecklenburg, S. (2010). The SMOS Mission: New Tool for Monitoring Key Elements ofthe Global Water Cycle. *Proceedings of the IEEE*, *98*(5), 666–687. https://doi.org/10.1109/JPROC.2010.2043032

Lagerloef, G., Colomb, F. R., Le Vine, D., Wentz, F., Yueh, S., Ruf, C., … others. (2008). The Aquarius/SAC-D mission: Designed to meet the salinity remote-sensing challenge. *Oceanography*, *21*(1), 68–81.

Lee, T. (2016). Consistency of Aquarius sea surface salinity with Argo products on various spatial and temporal scales. *Geophysical Research Letters*, *43*(8), 2016GL068822. https://doi.org/10.1002/2016GL068822

Nuijens, L., Stevens, B., & Siebesma, A. P. (2009). The Environment of Precipitating Shallow Cumulus Convection. *Journal of the Atmospheric Sciences*, *66*(7), 1962–1979. https://doi.org/10.1175/2008JAS2841.1

Price, J. F. (1979). Observations of a Rain-Formed Mixed Layer. *Journal of Physical Oceanography*, *9*(3), 643–649.

Reverdin, G., Morisset, S., Boutin, J., & Martin, N. (2012). Rain-induced variability of near sea-surface T and S from drifter data. *Journal of Geophysical Research: Oceans*, *117*(C2), n/a–n/a. https://doi.org/10.1029/2011JC007549

Riser, S. C., Freeland, H. J., Roemmich, D., Wijffels, S., Troisi, A., Belbéoch, M., … Jayne, S. R. (2016). Fifteen years of ocean observations with the global Argo array. *Nature Climate Change*, *6*(2), 145–153. https://doi.org/10.1038/nclimate2872

Riser, S. C., Ren, L., & Wong, A. (2008). Salinity in Argo: A modern view of a changing ocean. *Oceanography*, *21*(1), 56–67.

Santos-Garcia, A., Jacob, M. M., & Jones, W. L. (2016). SMOS Near-Surface Salinity Stratification Under Rainy Conditions. *IEEE Journal of Selected Topics in Applied Earth Observations and Remote Sensing*, *9*(6), 2493–2499. https://doi.org/10.1109/JSTARS.2016.2527038

Santos-Garcia, A., Jacob, M. M., Jones, W. L., Asher, W. E., Hejazin, Y., Ebrahimi, H., & Rabolli, M. (2014). Investigation of rain effects on Aquarius Sea Surface Salinity

measurements. *Journal of Geophysical Research: Oceans*, *119*(11), 7605–7624. https://doi.org/10.1002/2014JC010137

Schanze, J. J., Schmitt, R. W., & Yu, L. L. (2010). The global oceanic freshwater cycle: A state-of-the-art quantification. *Journal of Marine Research*, *68*(3–1), 569–595. https://doi.org/10.1357/002224010794657164

Soloviev, A., & Dean, C. (2015). 3D Dynamics of Freshwater Lenses in the Near-Surface Layer of the Tropical Ocean. *Oceanography*, 142–149. https://doi.org/10.5670/oceanog.2015.14.

Soloviev, A., & Lukas, R. (1997). Observation of large diurnal warming events in the near-surface layer of the western equatorial Pacific warm pool. *Deep Sea Research Part I: Oceanographic Research Papers*, *44*(6), 1055–1076. https://doi.org/10.1016/S0967-0637(96)00124-0

St. Laurent, L., & Schmitt, R. W. (1999). The Contribution of Salt Fingers to Vertical Mixing in the North Atlantic Tracer Release Experiment. *Journal of Physical Oceanography*, *29*(7), 1404–1424. https://doi.org/10.1175/1520-0485(1999)029<1404:TCOSFT>2.0.CO;2

Tomczak, M. (1995). Salinity variability in the surface layer of the tropical western Pacific Ocean. *Journal of Geophysical Research: Oceans*, *100*(C10), 20499–20515. https://doi.org/10.1029/95JC01544

Walesby, K., Vialard, J., Minnett, P. J., Callaghan, A. H., & Ward, B. (2015). Observations indicative of rain-induced double diffusion in the ocean surface boundary layer. *Geophysical Research Letters*, *42*(10), 2015GL063506. https://doi.org/10.1002/2015GL063506

Ward, B., Fristedt, T., Callaghan, A. H., Sutherland, G., Sanchez, X., Vialard, J., & Doeschate, A. ten. (2014). The Air–Sea Interaction Profiler (ASIP): An Autonomous Upwardly Rising

Profiler for Microstructure Measurements in the Upper Ocean. *Journal of Atmospheric and Oceanic Technology*, *31*(10), 2246–2267. https://doi.org/10.1175/JTECH-D-14-00010.1

Webster, P. J., Clayson, C. A., & Curry, J. A. (1996). Clouds, radiation, and the diurnal cycle of sea surface temperature in the tropical western Pacific. *J. Climate*, *9*, 1712–1730.

Wijesekera, H. W., Paulson, C. A., & Huyer, A. (1999). The Effect of Rainfall on the Surface Layer during a Westerly Wind Burst in the Western Equatorial Pacific. *Journal of Physical Oceanography*, *29*(4), 612–632. https://doi.org/10.1175/1520-0485(1999)029<0612:TEOROT>2.0.CO;2

Wilson, E. A., & Riser, S. C. (2016). An Assessment of the Seasonal Salinity Budget for the Upper Bay of Bengal. *Journal of Physical Oceanography*, *46*(5), 1361–1376. https://doi.org/10.1175/JPO-D-15-0147.1

Zappa, C. J., Ho, D. T., McGillis, W. R., Banner, M. L., Dacey, J. W. H., Bliven, L. F., … Nystuen, J. (2009). Rain-induced turbulence and air-sea gas transfer. *Journal of Geophysical Research: Oceans*, *114*(C7), C07009. https://doi.org/10.1029/2008JC005008

Table 3.1. Number of salinity drop events

Table 3.1. Number of salinity drop events

	all profiles collected	profiles with salinity drop events	profiles with rain events including Bay of Bengal	profiles with rain events		
salinity drop critera (<= XX PSU)	**-**	**-0.1 PSU**	**-0.1 PSU**	**-0.1 PSU**	**-0.5 PSU**	**-1.0 PSU**
10 day profiles	9,199	350	205	189	43	10
fast cycle profiles	7,780	631	335	180	41	4
all profiles collected	16,979	981	540	369	84	14

Table 3.2. Correlation of maximum salinity drop with CMORPH precipitation statistics

Table 3.2. Correlation of maximum salinity drop with CMORPH precipitation statistics

	Maximum rain rate prior to profile (mm/hr)			Rainfall accumulation prior to profile (mm)		
	3 day	**24 hr**	**last rate**	**3 day**	**24 hr**	**6 hr**
wind < 6 m/s	N	N	N	N	N	N
wind > 6 m/s	N	N	N	N	N	Y
all wind speeds	N	N	N	N	N	N

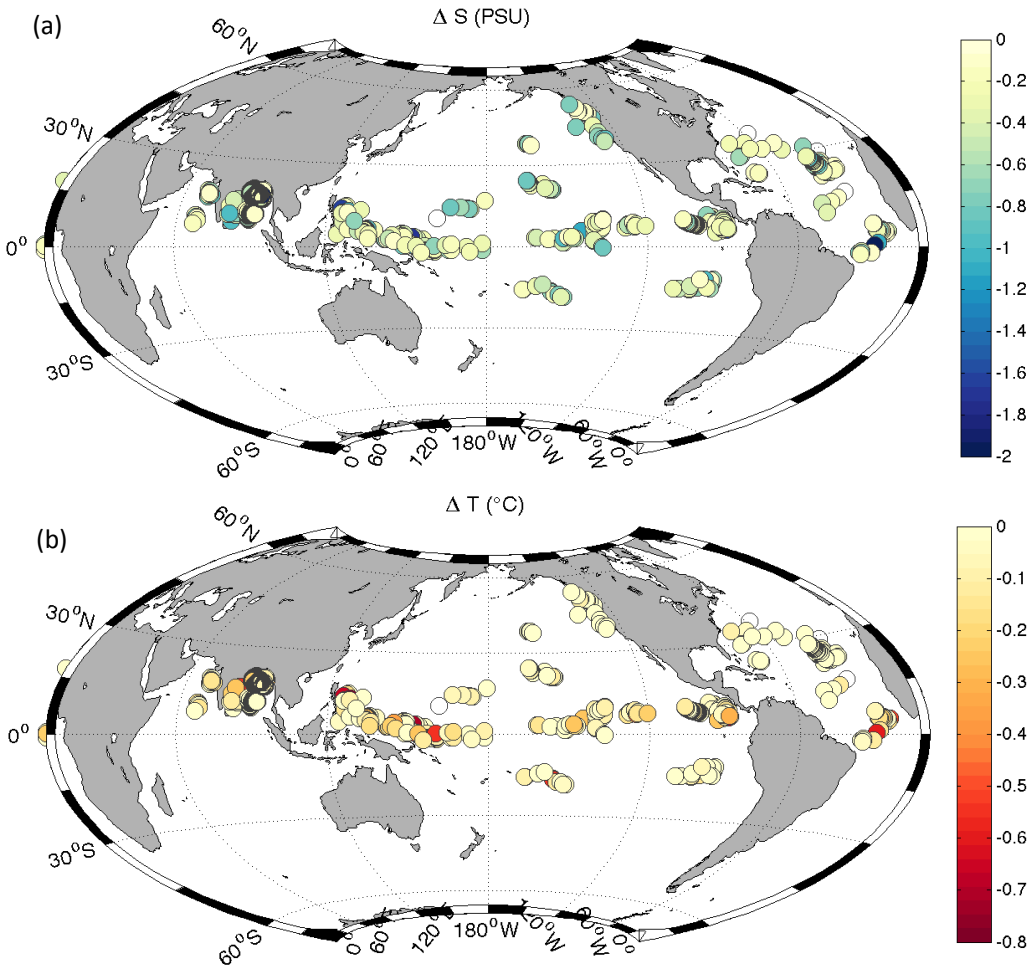

Figure 3.1. Location of salinity drop profiles sampled with 76 STS Argo floats between 20 December 2007 and 31 January 2016. (a) The amplitude of the maximum salinity drops in the upper 10 m and (b) the temperature drop at the depth of the salinity drop.

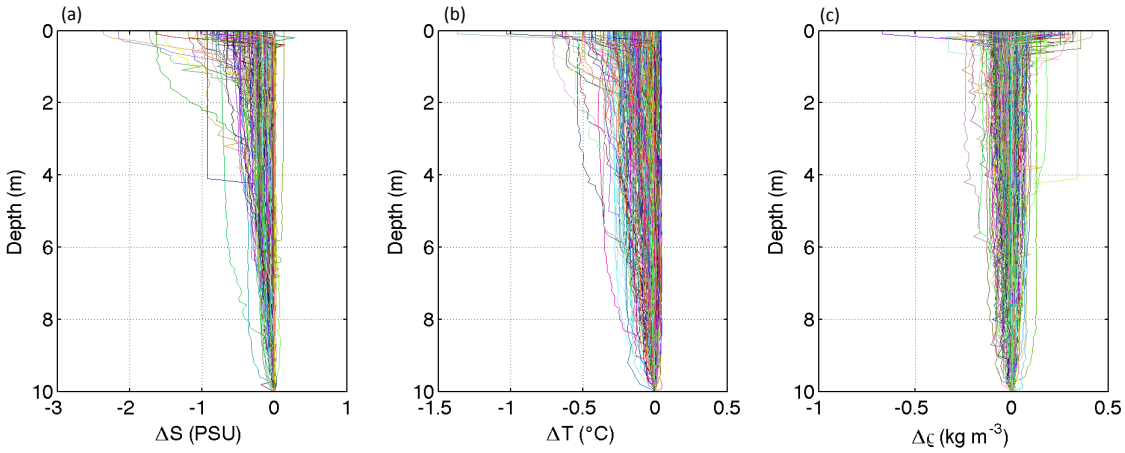

Figure 3.2. Difference from 10 m for (a) salinity, (b) temperature, and (c) density for all salinity drop events collocated with rainfall within 24 hours of profile time. Bay of Bengal profiles have been excluded.

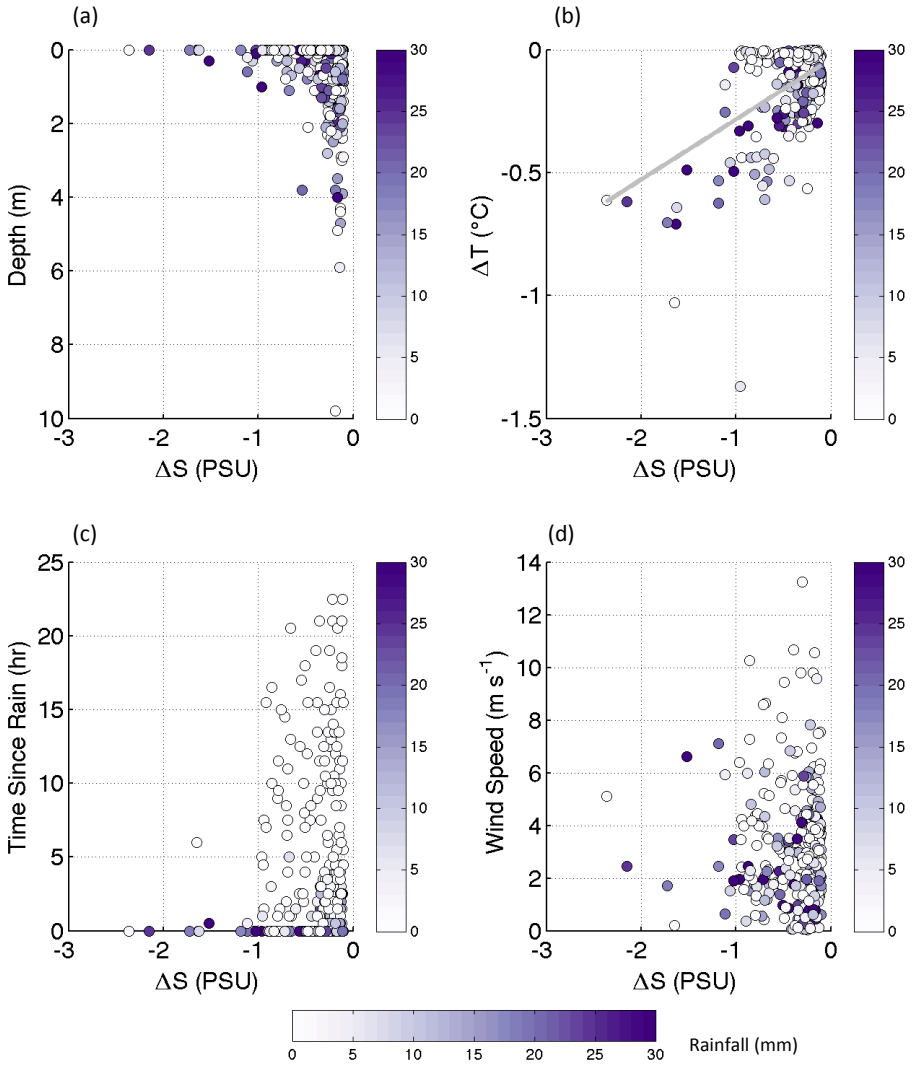

Figure 3.3. Maximum salinity drop versus (a) depth of the maximum salinity drop, (b), temperature drop at depth of maximum salinity drop (grey line significant linear best fit), (c) time between last rainfall and profile of salinity drop, and (d) wind speed at time salinity drop profile. Color indicates rainfall accumulation 6 hrs prior to profile.

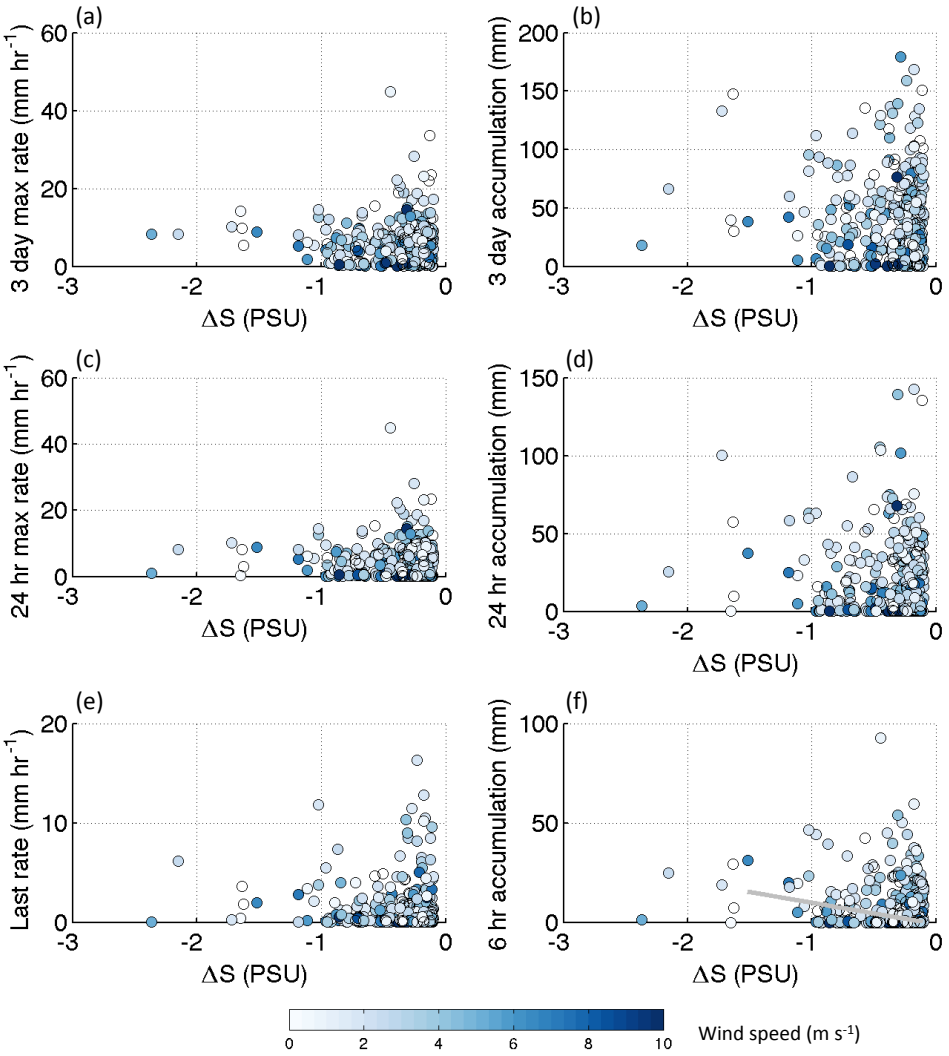

Figure 3.4. Maximum salinity drop versus CMORPH precipitation statistics; (a) 3 day maximum rain rate, (b) 3 day rainfall accumulation, (c) 24 hr maximum rain rate, (d) 24 hr accumulation rate, (e) last rain rate (greater than 0) prior to profile time, and (f) 6 hr accumulation rate where the gray line indicates significant best fit line for wind speeds > 6 m/s. Color indicated wind speed at time of float profile.

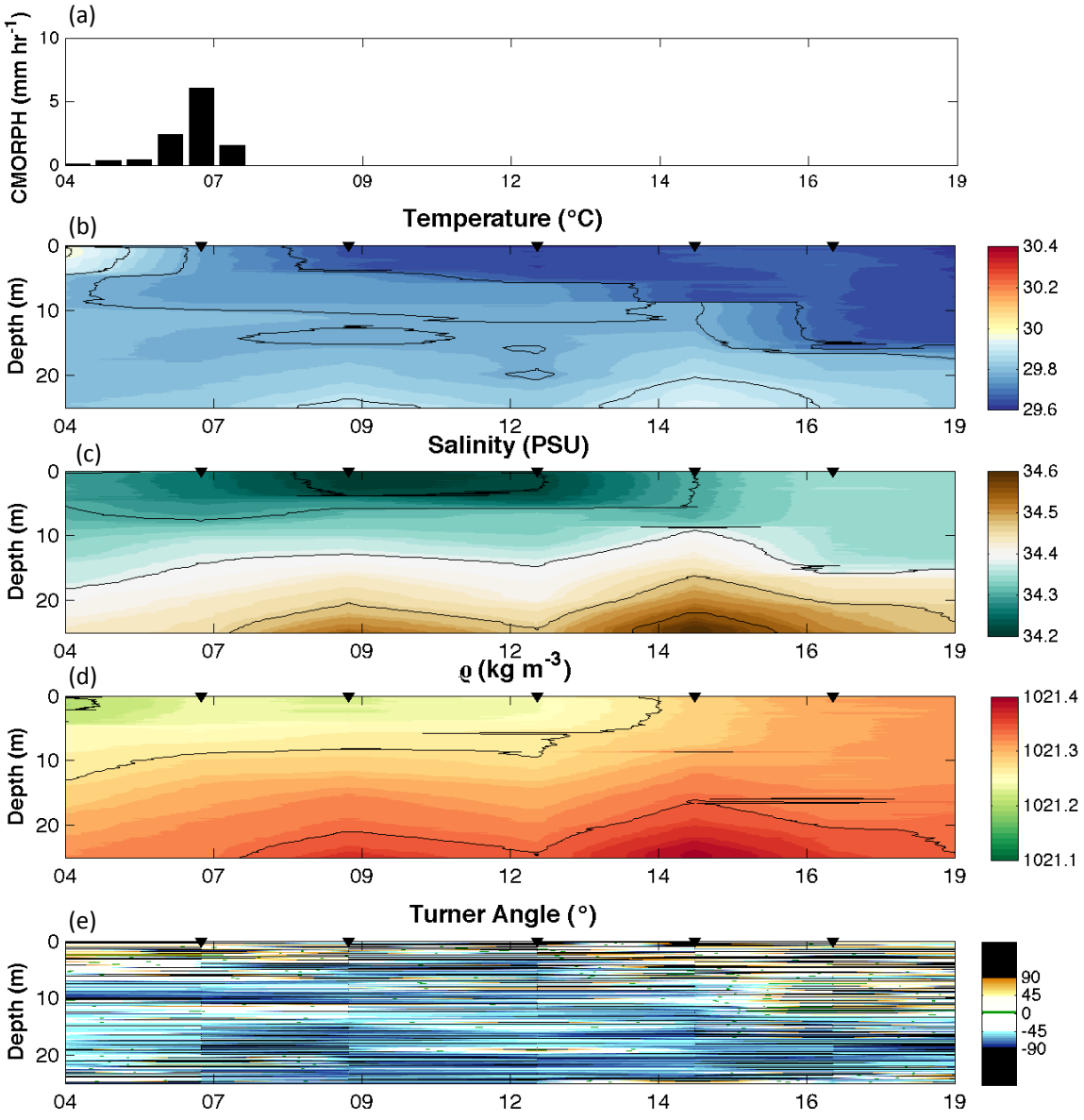

Figure 3.5. Salinity drop event observed by float 6115 in the tropical western Pacific (1.45°S,159.36°W) on 7 July 2009. (a) CMORPH rainfall (mm), (b) STS temperature (°C), (c) STS salinity (PSU). (d) STS density (kg m-3), (e) Turner angle (°).

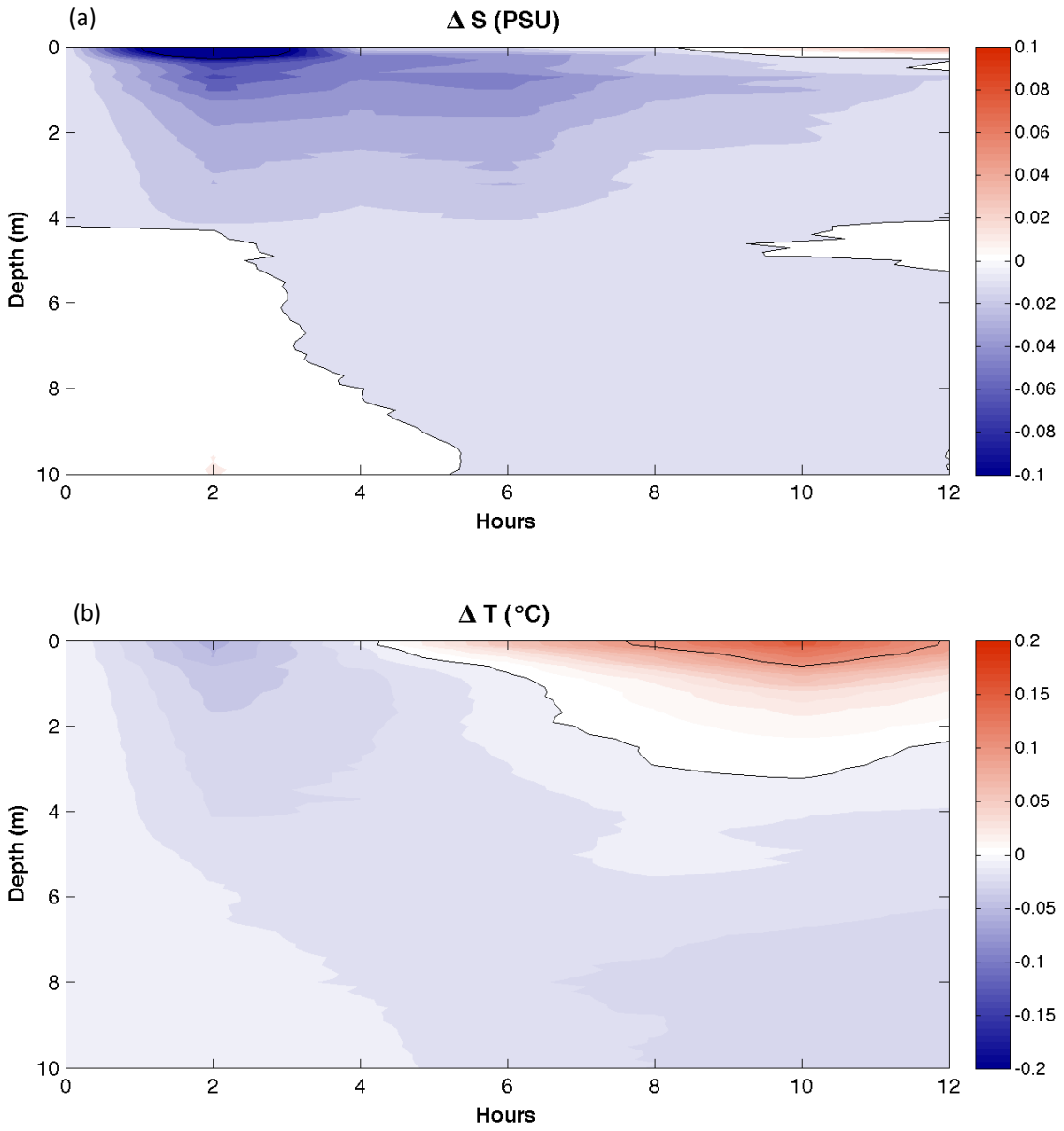

Figure 3.6. Average change from pre-drop profile for (a) salinity (PSU) and (b) temperature (°C), based on 86 salinity drop events.

Chapter 4

Annual and eddy subduction in the Salinity Processes in the Upper Ocean Regional Study (SPURS-1) area

Abstract

Mixed layer properties and subduction of high salinity water in an evaporation dominated region of the North Atlantic Ocean (~25°N, 38°W) that was heavily surveyed during the Salinity Processes in the Upper Ocean Regional Study (SPURS-1) are examined. High spatial resolution objective maps of temperature, salinity, and mixed layer depth (MLD)-created from Argo, Seaglider, and mooring data-show small spatial variability during the late spring and summer months and larger spatial variability during the late winter and early spring as the mixed layer shoals. Spatial variability is larger during the one-year study period than inferred from climatology. Mixed layer temperature and salinity are warmer and saltier than ranges associated with Subtropical Underwater (STUW), indicating a source for STUW north of the region or significant mixing after subduction. These higher spatial and temporal resolution mixed layer maps are combined with ADCP velocities and satellite wind stress fields to investigate the annual mean and eddy-varying subduction rates in the SPURS-1 region. SPURS-1 results are put into context with updated, Argo-era climatological values for the North Atlantic. Enhanced lateral induction contributions to annual subduction rates are observed, as is the importance of using a time-varying MLD for calculation of eddy contributions.

4.1 Introduction

Surface salinity patterns in the global ocean reflect global patterns of evaporation and precipitation controlled by atmospheric circulation cells (e.g., Schmitt, 2008). In regions with enhanced precipitation, such as the tropics and high latitudes, surface salinity is lower due to the input of freshwater. In evaporative regions, surface salinity is high due to the loss of freshwater, leaving salt behind. It has been suggested that in response to climatic changes, there may be an intensification of the freshwater cycle (Held & Soden, 2006; Seager et al., 2010; Skliris et al., 2016) observable in salinity trends (Durack et al., 2012; Skliris et al., 2016) that may result in shifts in the location of extrema (Scheff & Frierson, 2012). If we are to understand how ocean salinity patterns may change in the future, it is necessary to understand their current modes of variability. The Salinity Processes in the Upper Ocean Regional Study (SPURS) was designed to determine, on a variety of time and space scales, the physical processes that control upper ocean salinity. To reduce the number of mechanisms considered at a time, the two extremes of upper ocean salinity, fresh (primarily driven by precipitation) and salty (primarily driven by evaporation), have been being studied by two separate field campaigns. The first field campaign, located an evaporation-dominated region, is the focus of the present study. A precipitation-dominated regime is being examined during the SPURS-2 field campaign during 2016-2017.

The SPURS-1 field campaign took place in the center of the North Atlantic sea surface salinity maximum (SSS_{max}), near 25°N, 38°W (Figure 4.1). This location was chosen not only for its high evaporation but also its weak advection. The horizontal gradients of surface salinity are generally weak in the region with meridional gradients exceeding zonal gradients by an order of magnitude (e.g., Yu, 2011). The largest *E-P* values are found south of the SSS_{max} and thus maintenance of the SSS_{max} is likely due to a combination of evaporation, Ekman convergence,

vertical mixing, and subduction (Schmitt et al., 1989; Foltz & McPhaden, 2008). Studies using the ECCO (Estimating the Climate and Circulation of the Ocean) model have shown that ocean dynamics are just as important as *E-P* in the area (Qu et al., 2011). Of particular interest is the transfer of SSS_{max} properties away from the region via subduction. The majority of subducted water recirculates the basin before subducting again as North Atlantic Deep Water (Qu et al., 2013) while a smaller portion contributes to the shallow tropical overturning circulation (Schmitt et al., 1989; Qu et al., 2013) (Figure 4.1). In this manner, the SSS_{max} influences ocean circulation beyond the subtropics. While modeling studies have provided new insights, the variability of subduction dynamics in the subtropics is still not well understood. In the present study, densely spaced observations collected with a unique fleet of oceanic instrumentation during SPURS-1 are used to examine mixed layer variability and subduction dynamics in the SSS_{max} region.

4.1.1 *Subduction*

Subduction is the transfer of surface water through the base of the mixed layer and into the permanent pycnocline. While downward fluxes across the mixed layer base, detrainment, can occur throughout the year, it is only detrainment into the permanent pycnocline that is irreversible and qualifies as subduction. Water that is detrained into the seasonal pycnocline may be entrained back into the mixed layer months later (e.g., Qiu & Huang, 1995). The effective subduction period, the time period during which transfer into the permanent pycnocline occurs, typically lasts for several months beginning in late winter and is often associated with mixed layer shoaling due to increases in buoyancy. Due to the narrow effective window, subducted water brings with it the properties of the winter mixed layer (Stommel, 1979) and provides ventilation to the ocean interior. Estimation of subduction rates can be carried out several ways, including tracer/water age, kinematic, and thermodynamic approaches. In the kinematic

framework, subduction has vertical (Ekman pumping), horizontal (lateral induction (horizontal geostrophic advection across the mixed layer base)), and eddy-varying components whose strength fluctuates in space and time. Historically, Ekman pumping has been considered the only driver. Lateral induction was determined to be an equal contributor only after studies using tracer data revealed much higher subduction rates than had been found by studies which only looked at Ekman pumping (Jenkins, 1987). Lateral induction contributions are largest in regions of high mixed layer gradients, such as the region south of the Gulf Stream (Qiu & Huang, 1995). Eddy components and mixed layer depth variability have until recently been neglected.

More recently, mixed layer variability and eddy effects on subduction have been explored using Argo data in the Gulf Stream region (Trossman et al., 2009), the Southern Ocean (Sallée et al., 2010), and the North Pacific (Katsura et al., 2013). Argo float data provide improved estimates of mixed layer depth (MLD). Trossman et al. (2009) show use of the climatological mean MLD may underestimate annual ventilation rates compared to a year-to-year, varying MLD. In the Southern Ocean, eddy subduction due to time-varying properties may be as large as Ekman pumping and lateral induction by the mean field (Sallée et al., 2010). In some locations, modeling studies have shown eddies may reduce the annual subduction rate (Da Costa et al., 2005). Away from large fronts, in the calmer subtropical gyres, eddy contributions are thought to be small (D. Marshall, 1997). Using an ocean state estimate, Gebbie (2007) found that while integrated isopycnal eddy subduction was small in the subtropics, local eddy subduction rates can be large. This is consistent with studies of eddy impacts on other processes in the subtropics, such as freshwater fluxes (Gordon & Giulivi, 2014) and eddy transformation rates (Busecke et al., 2017).

4.1.2 *Subduction in the SPURS-1 area: historical overview*

Several previous studies have investigated subduction in the North Atlantic. The central mooring of the SPURS-1 study region is located west of the heavily studied region known as the beta triangle (Figure 4.1). Jenkins (1987) used the age of ^{3}H and ^{3}He on the density surfaces within 26.2-27.15 kg/m^3 to calculate a subduction velocity for this region. The calculated depth averaged subduction of 2.6 ± 0.3 x 10^{-6} m/s (~ 82 m/yr) was almost three times larger than Ekman pumping velocities, though later work concluded these values are likely an overestimate due to nonlinearities in the tracer ages (Jenkins, 1998). The geostrophic velocity field, which influences the lateral induction portion of subduction, was found to be variable in the region (Armi & Stommel, 1983). Additional work using ^{3}H and ^{3}He northeast of the SPURS-1 region showed lower subduction rates in that region that were still double the estimated Ekman pumping velocities and highlighted the importance of mesoscale processes (Joyce & Jenkins, 1993). Using climatological data for the North Atlantic, J. C. Marshall et al. (1993) estimated a subduction rate, including the influence of lateral induction, to be 50-100 m/yr in the SPURS-1 region, with the Ekman component being approximately 25-50 m/yr. They found the effective period of subduction (the period of permanent subduction) was between 2-3 months. Model results using both kinematic and thermodynamic methods have produced similar rates (Spall et al., 2000) as have observational studies using climatology and drifter data (O'Connor et al., 2005). Interannual variability in these rates is primarily due to changes in the winter mixed layer depth and the lateral induction term (Qu et al., 2016).

4.2 Subduction Calculation Methodology

Subduction rates can be estimated using a variety of methods depending on the datasets available. Previous studies in the North Atlantic have made use of kinematic, Lagrangian, and

tracer/water age methodologies. Each method has inherent limiting assumptions that prevent elucidating all the processes involved. Comparison of different studies is also difficult, though differences in methodology do provide a bound on rates and unique insights into dynamic processes. In the present study, we choose to utilize the kinematic framework developed by Cushman-Roisin (1987) and used by J. C. Marshall et al. (1993) and O'Connor et al. (2005) in the North Atlantic.

4.2.1 *Annual subduction rate*

The large quantity of data collected in the SPURS-1 area allows for the annual subduction rate to be estimated using a kinematic framework. Under that framework, the local, instantaneous rate of subduction s can be defined as (Cushman-Roisin, 1987; J. C. Marshall et al., 1993)

$$s(x, y, t) = -\frac{\partial h}{\partial t} - w_h - \boldsymbol{u}_h \cdot \nabla h \qquad (4.1)$$

where h is the depth of the mixed layer, $\boldsymbol{u}_h$ and w_h are the horizontal and vertical velocities at the base of the mixed layer, respectively, ∇ is the gradient operator in x and y, and t is time. Instantaneous subduction (4.1) is similar in form to the entrainment/detrainment term in a full salt balance. The terms of the right side of (4.1) represent the volume fluxes due to a time-variable mixed layer, vertical velocity across the mixed layer base, and advection across a sloping mixed layer (lateral induction). As derived in Cushman-Roisin (1987), a full volume budget would also include an evaporation minus precipitation (E-P) term on the right hand side of Equation 1. E-P over much of the North Atlantic is less than 1 m/yr (Schanze et al., 2010) and 0.89 m/yr during the SPURS-1 observational period (Farrar et al., 2015). Since E-P is an order of magnitude smaller than the other vertical terms, it is again neglected here as has been done in previous studies. While this is a good assumption in the SPURS-1 area and was one of the

reasons this location was chosen, the E-P term may not be negligible in regions with large precipitation, such as the SPURS-2 region.

When averaging over an annual cycle (or climatological periods), it can be assumed that no dramatic changes to the mixed layer depth occur and the first term on the right side of (4.1) becomes negligible. This assumes little interannual variability. Further, since we are only interested in permanent subduction, or the transfer of fluid into the permanent thermocline, h can be defined as the maximum winter mixed layer, H. Equation (4.1) can then be written as an annual subduction rate Sann,

$$S_{ann} = -\overline{w}_H - \overline{\boldsymbol{u}}_H \cdot \nabla H \qquad (4.2)$$

where $(-\overline{w}_H, \overline{\boldsymbol{u}}_H)$ are the annual mean velocities at the base of the winter mixed layer. The vertical velocity, $-\overline{w}_H$ may be divided into an Ekman pumping term, $\overline{w}_{Ek}$, and a correction for the portion of Sverdrup flow in the mixed layer. Applying this $\overline{w}_H$ becomes

$$\overline{w}_H = \overline{w}_{Ek} - \frac{\beta}{f}\int_H^0 \bar{v}\, dz \qquad (4.3)$$

where β is the gradient of f (the Coriolis parameter) and v is the meridional geostrophic velocity in the mixed layer. The Ekman pumping term is

$$w_{Ek} = \frac{1}{\rho} curl \frac{\tau}{f} \qquad (4.4)$$

where ρ is water density and τ is the wind stress. Here wind stress ($\tau = \rho_{air} C_D U_{10m}^2$) has been calculated with the Large and Pond (1981) parameterization of the drag coefficient, C_D, a constant air density (ρ_{air} = 1.22 kg/m^3), and satellite wind speeds for the wind at a height of 10 m (U_{10m}). Applying these, Equation (4.2) becomes

$$S_{ann} = -\frac{1}{\rho} curl \frac{\tau}{f} + \frac{\beta}{f}\int_H^0 \bar{v}\, dz - \overline{\boldsymbol{u}}_H \cdot \nabla H \qquad (4.5)$$

which is the rate (m/yr) per unit area of mass (volume) flux into the permanent thermocline.

Annual subduction rates from (4.5) can be used to determine the formation rate of a water mass. If it is assumed that mixed layer properties from late winter are conserved during subduction (Stommel, 1979), the formation area of a water mass can be defined as the surface area where the surface properties of temperature and salinity, and/or density are within the range associated with that water mass, with only the surface area during the period of effective subduction contributing to formation rates. Effective subduction begins when the buoyancy forcing changes sign (to positive) and the mixed layer begins to shoal (J. C. Marshall et al., 1993). Effective subduction in the subtropics typically ends 1-2 months after the change in the sign of the buoyancy forcing when the mixed layer depth matches that of the seasonal pycnocline (Gebbie, 2007; J. C. Marshall et al., 1993; O'Connor et al., 2002; Qiu & Huang, 1995). In the absence of buoyancy forcing data, O'Connor et al. (2002) estimate the formation area of water masses during effective subduction as the difference between the spring and summer sea surface areas with properties within a water mass density class. Multiplying this formation area times the annual subduction rate then gives the water mass formation rate.

4.2.2 *Eddy subduction*

Unlike the thermodynamic and water age methods, calculation of annual subduction using the kinematic method detailed above in Equation (4.5) does not take into account eddy contributions. Recent theoretical and modeling studies have shown that while eddy effects are relatively small in the subtropics, they are not negligible (D. Marshall, 1997; Qu et al., 2011). Following on the derivation by D. Marshall (1997), Gebbie (2007) derived eddy subduction rates for density classes using both a fixed and time variable mixed layer. Quantifications under both conditions are estimated here.

From Gebbie (2007), the surface $A_h(\sigma)$ can be defined as the mixed layer depth with density less than σ (i.e bounded by both the ML and the isopycnal σ). Separating (4.1) into time mean ($\bar{}$) and time-varying ($'$) components the mean subduction can be written as:

$$\overline{S_h}(\sigma) = \int^{\overline{A_h}(\sigma)} -(\overline{w}_h + \overline{\boldsymbol{u}}_h \cdot \nabla\overline{h})\, dA + \int^{\overline{A_h}(\sigma)} -(\overline{\frac{\partial \acute{h}}{\partial t}} + \overline{\acute{u_h} \cdot \nabla\acute{h}})dA + \overline{\int^{\acute{A_h}(\sigma,t)} s(x,y,t)\, dA} \tag{4.6}$$

The first term on the right is the mean subduction rate, while the second and third terms are components of the eddy subduction. The second term represents eddy subduction due to a time-varying MLD and the third term is due to time-varying isopycnals.

Invoking the mixed layer demon of Stommel (1979) (the preferential transfer of winter mixed layer properties), the mixed layer depth, h, in (4.6) is again fixed in time to the depth of the winter mixed layer, H, yielding

$$\overline{S_H}(\sigma) = \int^{\overline{A_H}(\sigma)} -(\overline{w}_H + \overline{\boldsymbol{u}}_H \cdot \nabla H)\, dA + \overline{\int^{\acute{A_H}(\sigma,t)} -(w_H + u_H \cdot \nabla H)\, dA} \tag{4.7}$$

In practice, the eddy subduction rate in (4.7) can be calculated as the difference between the annual subduction rate calculated using annual mean fields and the rate estimated using fields from shorter time scales. Optimally interpolated mixed layer maps and satellite wind fields allow for the second term in (4.7) to be calculated every 7 days. Details of the data used and mapping are provided in section 4.3.1.

While the assumption of a fixed mixed layer follows easily from previous studies, it is likely that if eddy subduction is important, it will show up not just in anomalous velocity fields, but also in a time variable mixed layer field. The use of (4.6) is therefore likely a more realistic estimate of the eddy subduction, though the second term $\int^{\overline{A_h}(\sigma)} -(\overline{\frac{\partial \acute{h}}{\partial t}} + \overline{\acute{u_h} \cdot \nabla\acute{h}})dA$ is dominated by the seasonal cycle. To account for this, Gebbie (2007) uses the idea of the mixed layer demon

differently. Assuming that effective subduction only occurs in the later winter/early spring as the mixed layer shoals, the effective period of subduction is very short. Over the short effective subduction period, the seasonal cycle of $\frac{\partial \acute{h}}{\partial t}$ can be approximated as a linear function. Subtracting this linear model from the second term, eddy effects can be isolated from the seasonal cycle.

4.3 Data Description

4.3.1 *Annual and eddy subduction in the SPURS-1 Area*

Annual mean and eddy subduction in the SPURS-1 area were determined using satellite measurements of wind and velocity along with in situ observations in the SPURS-1 area. For the current study, we define the SPURS-1 area as a 2° latitude by 2° longitude area extending from 23.5°-25.5° N and 37°-39° W, centered roughly on the Woods Hole Oceanographic Institution (WHOI) central mooring. 107,158 in situ measurements of various types collected in the SPURS-1 area during the primary study period, 1 October 2012 to 30 September 2013, are used in the current study. The locations of these profiles are shown in Figure 4.2. Details about the satellite and in situ observations follow.

4.3.1.1 *Mixed Layer Depth*

MLD in the SPURS-1 area was calculated from profiles of temperature and salinity obtained from a variety of instruments deployed during the SPURS-1 field campaign. Consistent with Monthly Isopycnal/Mixed-Layer Ocean Climatology (MIMOC) climatological estimates, the density algorithm of Holte and Talley (2009) was used to determine the MLD from observations. This algorithm examines potential density changes across the thermocline to first classify the profile as summer or winter, and then compares 8 different MLD estimates, including common gradient and threshold methods, to determine a final MLD. The algorithm looks for clustering

among the various MLD estimates, which helps to avoid anomalously shallow or deep MLDs often found with gradient methods. For SPURS-1 data, the density algorithm returns slightly shallower MLDs than the temperature algorithm (not shown). The average temperature, salinity and density within the determined ML are also calculated. After MLDs were determined for all profiles, objective maps of the mixed layer depth and its properties were made every 7 days using a Gaussian covariance of 0.5° (~50km) and 5 days.

Errors associated with MLD estimates are generally larger than other variables in subduction calculations. The vertical resolution of the data sources varies which limits the ability to resolve the depth of the mixed layer horizontal surface to ~5 m. The Holte and Talley (2009) algorithm uses linear interpolation to estimate the exact depth where criteria are met. On the small vertical scale between observations, this is likely a good assumption and reduces the representativeness error. The errors associated with the mapping are thus assumed to be the largest source of error in the MLD calculation as the instrument error, on the order of 0.005 °C and 0.01 PSU, is orders of magnitude smaller for all of the sensors deployed on various platforms. As such, the root mean square error (rmse) of the map residuals (13±7 m) was used in the Monte Carlo error analysis. Details about the sources of temperature and salinity data follow.

Central Mooring

An important component of the SPURS-1 campaign was the central mooring deployed by WHOI. The central mooring was located at 24.58°N, 38.00°W (Figure 4.2). The mooring was heavily instrumented in the upper 200 meters, with 1-10 dbar (1 Pa = 10^{-4} dbar) instrument spacing for temperature and 2-10 dbar spacing for salinity. Instrument spacing increased slightly with depth. Temperature and salinity were measured with the following Seabird Electronics, Inc. (SBE) and RBR Ltd. (RBR) conductivity, temperature, and depth (CTD) instruments: SBE 16,

SBE 37, SBE 39 (temperature only), and RBR XR-420. Temperature and salinity values were recorded every 5 min, resulting in 99,654 moored profiles collecting during the study period.

Seagliders

6 Seagliders deployed by the University of Washington/University of Washington-Applied Physics Laboratory heavily surveyed the SPURS-1 study area. The Seagliders were deployed three at a time for 6-month missions. Seaglider turnaround (recovery of 3 Seagliders and deployment of 3 more) occurred in March 2013. The Seagliders operated in a nested horizontal sampling scheme with one glider sampling in a bowtie pattern around the central mooring, one in a larger diamond around the mooring, and the last in a larger box around the central mooring (Figure 4.2). All Seagliders dove from the surface to 1000 m and back continuously, sampling temperature and salinity on both the up and down dives. Data is available with 2 dbar vertical resolution. Each seesaw dive took ~6-7 hours to complete and covered ~4.5 km. 2,364 glider-based profiles were collected during the study period.

Profiling Floats

During the SPURS-1 field campaign, 18 Argo-type profiling floats were deployed in the SPURS-1 area. All floats were equipped with a primary SBE 41CP CTD and an auxiliary SBE STS CTD to measure temperature and salinity, as well as a PAL (Passive Acoustic Listener) that measures wind and rainfall (Yang et al., 2015). Data from the primary SBE 41CP CTD were used in this study. Floats were deployed between 9-30 September 2012 in a high-density ~0.5° grid surrounding the central mooring (Figure 4.2). Floats operated on a standard Argo-type float mission (drift at 1000 dbar, profile from 2000 dbar to 4 dbar) with the exception that profile

frequency was increased to 1-5 days. Additionally, a small number of floats completed fast cycle missions, where the floats were programmed to profile temporarily over the upper ~150 dbar continuously every 2-3 hours for periods of up to 2 months. Profiles of temperature and salinity from the SBE41CP CTD had a vertical resolution of 2 dbar in the upper 1000 dbar. The floats remained remarkably close to the central mooring (300 km) through mid-winter and half remained within 300 km for the duration of the primary study period. 556 Argo profiles were collected within the study area over this time. Velocity data from the central mooring is discussed in section 4.3.1.3

PMEL Prawler

2 Platform and Instrumentation for Continuous Observations (PICO) moorings were deployed with mean locations of 24.74°N, 322.05°W (PICO 1000) and 24.51°N, 322.19°W (PICO 3000) (Figure 4.2). Both moorings were equipped with a Prawler (Profiler + Crawler) CTD that profiles from ~8 m to 500 m while descending under buoyancy (Osse et al., 2015). Wave energy is then utilized to ascend. It takes ~2-4 hrs to complete one ascend/descend cycle. Pico 1000 was adrift from 19 February 2013 until 2 April 2013. Data collected during this time period were not used in the present study. Additionally, PICO 3000 did not collect data in the surface layer between 16 December 2012 and 2 April 2013. Only profiles where the upper 200 m was well sampled are used in this study. In total 4,584 samples of temperature and salinity were obtained. The vertical resolution of PICO data varies from profile to profile but is generally 1-3 dbar.

4.3.1.2 *Ekman Pumping*

Advanced scatterometer (ASCAT) estimates of wind speed and direction were used in calculating the Ekman pumping term (Equation 4). 7 day and monthly, 1/4° x 1/4° gridded,

global (90°N to 90°S), ASCAT wind vector data available from Remote Sensing Systems Inc. (RSS) are used here. Data collected during rainfall is not removed from the dataset since interference of rain with measurements in the radar band used by ASCAT (5.2 GHz, C-band) is small (Figa-Saldaña et al., 2002). The Large and Pond (1981) drag coefficient parameterization was used to calculate wind stress, τ. Objective maps of ML density, used to identify the water mass being subducted as well in calculation of the Ekman pumping term, were created using the average density in the ML as determined using the Holte and Talley (2009) density algorithm and the same mapping procedure described in section 4.3.1.1. Sampling errors associated the spatial and temporally smoothed ASCAT data are ~0.21 ± 0.09 (Schlax et al., 2001). Mapping errors associated with the density field (0.034 ± 0.016 kg/m^3) as a percent of the signal are small in comparison.

4.3.1.3 *Mixed Layer Velocities*

Horizontal velocities in the mixed layer during the study period were obtained from two 300 kHz RD Instruments (RDI) acoustic Doppler current profilers (ADCP) deployed on the WHOI central mooring located at 24.58°N, 38.00°W (Figure 4.2). Two upward looking ADCP's were affixed at 75 m and 145 m and measured hourly, zonal and meridional velocities in 2 m depth bins from ~ 18-140 m. Mooring GPS data was used to correct ADCP currents for mooring movement (0.05 cm/s). The ADCP accuracy, 0.5 % of water velocity or ~0.5 cm/s, was used as an error estimate for both velocity components in the Monte Carlo analysis. Due to the limited availability of high quality velocity data, evaluation of annual and eddy subduction in the SPURS-1 area is limited to one point, the central mooring location. Satellite based velocity estimates were used to investigate the spatial variability of these processes beyond the central mooring, but the results

were not statistically significant due to large errors associated with the geostrophic velocities (Scharffenberg & Stammer, 2010) and are not presented here.

4.3.2 *North Atlantic Climatology*

Previous studies using kinematic methods to estimate annual subduction in the North Atlantic utilized climatologies based on temporally and spatially sparse ship and buoy measurements or smoothed reanalysis products (J. C. Marshall et al., 1993; O'Connor et al., 2005). To put the high resolution annual and eddy-varying SPURS-1 area subduction rates in context, annual mean subduction rates in the North Atlantic (5°-60°N and 0°-80°W) are revisited using climatologies constructed during the more recent, data rich era. Satellite measurements of surface winds and the unprecedented number of temperature and salinity profiles collected by the Argo program have allowed determination of new, higher spatial resolution wind, velocity, and mixed layer climatologies. All datasets were downsampled to the resolution of the coarsest dataset (1°x1°). Details of the datasets used to construct an updated climatological view follow.

Scatterometer Climatology of Ocean Winds (SCOW)

SCOW, a QuikSCAT based climatology, was used for ocean winds. SCOW was constructed via harmonic analysis from 10 years (1999-2009) of QuikSCAT data (Risien & Chelton, 2008). Monthly maps are available on a 0.25° x 0.25° grid from ~±70° N/S. The combined measurement and sampling errors for the spatiotemporally smoothed QuikSCAT fields is estimated to be ~0.11 ± 0.05 m/s (Schlax et al., 2001). These errors are assumed to be smaller than the errors associated with the representativeness of the data (due to the limited 10 year record and year to year variability). Risien and Chelton (2008) minimize the effects of this error by only using the first 4 terms of the harmonic analysis. While calculation of the curl amplifies

errors, the high spatiotemporal sampling of QuikSCAT reduces uncertainties compared to previous in situ climatologies as shown by the lack of nonphysical patterns in wind stress curl maps (Risien & Chelton, 2008).

Monthly Isopycnal/Mixed-Layer Ocean Climatology (MIMOC)

North Atlantic mixed layer maps and density were determined from the mixed layer pressure, potential temperature, and salinity data files available as part of the MIMOC suite of ocean property maps. MIMOC optimally interpolated fields are available on a monthly, 0.5° x 0.5° grid from 90°N to 80°S on 81 pressure surfaces (resolution 5 m, 0-100 m; 10 m, 100-350 m). The optimal interpolation scheme emphasizes data from the data rich Argo era (2007-2011), though data from Ice-Teathered Profiler CTDs and other hydrographic data platforms in the World Ocean Database (WOD09) are also included (Schmidtko et al., 2013). MLD is determined using the Holte and Talley (2009) density algorithm where mixed layer pressures < 20 dbar are removed. Formal error estimates are not included in the MIMOC data set. Measurement errors are assumed to be much smaller than sampling, mapping, and representativeness errors. Since only the measurement errors are known, we assume errors in the MLD of 5 m. This represents the vertical resolution of the vertically gridded MIMOC dataset in the upper ocean and is 1-2 times the vertical resolution of most Argo floats.

Absolute Geostrophic Velocities from Argo (AGVA)

Mixed layer geostrophic velocities were obtained from AGVA, which uses Argo CTD and parking-depth drift data to compute dynamic height estimates on 29 pressure surfaces between 5 dbar and 2000 dbar, with a vertical resolution between 5-50 dbar in the upper 300 dbar. Geostrophic velocities are referenced to the velocity at 900 dbar as determined from float

trajectories. Global (69°N to 75°S), monthly AGVA data is available on a 1° x 1° degree grid from December 2004 to November 2010 (Gray & Riser, 2014). The arithmetic average of AGVA data over the 6-year period was calculated to determine a climatological value for each month. The mean and standard deviation of the meridional and zonal velocities is shown in Figure 4.3. Velocity components on the pressure surface closest to the mixed layer depth were used for calculation of the subduction rate. Provided error estimates for the gridded velocity fields (includes both measurement and sampling errors) are on the order of 0.006 m/s in the SPURS-1 area.

4.3.3 *Error Analysis*

Errors associated with annual subduction rates are difficult to obtain via formal error propagation methods. As such, previous studies, as well as this study, have not generally completed a satisfactory error budget. J. C. Marshall et al. (1993) assumed that the errors in vertical pumping and lateral induction components where each ~40%. In the middle of the North Atlantic gyre, the error was thus determined to be ~30% for annual subduction, 15 m/yr. O'Connor et al. (2005) assumed that the measurement errors were much less than the errors in the assumptions and estimated errors of 7-20% in subduction rates over the North Atlantic and further used the differences between the tracer and drifter methods as an estimate of the total error (22%) though this comparison also includes the effect of eddies.

Error estimates for this study were determined using a Monte Carlo simulation of the data. For both the climatological and SPURS-1 area subduction rates, error estimates for the data products or mapping were used to produce random perturbations to each dataset. The sampling and mapping errors are larger than instrument errors for both the satellite measurements and SPURS-

1 area assets. Errors associated with each data product are discussed along with the data description in sections 4.3.1 and 4.3.2.

In the Monte Carlo simulation all data product errors (sampling and mapping) were assumed to have a normal distribution, and 10^3 random samples were drawn from a Gaussian distribution. The subduction rates were then recalculated using the randomly variable data product values. The error for each component of subduction is reported as the standard deviation of the resulting Monte Carlo histogram. The component of annual subduction with the largest error is lateral induction. This is due to large uncertainties in the MLD. ML maps are subject to errors associated with the vertical resolution of the temperature and salinity datasets as well as errors in the horizontal smoothing. Other components that utilize MLD maps also have higher errors. In general, error of the present study is ~15-50 %.

4.4 Results and Discussion

4.4.1 *SPURS-1 mixed layer properties and variability*

Shown in Figure 4.4 is the depth of the ML in the SPURS-1 area determined using the Holte and Talley (2009) density algorithm on SPURS-1 observations. After the MLD was determined, the average temperature, salinity, and density over the MLD were also calculated. The annual cycle of mean values from the objective maps are described. When the SPURS-1 assets were deployed, the MLD in the SPURS-1 area was near its mean annual value, 47 m. The average ML temperature and salinity were at a maximum, 26.98 °C and 37.56 PSU, respectively. Potential density, primarily controlled by temperature, was at a minimum 24.64 kg/m^3. The ML continued to deepen throughout the fall and early winter until reaching a maximum spatial mean value of 96 m the first week of February 2013. Temperature and salinity reached their minimum values, 22.98 °C and 37.41 PSU shortly after. Density was at a maximum value of 25.77 kg/m^3. ML

properties during the maximum MLD were used in calculating the annual subduction rate. After reaching its maximum depth, the ML shoaled until April, before remaining relatively constant throughout the summer. ML temperature begins to increase in April, shortly after the ML has reached its minimum while the mean salinity starts to increase despite the signature of fresh pools.

The maximum mean MLD in the SPURS-1 region is 10 m deeper than the climatological average MLD in the SPURS-1 area from MIMOC. The 7-day objective maps show significant short-term variability; however, the annual mean value is 5 m shallower than climatology. Temperatures during the study period were warmer by 0.23 °C throughout the fall and winter than climatology. As a result, the ML was slightly less dense. ML mean salinity was identical to climatology, with more short-term variability.

The timing of the maximum MLD (early February) is similar to MIMOC. Previous studies have assumed that the maximum occurs slightly later, in March (J. C. Marshall et al., 1993; Qu et al., 2016). Modeling studies have determined that effective subduction begins the last week of February in this area (Gebbie, 2007). Figure 4.5 shows the month of the maximum MLD from the MIMOC dataset. Across the North Atlantic subtropics the month of maximum MLD varies from December to March. Since the time resolution of MIMOC is monthly, this may represent differences in MLD maximum timing of 2 to 16 weeks (last week of December/first week of January to first week of December/last week of March) across a few degrees of latitude/longitude.

The depth of the ML in the SPURS-1 region shows high temporal and spatial variability. While the general trend in MLD shows a deepening from September to January and a shallowing from February to June, there is large variability at shorter time scales. Figure 4.6 shows wind stress

and geostrophic velocities over the SPURS-1 domain. Qualitatively, it can be seen that changes to the MLD often occur following changes in the wind and velocity field. Salinity in the SPURS-1 area shows temporal variability in late May and early July of unknown origin. The fresh, warm signature of this variability is similar to events described by Busecke et al. (2014) earlier in the year that were the result of advection of water south of the region. Shown in Figure 4.7 are objective maps of MLD over the study period, which reveal large spatial variability. The MLD is spatially uniform when the floats are deployed. As the mixed layer begins to shoal in winter, there is large spatial variability in MLD (> 50 m over 2°). Significant variability is also present during the summer months. This horizontal variability was also observed by Busecke et al. (2014) in the temperature and salinity field. The small-scale variability of the MLD in the SPURS-1 area is much larger than interpreted from coarser resolution climatologies used by Marshall et al. (1993) and O'Connor et al. (2005). This could enhance lateral induction contributions to subduction in the subtropics.

4.4.2 *Subtropical Underwater (STUW)*

Subtropical Underwater (STUW) is lower density (26.0 kg/m^3) mode water identified by its shallow salinity maximum. This maximum is found throughout the North Atlantic subtropics (O'Connor et al., 2005; Qu et al., 2016). Due to its unique salinity signature and density range, it has been proposed that STUW forms via subduction of sea surface salinity maximum (SSS_{max}) water during the late winter. The SPURS-1 region, located within the center of the SSS_{max}, could therefore be located within its source region. O'Connor et al. (2005) used World Ocean Database data to identify profiles containing a salinity maximum and then identify the average temperature, salinity, and density ranges associated with the maximum. The mean and range of STUW properties are 20.4 (20.4-22.2) °C, 36.73 (36.72-37.10) PSU, and 26.0 (25.6-26.3) kg/m^3.

If it is assumed that no transformation occurs during the subduction process, areas with a surface expression of properties in these ranges can be used to identify STUW formation regions.

Shown in Figure 4.9 is the spatial extent of STUW property ranges identified with the MIMOC dataset. Regions with a STUW temperature range surface expression spread east to west across the basin during all months of the year. There is a seasonal migration northward in the summer/fall and southward in the spring/winter. Salinity ranges are located in the center of the basin throughout the year with a slight increase in surface area in the late summer. Overlap of the STUW temperature and salinity ranges occurs in the eastern portion of the basin beginning in October and spreads westward during the winter months before retreating east again in spring. From December to May, overlap of the temperature and salinity ranges lies just slightly north of the SPURS-1 region. STUW properties are found in the northern extent, but not over the entire study region from February to April. That there is not a surface expression of STUW properties in the SPURS-1 area (located in the core of the SSS_{max}) during the late winter when subduction occurs may indicate that STUW forms slightly to the north of the region. Modeling studies (Qu et al., 2013) indicated that water subducted in the SSS_{max} region may circulate around the basin with a small portion upwelling in the tropics as part of the subtropical cell (shallow meridional overturning circulation), and most recirculating the basin before subducting again, this time as STUW, further north in the basin (Figure 4.1).

The ML properties of SPURS-1 observations also are not in STUW ranges of O'Connor et al. (2005). Figure 4.4 shows the average mixed layer properties in the SPURS-1 area throughout the study period. During all times of the year the temperature and salinity are warmer and saltier (by ~0.5 °C and 0.3 PSU in the late winter) than the ranges associated with STUW. The size of the warming and salinification of the ML is on the order of observed 50 yr temperature and salinity

trends in the North Atlantic (Durack et al., 2012) and may represent not only interannual variability, but also larger scale differences in upper ocean properties between the present study and the O'Connor et al. (2005) study.

Density of the ML in the study area does enter the ranges associated with STUW from the beginning of February to the end of April. In contrast, this may show that STUW does form in the SPURS-1 area, but the water mass mixes as it subducts. Temperature and salinity in the subtropics can be density compensating (de Boyer Montégut et al., 2004) and previous studies have shown the presence of spice anomalies, salinity and temperature variations on a surface of constant density (Kolodziejczyk et al., 2014). Fresher, cooler subsurface water may mix with the warmer, saltier SSS_{max} along isopycnals during subduction with further (small) diapycnal mixing along the spreading path in the basin. Recently, Qu et al. (2016) used the criteria of a vertical salinity maximum > 36.5 PSU within the 24.5-26.5 kg/m^3 density surfaces to identify the density most likely to contain the SSS_{max} signature. The broader, lighter range of density surfaces 25.0-26.0 kg/m^3 bound these salinity maxima and were associated with temperatures > 23.0 °C. This new definition of STUW fits all ML observations in the SPURS-1 area and thus would directly link STUW formation to the subduction of SSS_{max} water without significant mixing required. It may be of more utility in understanding climatic changes to SSS_{max} water (as a property extreme) to expand the property definition to one that is defined primarily by salinity and less sensitive to warming trends.

4.4.3 *North Atlantic Climatological Subduction*

Climatological annual subduction (Equation 5) for the Argo and satellite era was calculated using SCOW winds, AGVA velocities, and MIMOC mixed layer depths. It is only the vertical transfer of fluid below the depth of the deepest MLD in winter that contributes to subduction. As

such, for each grid point, the month of the deepest MLD was determined and the ML map for that month used to calculate the annual rate at that grid point. Figure 4.5 shows the month in which the deepest mixed layer occurred. Over much of the North Atlantic, the deepest mixed layer occurs in January and February. Previous studies have used March ML maps in determining subduction rates. While March is likely a good estimate for the active subduction south of the Gulf Stream extension, it is too late for much of the subtropics. If the ML has already begun to shoal before March, it is likely the annual subduction rates would be over or underestimated. The use of a variable ML month helps to avoid this.

Total annual subduction and the magnitudes of contributing processes vary over the North Atlantic (Figure 4.10). Controlled by atmospheric circulation patterns, Ekman pumping contributes positively to subduction across the North Atlantic from 15-45 °N. Lateral induction shows two regions of large positive contributions to subduction. The largest of these is located in the northern extent of the basin and is associated with the ML variability south of the Gulf Stream (J. C. Marshall et al., 1993; Trossman et al., 2009). There is a secondary center of subduction in the subtropics associated with smaller mesoscale ML variability. This secondary hotspot has also been observed using Lagrangian methods with World Ocean Database data and the ECCO model (Qu et al., 2013). Upward motion associated with Sverdrup flow slightly reduces the annual subduction rate north of ~25 °N. The total annual subduction varies over 150 m/yr over the North Atlantic. The sum of these terms can be generalized from (4.5) as

$$Annual\ Subduction\ (S_{ann}) =$$

$$Ekman\ Pumping\ (EP) - Severdrup\ (\mathrm{Sv}) + Lateral\ Induction\ (LI) \qquad (4.8)$$

The average of each of these components, in m/yr, over the SPURS-1 box (Table 1) are

$$41 \pm 6\ (S_{ann}) =$$

$$33 \pm 6\ (EP) - 11 \pm 4\ (\mathrm{Sv}) + 19 \pm 8(LI)$$

Across the North Atlantic, the annual subduction rate and regions of enhanced subduction agree with previous studies. Subduction rates in the SPURS-1 area for this study and previous studies are shown in Table 1. Climatological annual subduction rates from this study are in agreement with those from previous climatology based studies (J. C. Marshall et al., 1993; O'Connor et al., 2005). While the total annual subduction rate is similar, the balances between the components are slightly different in the present study. The QuickSCAT based Ekman pumping component is 17 m/yr, lower than both J. C. Marshall et al. (1993) and O'Connor et al. (2005). This reduction to total subduction from Ekman pumping is compensated with an increase of 19 m/yr in the lateral induction term. Enhanced lateral induction contributions are thought to be the result of better resolving MLD variability. MIMOC has twice the vertical resolution of the World Ocean Atlas (WOA94) climatology (Levitus et al., 1994; Levitus & Boyer, 1994) used by O'Connor et al. (2005), and the Holte and Talley (2009) algorithm may better represent the ML depth. The average ML gradient (deeper in north) combined with geostrophic velocities that are generally southward, are conducive to subduction. It is only due to smaller scale horizontal variability that lateral induction occurs. Error estimates for the lateral induction components are ~42 % due to uncertainties surrounding MLD mapping procedures (Table 1). Despite this large error, lateral induction is a climatologically significant contributor to subduction rates in the subtropics. Error estimates for the annual subduction rate are ~15 %.

4.4.4 *Subduction in the SPURS-1 area*

4.4.4.1 *Annual Subduction*

Annual subduction in the SPURS area was calculated at the central mooring location (24.58°N, 38.00°W) in the same manner as the climatological estimate. The winter MLD used in

the calculations was the maximum MLD at the central mooring location, interpolated from the objective maps. The maximum MLD occurred on the 9 February 2013 objective map. There is no net annual subduction at the central mooring location during the SPURS-1 observational period (Table 1). Obduction, the destructive process of entraining water from the permanent pycnocline back into the surface, dominates at this point in the study area. This is the result of smaller than normal or negative contributions from all terms. Ekman pumping is 80% smaller than most climatological estimates at 6 m/yr. The Sverdrup contribution again reduces the total rate (-30 m/s), but by a larger amount than normal due to higher velocities (Figure 4.6). Lateral induction has a very large negative contribution during the study year, -934 m/yr, due to northward net velocities. The errors associated with this term are the largest, due to uncertainties in the mixed layer objective maps. Negative lateral induction contributions were also observed by O'Connor et al. (2005), though of a much smaller size. Total annual subduction is -958 m/yr again with large uncertainty (50%) due to uncertainties in the lateral induction component (Table 1).

This means that in winter of 2013, no water in the 24-26 kg/m^3 density class range was formed at the central mooring location. This disagrees with Qu et al., (2016) who observed positive, though lower than normal, net subduction and water mass formation in the region during the winter of 2013. In the larger SSS_{max} region, vertical pumping was close to normal during the year but lateral induction was close to zero. It is unknown if net subduction took place at other points away from the central mooring in the SPURS-1 area during the winter of 2013. It is possible that large net positive lateral induction could be found at other points in the SPURS-1 region if southward velocities were present. Differences between the average velocity at the central mooring (in both sign and magnitude) and estimates from either purely geostrophic (dynamic

height) or dynamic height plus Ekman models of ocean velocity highlight the portion of velocity variance at the depth of the mixed layer not explained by these conceptual models or the assumption of slab dynamics (Ralph & Niiler, 1999). Capturing the full velocity variance could account for a portion of the observed obduction. Additionally while the annual subduction rate of Equation (4.5) does not formally incorporate eddy contributions, at smaller space scales, the effects of mesoscale eddies may begin to appear - even with a single time point ML map and annual mean velocities. Large ML gradients and velocity variability could be a result of mesoscale eddies. Calculation of the SPURS-1 area annual subduction rate with (4.5) utilizes a single map of the deepest winter mixed layer during the week of 9 February 2013. Due to the density of SPURS-1 observations as well as the short time period, our MLD map represents the mesoscale eddy field and consequently larger MLD gradients than multiyear averaged fields, which average over this variability. MLD maps here represent a snapshot of a highly time variable field. Use of fully instantaneous kinematic subduction rate would likely better represent subduction dynamics as suggested by the modeling work of Da Costa et al. (2005). While each jump in observational spatial resolution (inferred from the change in resolution between climatologies and SPURS-1 observations) increases MLD variability (and consequently lateral induction contributions) better resolution of the time variable field is needed to fully represent subduction dynamics. MLD time variability could explain why lateral induction is the largest contributor to year-to-year variability in the SSS_{max} region (Qu et al., 2016).

4.4.4.2 *Eddy subduction*

We now try to more formally quantify eddy (time variable) subduction rates. Using observations, eddy subduction rates in the SSS_{max} and SPURS-1 area are calculated directly for the first time. O'Connor et al. (2005) made an indirect observational estimate by comparing tracer and

kinematic methods. We examine eddy subduction using two methods. First, an estimate of the eddy subduction was undertaken using the standard estimate of eddy components as a difference between 7-day maps and the annual mean (Equation 7). Using this method, eddy subduction is 5 m/yr. This point value is larger that that found by (Gebbie, 2007) and similar to the 8 m/yr difference between tracer and kinematic methods determined by O'Connor et al. (2005). Averaged over long time periods, the difference between annual kinematic subduction rates and tracer studies may reflect eddy subduction contributions. The first eddy subduction method does not allow for the ML depth to vary however. Looking at Figure 4.4 large temporal variability in the MLD is evident, especially during the period of effective subduction. If there is a contribution from eddies to subduction, it is likely to come via MLD variations and lateral induction.

Allowing the MLD to vary in time, the annual subduction can be divided into mean and eddy components (Equation 6). These terms were calculated only during the effective period of subduction so that annual cycle does not dominate the signal. The effective subduction period was determined to start when the ML began to shoal, indicating the presence of buoyancy forcing, on 9 February 2013 and ended two months later on 30 March 2013, when the MLD stabilized. The seasonal cycle of $\frac{\partial \acute{h}}{\partial t}$ was removed using a linear best fit over the two month period. Using this method, eddy subduction is -8,160 m/yr (net obduction) at the central mooring location. This is again the result of large MLD gradients during the effective subduction period as well as large northward velocities. While an order of magnitude larger, this obduction rate agrees with Gebbie (2007) who found locally higher eddy subduction/obduction rates in the subtropical Atlantic. The size of the SPURS-1 region is close to the size of mesoscale variability (50 km Rossby radius). It is likely that each hotspot of eddy subduction may be accompanied by

an eddy hotspot of obduction. Further, eddies in the SPURS-1 region may set up large gradients on which diffusion can then act. Busecke et al. (2017) found 2 Sv of transformation by eddies in the North Atlantic. Eddy kinetic energy begins to rise during the effective subduction period, which could mean transformation of SSS_{max} water occurs concurrent to subduction. If the eddies bring cooler, less fresh water, this could also explain the property disconnect between SSS_{max} values and STUW values.

4.5 Conclusions

Using a multitude of observational datasets, we examined mixed layer variability and subduction rates in the North Atlantic SSS_{max} region. The mixed layer was spatially homogenous when the assets were deployed and remained relatively uniform as the mixed layer deepened. The maximum MLD was earlier in spring than in northern portions of North Atlantic. In spring, as the ML shoaled, there was high temporal variably and spatial variability was also at a maximum. Observed MLD gradients are much larger than those inferred from climatologies used in previous studies, which has large impacts on subduction rates. The SPURS-1 ML was slightly warmer and less dense than climatology but just as salty. A direct path from SSS_{max} water to STUW formation was not seen in the SPURS-1 region. STUW either forms slightly north of the SSS_{max} area, undergoes mixing during/after subduction, or the density range associated with STUW should be expanded to 25-26 kg/m^3 which represents waters of a broader temperature range with salinities >36.5 PSU.

Argo climatologies show similar net subduction rates when compared to previous studies but with enhanced lateral induction. Much larger increases to lateral induction rates were observed at the central mooring location in the SPURS-1 region. Increasing the resolved resolution to the mesoscale reveals lateral induction hundreds of m/yr larger than other studies. The net effect of

this increase and variability may be limited however, with each increase in subduction likely being accompanied by an increase in obduction. While subduction via lateral induction may be greatly enhanced on one side of an eddy, it could be greatly decreased on the other side, having a net neutral effect on subduction rates. While the signature of this appears to be present in MLD variability, high quality velocity data at a finer space and time resolutions is needed to confirm. Variability in MLD and subduction rates highlights the large interannual variability in the region (Qu et al., 2016). For subduction and water mass formation rates to be represented in models, improving the characterization of MLD variability-in both time and space-is required. Since the climatologies used in this study are from a limited time frame it is expected they are prone to representativeness errors of unknown size. Additional years of high quality satellite wind measurements and the continuation of the Argo program at its target density will be essential to determining the interannual variability and fully describing the MLD.

Acknowledgments:

A tremendous thank you to the numerous SPURS-1 scientists and the crews of the R/V Knorr and R/V Endeavor for the work that went into collecting SPURS-1 data and the lab group members who built and readied instruments for deployment. An extra thank you to J. Thomas Farrar, William Kessler, Craig Lee, Luc Rainville, and Charles Eriksen for providing the mooring and Seaglider data used in this study and Frank Bryan for suggestions regarding eddy subduction. Data used in this study were obtained from the following locations: AGVA (http://flux.ocean.washington.edu/agva/), MIMOC (http://www.pmel.noaa.gov/mimoc/), SCOW (http://cioss.coas.oregonstate.edu/scow/), SPURS assets; Argo, Seaglider, PICO, WHOI central mooring (https://podaac.jpl.nasa.gov/), ASCAT (http://www.remss.com/missions/ascat),

GEKCO (http://ctoh.legos.obs-mip.fr/products/global-surface-currents/global-surface-current-data-product). Support for this work was generously supported through NASA grants NNX09AU71G and NNX11AF79G to the University of Washington.

References:

Armi, L., & Stommel, H. (1983). Four Views of a Portion of the North Atlantic Subtropical Gyre. *Journal of Physical Oceanography*, *13*(5), 828–857. https://doi.org/10.1175/1520-0485(1983)013<0828:FVOAPO>2.0.CO;2

de Boyer Montégut, C., Madec, G., Fischer, A. S., Lazar, A., & Iudicone, D. (2004). Mixed layer depth over the global ocean: An examination of profile data and a profile-based climatology. *Journal of Geophysical Research: Oceans*, *109*(C12), C12003. https://doi.org/10.1029/2004JC002378

Busecke, J., Gordon, A. L., Li, Z., Bingham, F. M., & Font, J. (2014). Subtropical surface layer salinity budget and the role of mesoscale turbulence. *Journal of Geophysical Research: Oceans*, *119*(7), 4124–4140. https://doi.org/10.1002/2013JC009715

Busecke, J., Abernathey, R. P., & Gordon, A. L. (2017). Lateral eddy mixing in the subtropical salinity maxima of the global ocean. *Journal of Physical Oceanography*. https://doi.org/10.1175/JPO-D-16-0215.1

Cushman-Roisin, B. (1987). Subduction. *Hawaii Univ, Dynamics of the Oceanic Surface Mixed Layer p 181-196(SEE N 88-20785 13-48)*.

Da Costa, M. V., Mercier, H., & Treguier, A. M. (2005). Effects of the Mixed Layer Time Variability on Kinematic Subduction Rate Diagnostics. *Journal of Physical Oceanography*, *35*(4), 427–443. https://doi.org/10.1175/JPO2693.1

Durack, P. J., Wijffels, S. E., & Matear, R. J. (2012). Ocean Salinities Reveal Strong Global Water Cycle Intensification During 1950 to 2000. *Science*, *336*(6080), 455–458. https://doi.org/10.1126/science.1212222

Farrar, T., Rainville, L., Plueddemann, A. J., Kessler, W. S., Lee, C., Hodges, B. A., … Fratantoni, D. M. (2015). Salinity and Temperature Balances at the SPURS Central Mooring During Fall and Winter. *Oceanography*, *28*(1), 56–65. https://doi.org/10.5670/oceanog.2015.06

Figa-Saldaña, J., Wilson, J. J. w., Attema, E., Gelsthorpe, R., Drinkwater, M. R., & Stoffelen, A. (2002). The advanced scatterometer (ASCAT) on the meteorological operational (MetOp) platform: A follow on for European wind scatterometers. *Canadian Journal of Remote Sensing*, *28*(3), 404–412. https://doi.org/10.5589/m02-035

Foltz, G. R., & McPhaden, M. J. (2008). Seasonal mixed layer salinity balance of the tropical North Atlantic Ocean. *Journal of Geophysical Research: Oceans*, *113*(C2), C02013. https://doi.org/10.1029/2007JC004178

Gebbie, G. (2007). Does eddy subduction matter in the northeast Atlantic Ocean? *Journal of Geophysical Research: Oceans*, *112*(C6), C06007. https://doi.org/10.1029/2006JC003568

Gordon, A. L., & Giulivi, C. F. (2014). Ocean eddy freshwater flux convergence into the North Atlantic subtropics. *Journal of Geophysical Research: Oceans*, *119*(6), 3327–3335. https://doi.org/10.1002/2013JC009596

Gray, A. R., & Riser, S. C. (2014). A Global Analysis of Sverdrup Balance Using Absolute Geostrophic Velocities from Argo. *Journal of Physical Oceanography*, *44*(4), 1213–1229. https://doi.org/10.1175/JPO-D-12-0206.1

Held, I. M., & Soden, B. J. (2006). Robust responses of the hydrological cycle to global warming. *Journal of Climate*, *19*(21), 5686–5699.

Holte, J., & Talley, L. (2009). A New Algorithm for Finding Mixed Layer Depths with Applications to Argo Data and Subantarctic Mode Water Formation. *Journal of Atmospheric and Oceanic Technology*, *26*(9), 1920–1939. https://doi.org/10.1175/2009JTECHO543.1

Jenkins, W. J. (1987). 3H and 3He in the Beta Triangle: Observations of Gyre Ventilation and Oxygen Utilization Rates. *Journal of Physical Oceanography*, *17*(6), 763–783. https://doi.org/10.1175/1520-0485(1987)017<0763:AITBTO>2.0.CO;2

Jenkins, W. J. (1998). Studying subtropical thermocline ventilation and circulation using tritium and 3He. *Journal of Geophysical Research: Oceans*, *103*(C8), 15817–15831. https://doi.org/10.1029/98JC00141

Joyce, T. M., & Jenkins, W. J. (1993). Spatial variability of subducting water in the North Atlantic: A pilot study. *Journal of Geophysical Research: Oceans*, *98*(C6), 10111–10124. https://doi.org/10.1029/93JC00572

Katsura, S., Oka, E., Qiu, B., & Schneider, N. (2013). Formation and Subduction of North Pacific Tropical Water and Their Interannual Variability. *Journal of Physical Oceanography*, *43*(11), 2400–2415. https://doi.org/10.1175/JPO-D-13-031.1

Kolodziejczyk, N., Reverdin, G., & Lazar, A. (2014). Interannual Variability of the Mixed Layer Winter Convection and Spice Injection in the Eastern Subtropical North Atlantic. *Journal of Physical Oceanography*, *45*(2), 504–525. https://doi.org/10.1175/JPO-D-14-0042.1

Large, W. G., & Pond, S. (1981). Open Ocean Momentum Flux Measurements in Moderate to Strong Winds. *Journal of Physical Oceanography*, *11*(3), 324–336. https://doi.org/10.1175/1520-0485(1981)011<0324:OOMFMI>2.0.CO;2

Levitus, S., & Boyer, T. P. (1994). *World Ocean Atlas 1994. Volume 4. Temperature* (No. PB--95-270112/XAB; NESDIS--4). National Environmental Satellite, Data, and Information

Service, Washington, DC (United States). Retrieved from https://www-osti-gov.offcampus.lib.washington.edu/scitech/biblio/137203

Levitus, S., Burgett, R., & Boyer, T. P. (1994). *World Ocean Atlas 1994. Volume 3. Salinity*. National Environmental Satellite, Data, and Information Service, Washington, DC (United States). Retrieved from https://www-osti-gov.offcampus.lib.washington.edu/scitech/biblio/137202

Marshall, D. (1997). Subduction of water masses in an eddying ocean. *Journal of Marine Research*, *55*(2), 201–222. https://doi.org/10.1357/0022240973224373

Marshall, J. C., Williams, R. G., & Nurser, A. J. G. (1993). Inferring the Subduction Rate and Period over the North Atlantic. *Journal of Physical Oceanography*, *23*(7), 1315–1329. https://doi.org/10.1175/1520-0485(1993)023<1315:ITSRAP>2.0.CO;2

O'Connor, B. M., Fine, R. A., & Olson, D. B. (2005). A global comparison of subtropical underwater formation rates. *Deep Sea Research Part I: Oceanographic Research Papers*, *52*(9), 1569–1590. https://doi.org/10.1016/j.dsr.2005.01.011

O'Connor, B. M., Fine, R. A., Maillet, K. A., & Olson, D. B. (2002). Formation rates of subtropical underwater in the Pacific Ocean. *Deep Sea Research Part I: Oceanographic Research Papers*, *49*(9), 1571–1590. https://doi.org/10.1016/S0967-0637(02)00087-0

Osse, T. J., Meinig, C., Stalin, S., & Milburn, H. (2015). The PRAWLER, a vertical profiler powered by wave energy. In *OCEANS 2015 - MTS/IEEE Washington* (pp. 1–8). https://doi.org/10.23919/OCEANS.2015.7404354

Qiu, B., & Huang, R. X. (1995). Ventilation of the North Atlantic and North Pacific: Subduction Versus Obduction. *Journal of Physical Oceanography*, *25*(10), 2374–2390. https://doi.org/10.1175/1520-0485(1995)025<2374:VOTNAA>2.0.CO;2

Qu, T., Gao, S., & Fukumori, I. (2011). What governs the North Atlantic salinity maximum in a global GCM? *Geophysical Research Letters*, *38*(7), n/a–n/a. https://doi.org/10.1029/2011GL046757

Qu, T., Gao, S., & Fukumori, I. (2013). Formation of salinity maximum water and its contribution to the overturning circulation in the North Atlantic as revealed by a global general circulation model. *Journal of Geophysical Research: Oceans*, *118*(4), 1982–1994. https://doi.org/10.1002/jgrc.20152

Qu, T., Zhang, L., & Schneider, N. (2016). North Atlantic Subtropical Underwater and Its Year-to-Year Variability in Annual Subduction Rate during the Argo Period. *Journal of Physical Oceanography*, *46*(6), 1901–1916. https://doi.org/10.1175/JPO-D-15-0246.1

Ralph, E. A., & Niiler, P. P. (1999). Wind-Driven Currents in the Tropical Pacific. *Journal of Physical Oceanography*, *29*(9), 2121–2129. https://doi.org/10.1175/1520-0485(1999)029<2121:WDCITT>2.0.CO;2

Risien, C. M., & Chelton, D. B. (2008). A Global Climatology of Surface Wind and Wind Stress Fields from Eight Years of QuikSCAT Scatterometer Data. *Journal of Physical Oceanography*, *38*(11), 2379–2413. https://doi.org/10.1175/2008JPO3881.1

Sallée, J.-B., Speer, K., Rintoul, S., & Wijffels, S. (2010). Southern Ocean Thermocline Ventilation. *Journal of Physical Oceanography*, *40*(3), 509–529. https://doi.org/10.1175/2009JPO4291.1

Schanze, J. J., Schmitt, R. W., & Yu, L. L. (2010). The global oceanic freshwater cycle: A state-of-the-art quantification. *Journal of Marine Research*, *68*(3–1), 569–595. https://doi.org/10.1357/002224010794657164

Scharffenberg, M. G., & Stammer, D. (2010). Seasonal variations of the large-scale geostrophic flow field and eddy kinetic energy inferred from the TOPEX/Poseidon and Jason-1 tandem mission data. *Journal of Geophysical Research: Oceans*, *115*(C2), C02008. https://doi.org/10.1029/2008JC005242

Scheff, J., & Frierson, D. M. W. (2012). Robust future precipitation declines in CMIP5 largely reflect the poleward expansion of model subtropical dry zones. *Geophysical Research Letters*, *39*(18), L18704. https://doi.org/10.1029/2012GL052910

Schlax, M. G., Chelton, D. B., & Freilich, M. H. (2001). Sampling Errors in Wind Fields Constructed from Single and Tandem Scatterometer Datasets. *Journal of Atmospheric and Oceanic Technology*, *18*(6), 1014–1036. https://doi.org/10.1175/1520-0426(2001)018<1014:SEIWFC>2.0.CO;2

Schmidtko, S., Johnson, G. C., & Lyman, J. M. (2013). MIMOC: A global monthly isopycnal upper-ocean climatology with mixed layers. *Journal of Geophysical Research: Oceans*, *118*(4), 1658–1672. https://doi.org/10.1002/jgrc.20122

Schmitt, R. W. (2008). Salinity and the Global Water Cycle. *Oceanography*, *21*(1), 12.

Schmitt, R. W., Bogden, P. S., & Dorman, C. E. (1989). Evaporation Minus Precipitation and Density Fluxes for the North Atlantic. *Journal of Physical Oceanography*, *19*(9), 1208–1221. https://doi.org/10.1175/1520-0485(1989)019<1208:EMPADF>2.0.CO;2

Seager, R., Naik, N., & Vecchi, G. A. (2010). Thermodynamic and Dynamic Mechanisms for Large-Scale Changes in the Hydrological Cycle in Response to Global Warming. *Journal of Climate*, *23*(17), 4651–4668. https://doi.org/10.1175/2010JCLI3655.1

Skliris, N., Zika, J. D., Nurser, G., Josey, S. A., & Marsh, R. (2016). Global water cycle amplifying at less than the Clausius-Clapeyron rate. *Scientific Reports*, *6*, srep38752. https://doi.org/10.1038/srep38752

Spall, M. A., Weller, R. A., & Furey, P. W. (2000). Modeling the three-dimensional upper ocean heat budget and subduction rate during the Subduction Experiment. *Journal of Geophysical Research: Oceans*, *105*(C11), 26151–26166. https://doi.org/10.1029/2000JC000228

Stommel, H. (1979). Determination of water mass properties of water pumped down from the Ekman layer to the geostrophic flow below. *Proceedings of the National Academy of Sciences*, *76*(7), 3051–3055.

Sudre, J., Maes, C., & Garçon, V. (2013). On the global estimates of geostrophic and Ekman surface currents. *Limnology and Oceanography: Fluids and Environments*, *3*(1), 1–20. https://doi.org/10.1215/21573689-2071927

Trossman, D. S., Thompson, L. A., Kelly, K. A., & Kwon, Y.-O. (2009). Estimates of North Atlantic Ventilation and Mode Water Formation for Winters 2002–06. *Journal of Physical Oceanography*, *39*(10), 2600–2617. https://doi.org/10.1175/2009JPO3930.1

Wenegrat, J. O., McPhaden, M. J., & Lien, R.-C. (2014). Wind stress and near-surface shear in the equatorial Atlantic Ocean. *Geophysical Research Letters*, *41*(4), 2013GL059149. https://doi.org/10.1002/2013GL059149

Yang, J., Riser, S. C., Nystuen, J. A., Asher, W. E., & Jessup, A. T. (2015). Regional Rainfall Measurements: Using the Passive Aquatic Listener During the SPURS Field Campaign. *Oceanography*, *28*(1), 124–133. https://doi.org/10.2307/24861850

Yu, L. (2011). A global relationship between the ocean water cycle and near-surface salinity. *Journal of Geophysical Research: Oceans*, *116*(C10), n/a–n/a. https://doi.org/10.1029/2010JC006937

Table 4.1. Subduction rates in the SPURS-1 area

Table 4.1. Subduction rates in the SPURS-1 area

	Ekman Pumping (m/yr)	Sverdrup (m/yr)	Vertical Pumping (m/yr)	Lateral Induction (m/yr)	Annual Subduction (m/yr)
Marshall et al. [1993]	50		50	0-50	50-100
O'Connor et al. [2005] Drifters	49	-12	37	-1	36
O'Connor et al. [2005] Tracers	-	-	-	-	44
Updated Climatology	33 ± 6	-11 ± 4	22 ± 7	19 ± 8	41 ± 6
SPURS-1 Central Mooring	6 ± 1	-30 ± 7	-24 ± 7	-934 ± 471	-958 ± 477

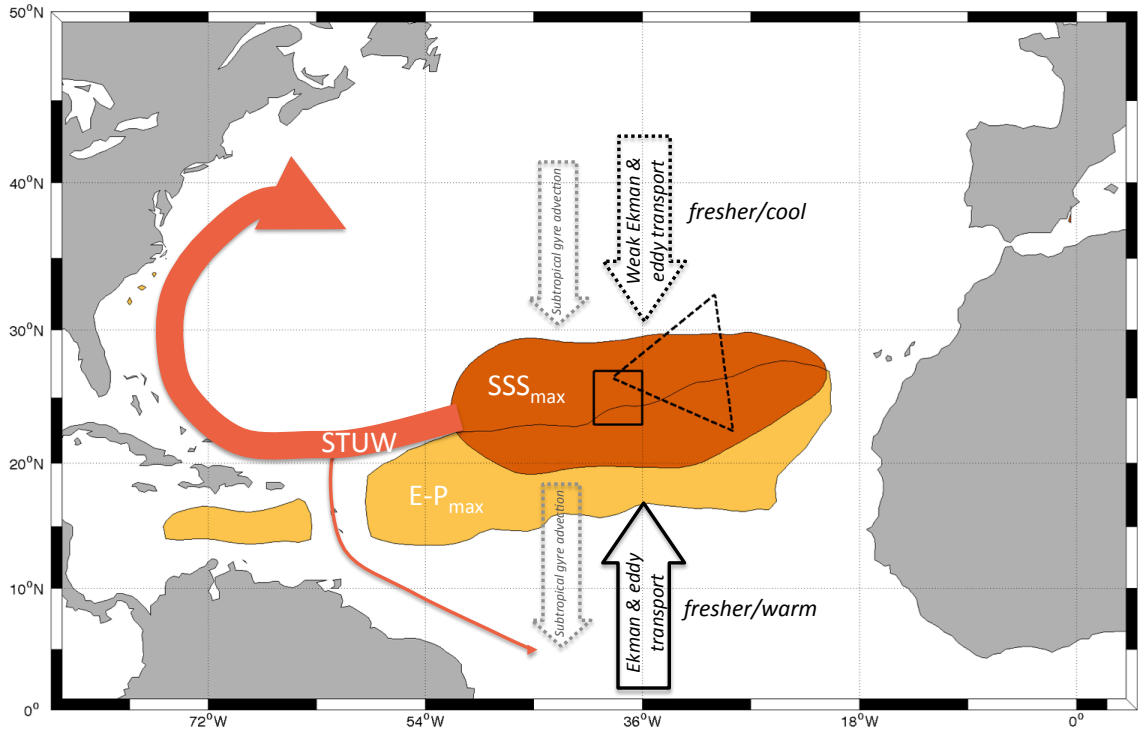

Figure 4.1. Location and path of SSS_{max} and STUW. The mean SSS_{max} location (orange) is north of the E-P maximum (tan). Ekman and eddy convergence bring fresh water in the SSS_{max} region. After subduction, SSS_{max} water flows southwest until recirculating the basin or exiting to the tropics. Based on the schematic of (Gordon & Giulivi, 2014). SPURS study area (black box) and beta triangle study area (grey triangle) is also shown. Salinity data (Salinity > 37.1 PSU) from MIMOC (Schmidtko et al., 2013). E-P (E-P > 1.2 m/yr) data from (Schanze et al., 2010)

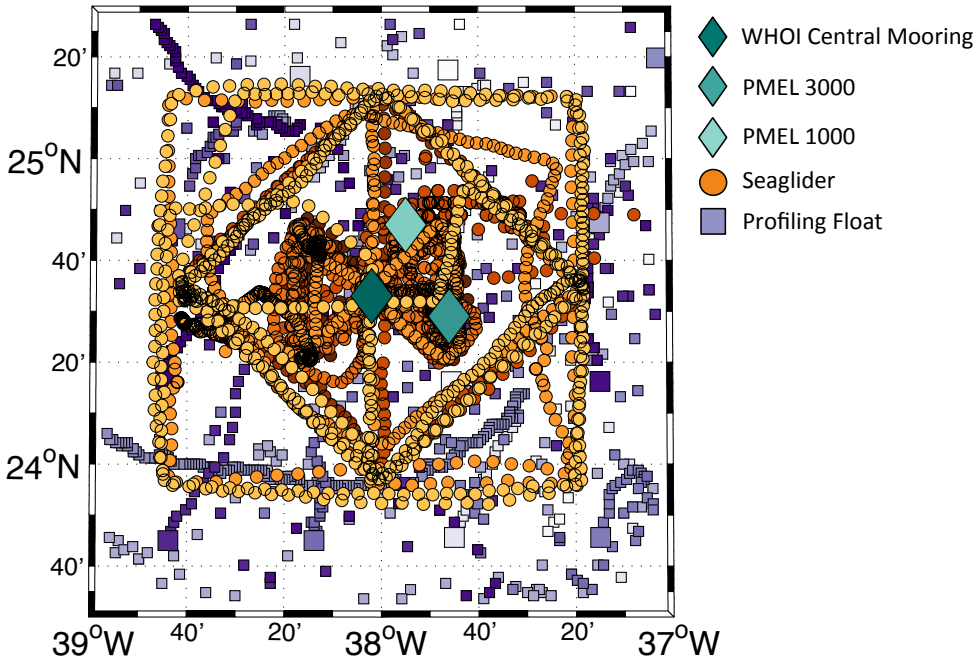

Figure 4.2. Study area and location of profiles collected by SPURS assets. Teal diamonds indicate mooring locations, Seaglider profiles with orange circles, and Argo float profiles with purple squares (deployment locations are slightly larger). All profiles collected by a single Seaglider or Argo float are the same shade of orange or purple, respectively. Seagliders operated in a three tiered, nested, spatial mission consisting of an outer box, middle diamond, and interior bowtie.

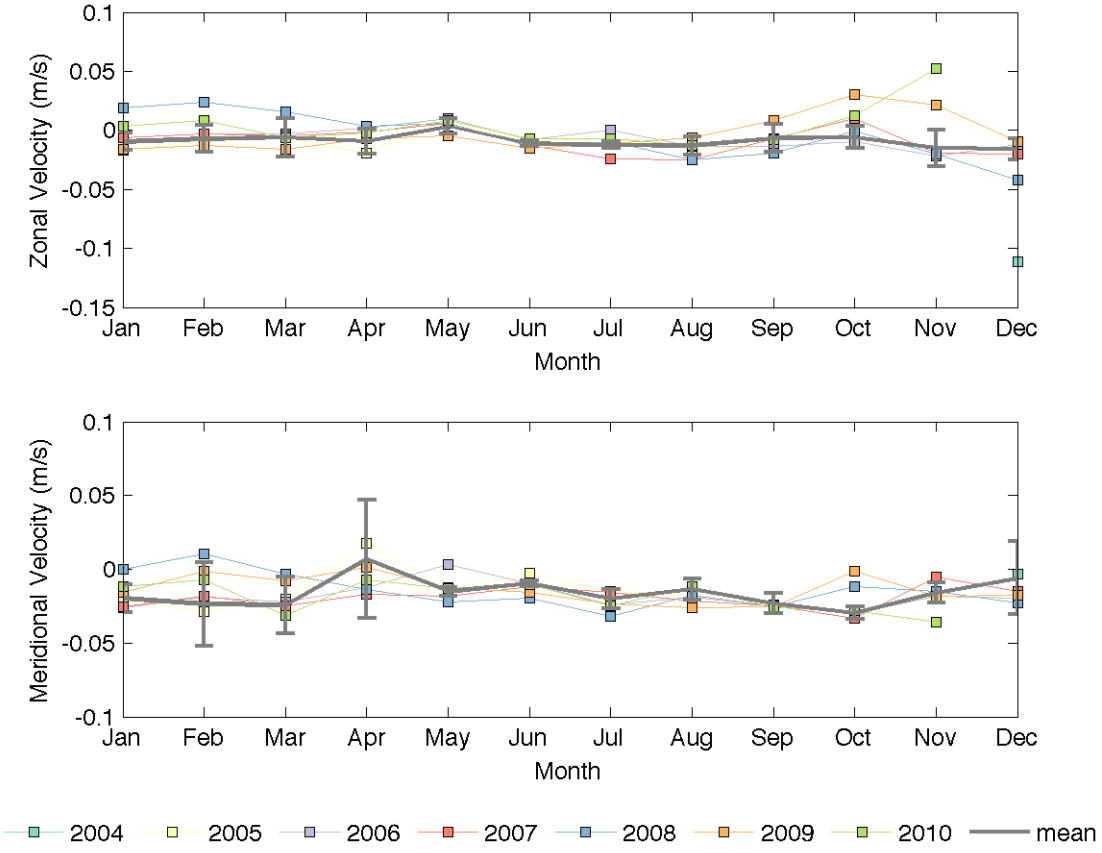

Figure 4.3. AGVA mean (2004-2010) (gray) zonal and meridional components of velocity in the SPURS-1 area and individual year values (various colors).

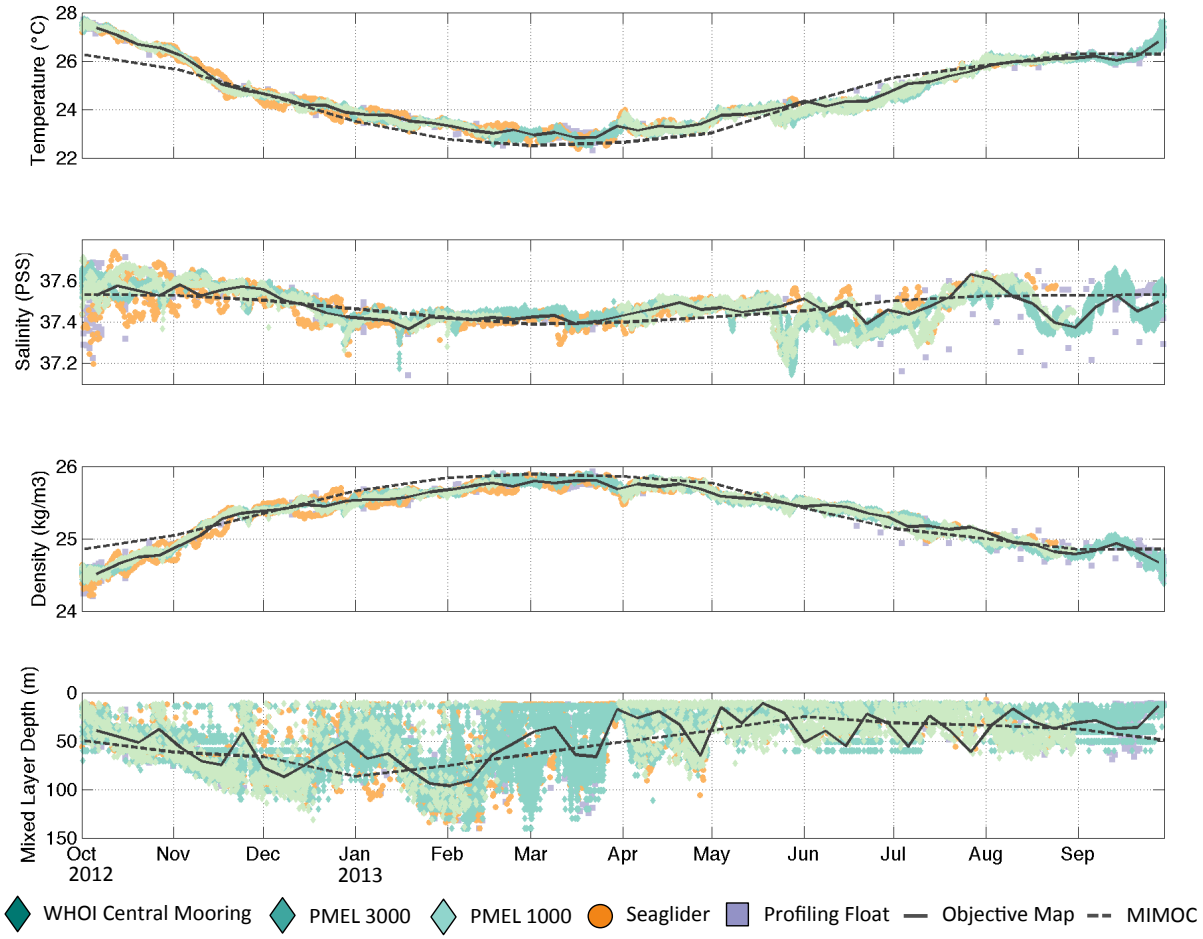

Figure 4.4. Average temperature (a), salinity (b), and density (c) of the mixed layer in the SPURS-1 area. Depth of the mixed layer is shown in (d). Observational values from moorings, Seagliders, and Argo floats are indicated with colored dots. Mean values from the objective map in the SPURS-1 area (solid line) and MIMOC (dashed line) are also plotted.

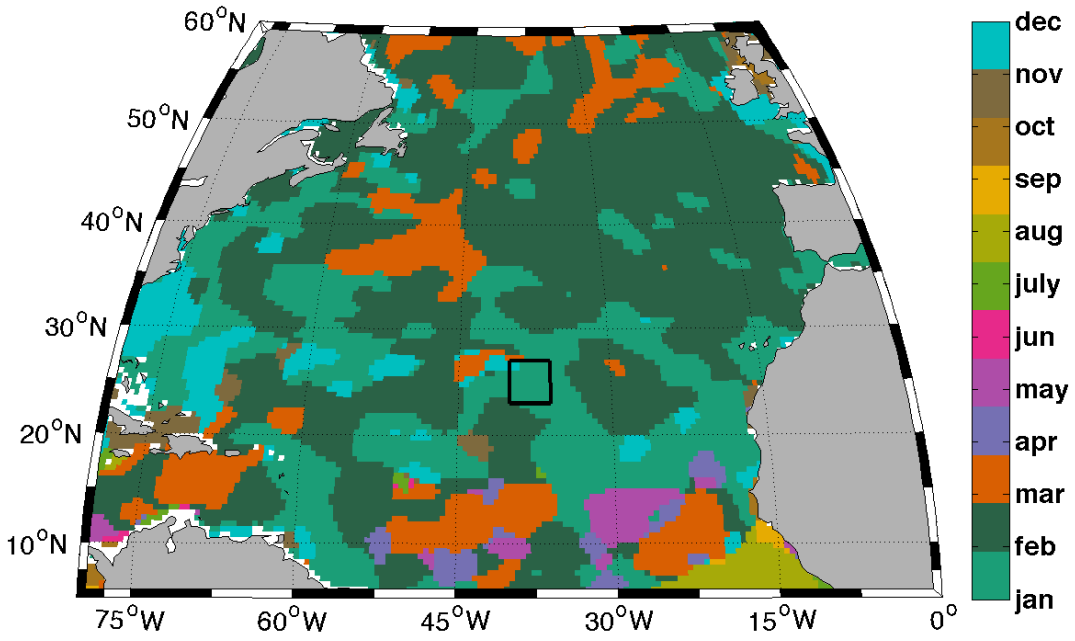

Figure 4.5. Month of maximum MLD from MIMOC data. Location of SPURS-1 area indicated with black box.

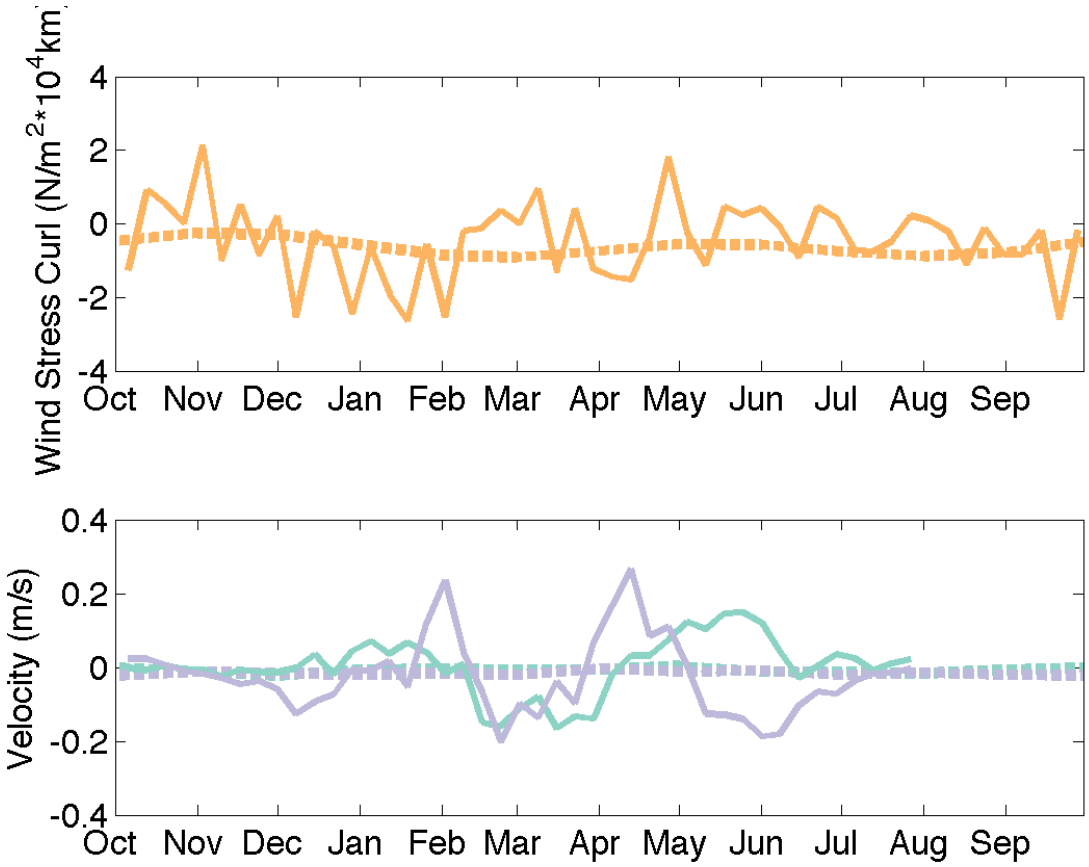

Figure 4.6. (a) Wind stress curl averaged over the SPURS-1 area from SCOW climatology (dashed) and ASCAT during the study period (solid), (b) meridional (purple) and zonal (teal) geostrophic velocity at the depth of the winter mixed layer from AGVA (dashed) and velocity from the central mooring ADCP (solid).

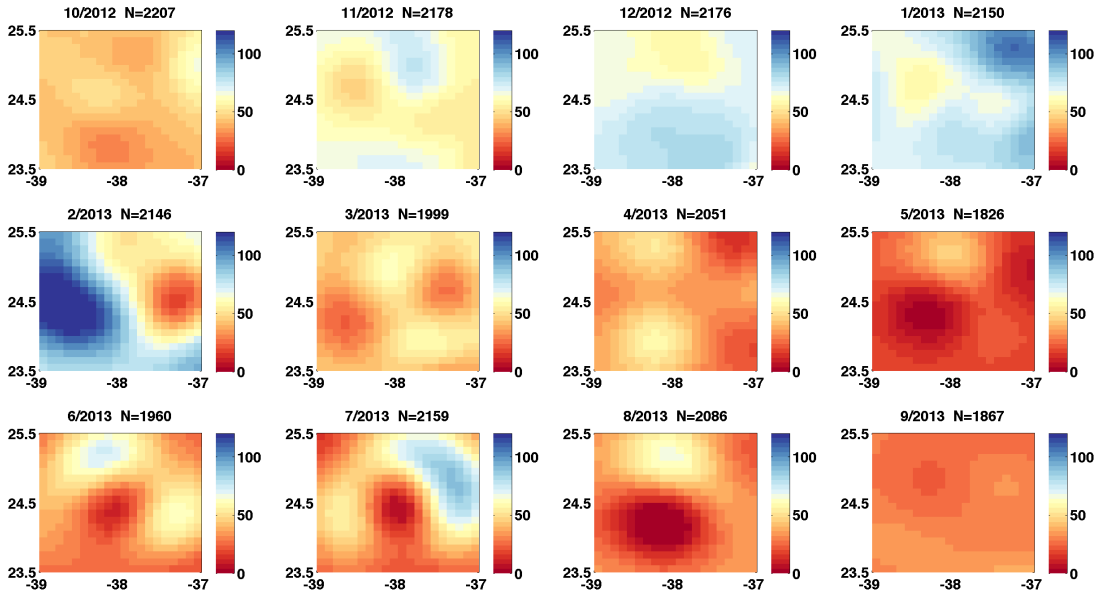

Figure 4.7. Mixed layer depth (m) in the SPURS-1 area from monthly averaged objective maps.

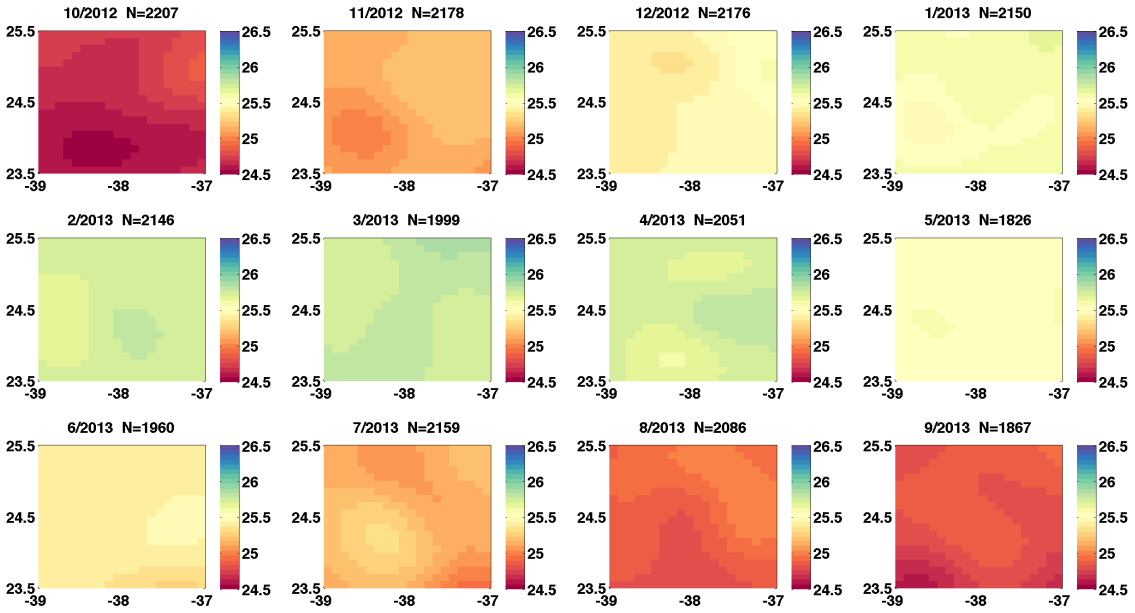

Figure 4.8. Mixed layer average density (kg/m^3) in the SPURS-1 area from monthly averaged objective maps.

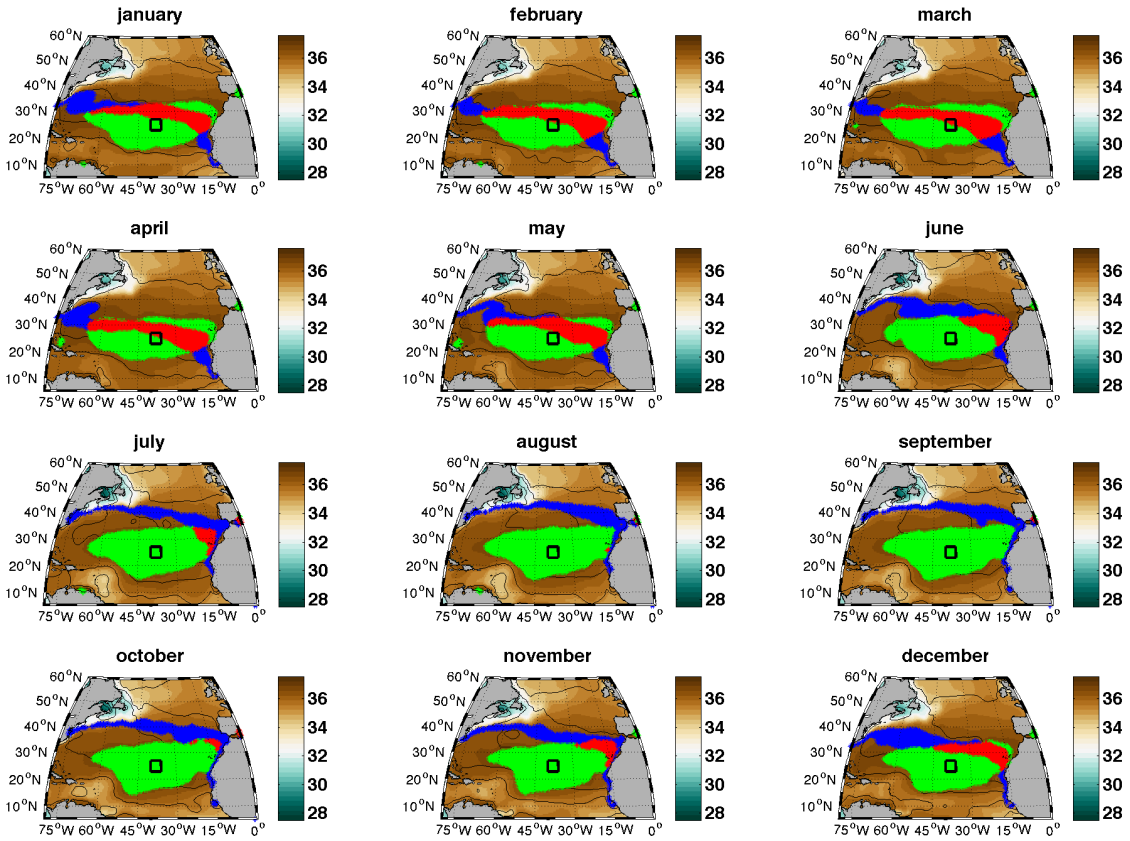

Figure 4.9. Monthly geographic extent of Subtropical Underwater (STUW) determined from MIMOC mixed layer data. Areas where the mixed layer properties are within ranges associated with STUW are shown for temperature only (blue), salinity only (green), and for both temperature and salinity (red). Mixed layer salinity is indicated with the colormap. SPURS study region is indicated with black box.

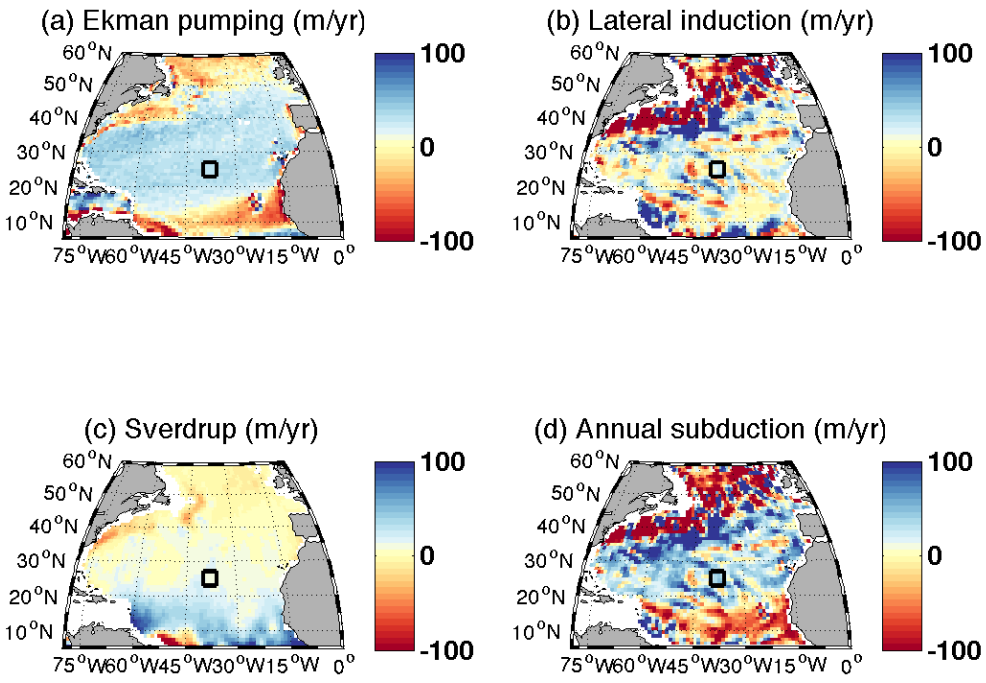

Figure 4.10. Contributions from (a) Ekman pumping, (b) lateral induction, and (c) Sverdrup flow to the (d) climatological annual subduction rate (m/yr). Positive values indicate subduction.

Appendix A

Conductivity Cell Thermal Mass Correction (CTM) for Seabird Surface Temperature and Salinity (STS) sensors

Conductivity, Temperature, Depth (CTD) is the general name given to a range of instruments that contain both a thermistor and a conductivity cell. Within the CTD unit, these two elements are physically separated wherein one element is located downstream of the other. Due to this physical separation as well as differences in the response time of each element, there is a temporal mismatch between when a water parcel is measured by each element. Additionally, the materials used for the conductivity cell influence the response time via thermal inertia. Several adjustments are commonly applied to raw CTD data to correct for these spatial and temporal mismatches including: thermistor response (identified as a blurring of sharp gradients), thermistor and conductivity cell physical separation (identified as salinity spikes), and conductivity cell thermal mass (CTM) (identified as artificial salting/freshening) (Johnson et al., 2007). Here we consider the last of these corrections, conductivity cell thermal mass (CTM), for the Surface Temperature and Salinity (SBE-STS) CTD manufactured by Seabird Electronics, Inc. (Seabird).

CTM errors, or the transfer of heat stored in the cell, manifest due to the physical properties of the conductivity cell as well as the flow rate through the cell. By assuming quasi-steady heat transfer, Lueck (1990) developed equations that describe the heat transfer effects on

conductivity. This result was then simplified into the following temperature adjustment (Morison et al., 1994):

$$T_T(n) = -bT_T(n-1) + a[T(n) - T(n-1)] \quad \text{(A.1)}$$

which can then be used to calculate conductivity. T_T Is the temperature correction and a and b are defined by:

$$a = 4f_n\alpha\beta^{-1}(1 + 4f_n\beta^{-1})^{-1} \quad \text{(A.2)}$$

$$b = 1 - 2a\alpha^{-1} \quad \text{(A.3)}$$

where f_n is the Nyquist frequency, α is the initial magnitude of the temperature change, and τ_{CTM}, the relaxation time, is equal to β^{-1}. Values of α and τ_{CTM} are dependent on the flushing rate of the cell where both α and τ_{CTM} grow exponentially as the velocity slows (Morison et al., 1994). Correction values for the unpumped STS unit which ascends at ~9 cm/s are thus likely to be larger than correction values determined for CTDs which are pumped with velocities an order of magnitude larger. Additionally, variable ascent rates on Argo floats require that values of α and τ_{CTM} are determined for each ascent rate instead of a singular pair for a constant pumping rate. CTM errors can be identified as artificial salting or freshening signals when moving from warm to cold or cold to warm water, respectively. Shown in Figure A.1 is a time series of SBE-STS temperature and salinity data collected by float 7742 in the subtropical Atlantic. The CTM error is identified as a fresh signal that is concurrent in depth and time with a large diurnal warming signal. A lack of rainfall in this region was confirmed with satellite precipitation data.

Since a CTM correction is not commonly determined in the laboratory for each CTD, we utilize the statistical approach applied to the pumped, SBE-41 CTD aboard Argo floats by Johnson et al. (2007) to determine values of α and τ_{CTM} for the SBE-STS CTD. In this approach, profiles with strong gradients underneath a well mixed layer (ML) are identified and a range of α (0-20) and

τ_{CTM} (0-75 (s)) pairs are used to calculated an adjustment to the temperature profile (Equation 1) and a new density profile. The combination of α and τ_{CTM} that minimizes the density gradient across the ML base are then determined for each profile. By repeating this process for many profiles, a singular value of α and τ_{CTM} can be determined statistically for a given flushing rate of the sensor. Applied to the SBE-STS unit, α and τ_{CTM} values which minimize the difference between the mean uncorrected ML density and the corrected bottom two ML samples were chosen. The flushing rate of the STS unit was determined as the average ascent rate of the float between ~3-25 m for each profile. Shown in Figure A.2 is the range of α and τ_{CTM} determined using this method for float 7742. A clear relationship between ascent rate and α/ τ_{CTM} is not found. This may be due to the highly variable ascent rate of the float (3-14 cm/s). Additionally, the theoretical curve of Morison et al. (1994) shows that a large range of α and τ_{CTM} values can be expected at slow flushing rates. Because of this, it may be more difficult to converge on α and τ_{CTM} due to the low ascent speeds of the SBE-STS equipped Argo floats.

The nonconvergence of α and τ_{CTM} values for float 7742 was also observed for other SBE-STS equipped Argo floats (not shown). Preliminary work completed by Seabird during STS development (Carol Janzen, person communication) estimated values of $\alpha = 0.21$ and $\tau_{CTM} = 6$ s by identifying values within the saddle of minimum squared residuals. Since multiple α/ τ_{CTM} pairs fall in the saddle, final values are determined manually by comparing profiles corrected with each pair. Similarly, a manual adjustment was attempted for several highly affected SBE-STS profiles from deployed floats. The application of Seabird estimated corrections and several other, minor to extreme values of α and τ_{CTM} did not successfully remove the observed artificial freshening signal (when moving from cool to warm) (Figure A.3). It was concluded that a consistent CTM correction (α/ τ_{CTM} pairs for each flushing rate) could not be determined for the

SBE-STS sensor using in situ data. This is likely due to either the variable ascent rate of the floats (flushing rate of the CTD) or another unknown physical process. The results from recent tank tests of the SBE-STS CTD by Seabird will be essential to determining the α and τ_{CTM} for idealized conditions as well as additional sensor corrections (Kim Martini, personal communication). The test tank experiments are limited in their range of tested ascent rates (flushing speeds) however, so application to in situ data may be difficult due to the highly variable, slow ascent rates of floats and other unknown confounding processes in the upper ocean. The CTM error is assumed to be small for the majority of profiles. If large diurnal warm layers are present, however, CTM errors may be significant.

References:

Johnson, G. C., Toole, J. M., & Larson, N. G. (2007). Sensor Corrections for Sea-Bird SBE-41CP and SBE-41 CTDs. *Journal of Atmospheric & Oceanic Technology*, *24*(6), 1117–1130. https://doi.org/10.1175/JTECH2016.1

Lueck, R. G. (1990). Thermal Inertia of Conductivity Cells: Theory. *Journal of Atmospheric and Oceanic Technology*, *7*(5), 741–755. https://doi.org/10.1175/1520-0426(1990)007<0741:TIOCCT>2.0.CO;2

Morison, J., Andersen, R., Larson, N., D'Asaro, E., & Boyd, T. (1994). The Correction for Thermal-Lag Effects in Sea-Bird CTD Data. *Journal of Atmospheric and Oceanic Technology*, *11*(4), 1151–1164. https://doi.org/10.1175/1520-0426(1994)011<1151:TCFTLE>2.0.CO;2

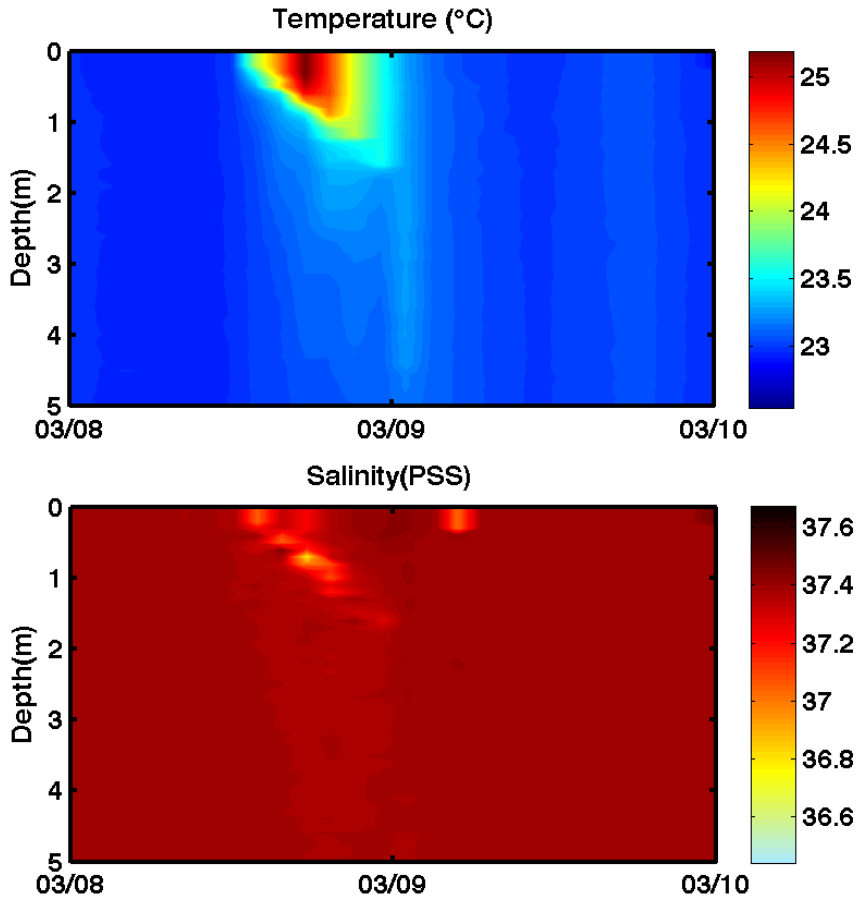

Figure A.1 Temperature and salinity for float 7742 (27.9°N, 40.7°W) deployed in the subtropical Atlantic.

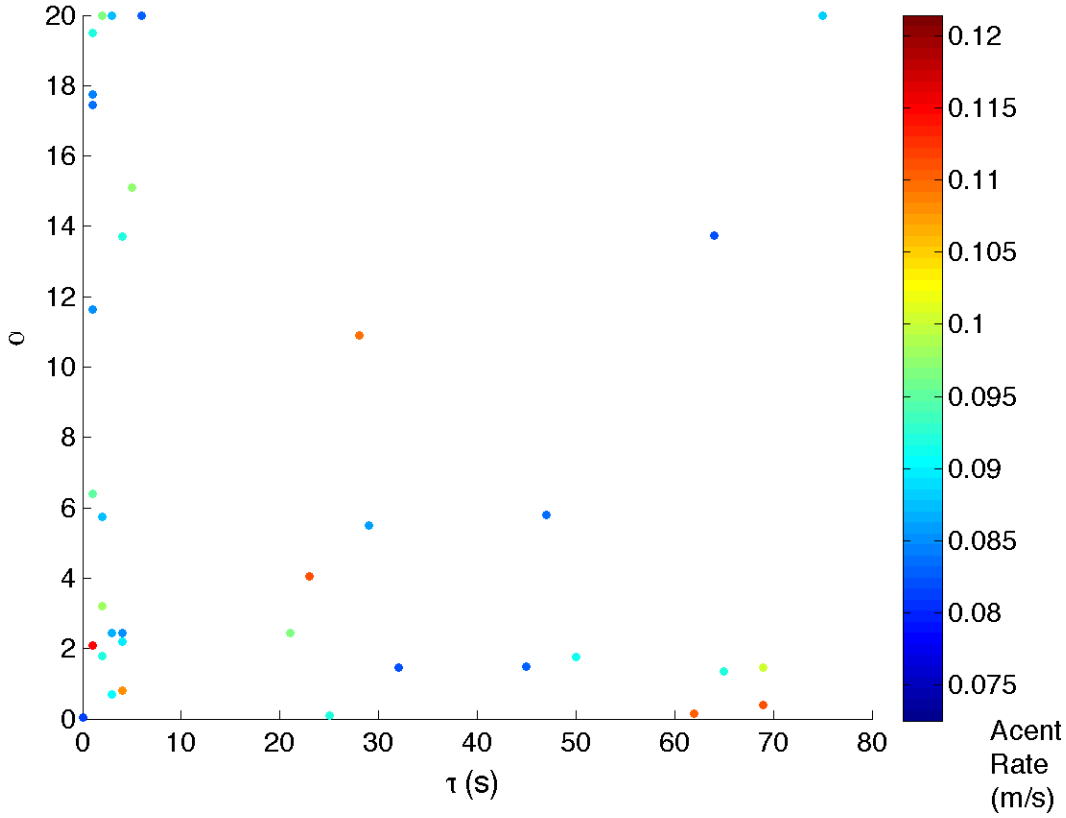

Figure A.2 α and τ_{CTM} values determined by minimizing the gradient at the base of the mixed layer. Color indicates the average ascent rate of float 7742 (27.9°N, 40.7°W) during the profile.

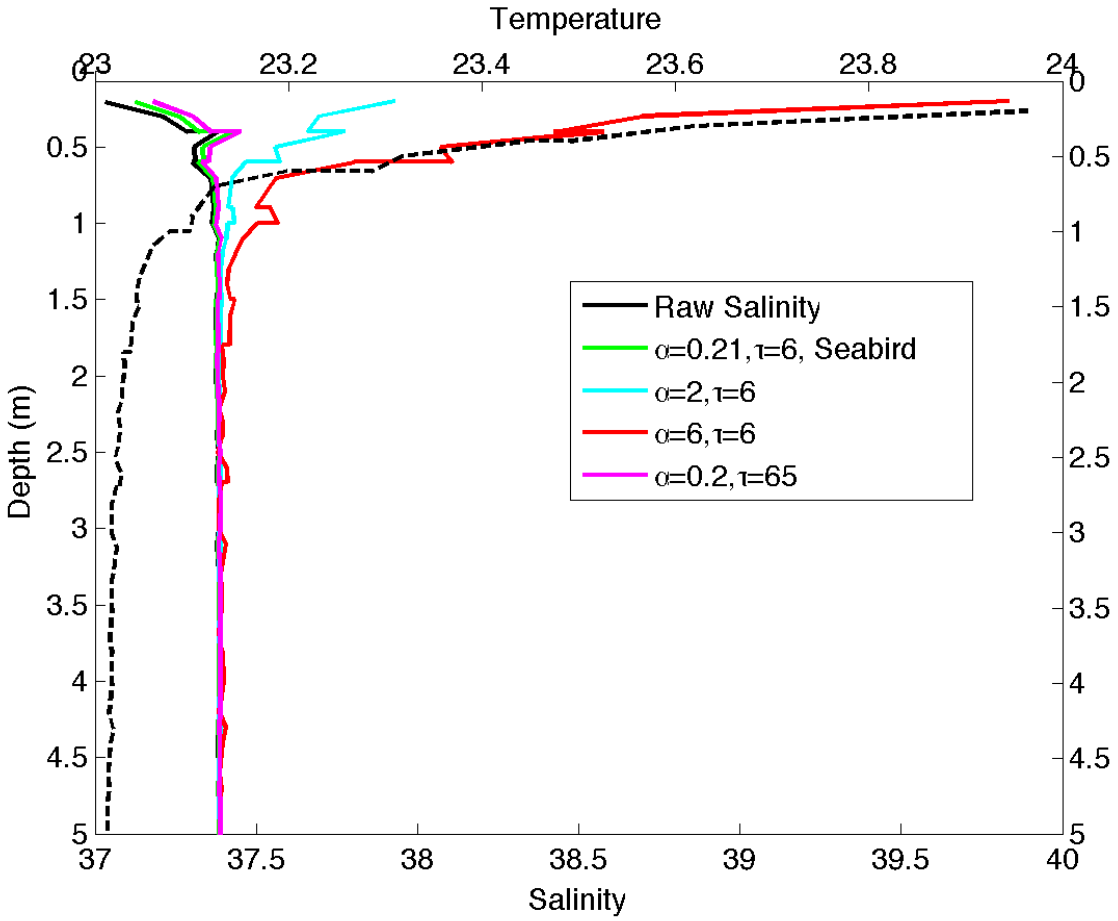

Figure A.3 Example adjustment of temperature and conductivity for float 7742 (27.9°N, 40.7°W) on 8 March, 2013.

VITA

Jesse Anderson was raised in Lawrence, Kansas. She graduated from The University of Kansas in 2004 with a Bachelor of Science in Atmospheric Science. She earned a Master of Science in Physical Oceanography from the University of Washington in 2012 and a Doctor of Philosophy in 2017.